Title
Plasma ion sources and ion beam technology in microfabrications

Author
Ji, Lili

Publication Date
2007-09-01

Plasma ion sources and ion beam technology in microfabrications

by

Lili Ji

B.S. (Peking University, P.R. China) 2002

A dissertation submitted in partial satisfaction of the

Requirements for the degree of

Doctor of Philosophy

in

Engineering-Nuclear Engineering

in the

GRADUATE DIVISION

of the

UNIVERSITY of CALIFORNIA, BERKELEY

Committee in charge:

Professor Ka-Ngo Leung, Chair
Professor Jasmina L. Vujic
Professor Vivek Subramanian
Doctor Qing Ji

Fall 2007

The dissertation of Lili Ji is approved:

Chair Date

Date

Date

Date

University of California, Berkeley

Fall 2007

Abstract

Plasma ion sources and ion beam technology in microfabrications

by

Lili Ji

Doctor of Philosophy in Nuclear Engineering

University of California, Berkeley

Professor Ka-Ngo Leung, Chair

For over decades, focused ion beam (FIB) has been playing a very important role in microscale technology and research, among which, semiconductor microfabrication is one of its biggest application area. As the dimensions of IC devices are scaled down, it has shown the need for new ion beam tools and new approaches to the fabrication of small-scale devices. In the meanwhile, nanotechnology has also deeply involved in material science research and bioresearch in recent years. The conventional FIB systems which utilize liquid gallium ion sources to achieve nanometer scale resolution can no longer meet the various requirements raised from such a wide application area such as low contamination, high throughput and so on. The drive towards controlling materials properties at nanometer length scales relies on the availability of efficient tools. In this thesis, three novel ion beam tools have been developed and investigated as the alternatives for the conventional FIB systems in some particular applications.

An integrated focused ion beam (FIB) and scanning electron microscope (SEM) system has been developed for direct doping or surface modification. This new instrument employs a mini-RF driven plasma source to generate focused ion beam with various ion species, a FEI two-lens electron (2LE) column for SEM imaging, and a five-

axis manipulator system for sample positioning. An all-electrostatic two-lens column has been designed to focus the ion beam extracted from the source. Based on the Munro ion optics simulation, beam spot sizes as small as 100 nm can be achieved at beam energies between 5 to 35 keV if a 5 μm-diameter extraction aperture is used. Smaller beam spot sizes can be obtained with smaller apertures at sacrifice of some beam current. The FEI 2LE column, which utilizes Schottky emission, electrostatic focusing optics, and stacked-disk column construction, can provide high-resolution (as small as 20 nm) imaging capability, with fairly long working distance (25 mm) at 25 keV beam voltage. Such an integrated FIB/SEM dual-beam system will not only improve the accuracy and reproducibility when performing ion beam sculpting and direct implantation processes, but will also enable researchers to perform cross-sectioning, imaging, and analysis with the same tool. A major advantage of this approach is the ability to produce a wide variety of ion species tailored to the application.

An ion beam tool with a new configuration has also been developed. By utilizing a double-chamber plasma ion source, a beam containing both positive ions and electrons can be generated. One of the advantages of this new configuration is that electrons in the beam can introduce surface neutralization effect without the need for beam alignment. Besides, electrons also introduce post-ionization effect. Experiment results have demonstrated that this can be used to improve performance of secondary ion mass spectrometry instruments. The secondary ion yield for an Al target has been enhanced to about one order of magnitude higher with the post-ionization induced by the low energy electrons in the combined beam. It can be further improved with the increase of electron beam current. When the combined beam is applied to insulating targets, sample charging is also eliminated. For Teflon targets, the secondary ion signal is increased by more than a factor of 20. In the meanwhile, simulation has been carried out for the system design. A simulation code "IBSimu" based on particle in cell algorithm has been developed by a collaborator Taneli Kalvas. It can simulate positive ions and electrons simultaneously. A combined-beam optical column has been designed using this code. Beam deflection and pulse generation of the combined beam have also been simulated.

The mini-rf plasma ion source used in the dual-beam and combined-beam systems is only suitable for generating ions of gaseous species. An rf plasma system for metallic ions generation and metal thin film deposition has also been developed. The system employs a radio-frequency (RF)-discharge plasma source with four straight RF antennas, which is made of or covered with the metal material, thus serving simultaneously as a sputtering target. With beam extraction and ion mass filter, metallic ions can be generated and can be used for direct patterning. Without beam extraction, the system can be used for thin film coating. The average deposition rate of the copper thin film can be as high as 500 nm/min when operated under continuous-wave (CW) mode. Film properties under different operating conditions (gas pressure, RF power, substrate biasing condition) have been investigated experimentally. Three thin-film coating schemes have been developed, one of which has been demonstrated to be suitable for conformal deep-trench coating. Conformal coating over trenches of high-aspect-ratio (>6:1) has been demonstrated at both micron and submicron scales.

Professor Ka-Ngo Leung

Nuclear Engineering Department

University of California, Berkeley

Table of Contents

5 Ion source for metallic ion beam generation and thin film deposition……..…..108

List of figures

ACKNOWLEDGEMENTS

Far too many people to mention individually have assisted in so many ways during my study at UC Berkeley and Lawrence Berkeley National Laboratory. They all have my sincere gratitude. In particular, I want to thank my family for their love and the constant support to my life and my study.

To Professor Ka-Ngo Leung, thanks for giving me the opportunity to work in this group and lead me into the world of plasma, thank you for all the guidance, teachings and encouragement, also thanks for giving me so many good suggestions for my future career. The five years of study under your instructions will benefit me in my future.

To Professor Vujic Jasmina and Professor Vivek Subramanian, thanks for accepting to read my dissertation and teaching me the knowledge on numerical simulation and IC devices. Thanks Professor Vujic for being the chair of my qualify exam committee.

To Dr. Qing Ji, I owe so many thanks to you. For me, you are a strict mentor, a considerate elder sister and a very close friend. Thanks for all the careness, encouragement, advice and help you’ve been giving to me through all these years.

To Ximan Jiang, thanks for being such a good friend and thank you for all your suggestions and help in my research work. Every time I discuss with you, I can learn something new.

I would like to thank all the members from the Ion Beam Technology group at Lawrence Berkeley National Laboratory. Thanks Steve Wilde, Tom McVeigh, Paul Wong, Frederic Gicquel and Jerry Fischer for the help on mechanical or electrical design

and machining, without your wonderful work, my research could not have gone this smoothly. Thanks Taneli Kalvas for developing the simulation code to assist my research work. Thanks Hannes Vainionpaa for helping with the simulation. Thanks to Ye Chen, Joon-Kuk Kim, Tak Pui Lou, Michael King, Ying Wu, Bret van den Akker and Helen Zhang for the friendship and the help on the experiments.

To Rick Gough, and the administrative coordinators, Darlene Hawkins, Martha Condon and Parish Epps, thanks for all your support during my work at Lawrence Berkeley Lab.

I would like to thank Lisa Zemelman for the instructions and the help to the studying in the Nuclear Engineering Department. Thanks for always being so nice.

I would like to acknowledge the Microfabrication Laboratory at UC Berkeley and the National Center for Electron Microscopy (NCEM) at the Lawrence Berkeley National Laboratory for providing the facilities for microfabrication and imaging.

I also would like to acknowledge the support from the Defense Advanced Research Projects Agency (DARPA) and the US Department of Energy through the Lawrence Berkeley National Laboratory under Contract No. DE-AC02-05CH11231.

Last but not least, I want to give my special thanks to Jianzhong and Shaonan. With your love, I can be strong enough to face all the difficulties. I wish I can be your strength to support you when you are weak.

There are many other people I’d like to thank to. Although not mentioning here, I owe you my sincere gratitude in my deep heart.

Chapter 1:

Introduction

1.1 Background

The focused ion beam (FIB) technique was mainly developed during the late 1970s and the early 1980s, and the first commercial instrument was introduced more than a decade ago.[1] Modern FIB systems are becoming widely available in semiconductor research and processing environments, as well as in material inspection, analysis and surface modification. The technology enables localized milling and deposition of conductors and insulators with high precision, hence its success in device modification, mask repair, process control and failure analysis.[2-6] In addition, the preparation of specimens for transmission electron microscopy (TEM) and the trimming of thin-film magnetoresistive heads (for magnetic storage disks) are important applications of FIB. Recently, a number of authors have reported the use of focused ion beam in micromachining applications for MEMS.[7-8] With the development and improvement of cross-discipline research, focused ion beam technology has extended its application into the area of biology[9-12] and medical research[13]. New applications and the continuous growth and improvement of conventional research keep raising more and more requirements on the FIB tools. In this chapter, the conventional FIB system and technology will be reviewed; its advantages and disadvantages will be discussed. New designs on focused ion beam systems will be proposed and presented in detail in the following chapters.

1.2 Conventional focused ion beam system (FIB)

As shown in figure 1.1, a conventional FIB system consists of an ion column, a working chamber, a vacuum system, a gas system and a workstation that provides the user interface. A schematic diagram of a FIB ion column is shown in figure 1.2. The structure of the column is similar to that of a scanning electron microscope, except that a FIB system employs a gallium ion (Ga^+) beam instead of an electron beam. The pressure inside the column is maintained at typically 1 x 10^{-7} mbar.

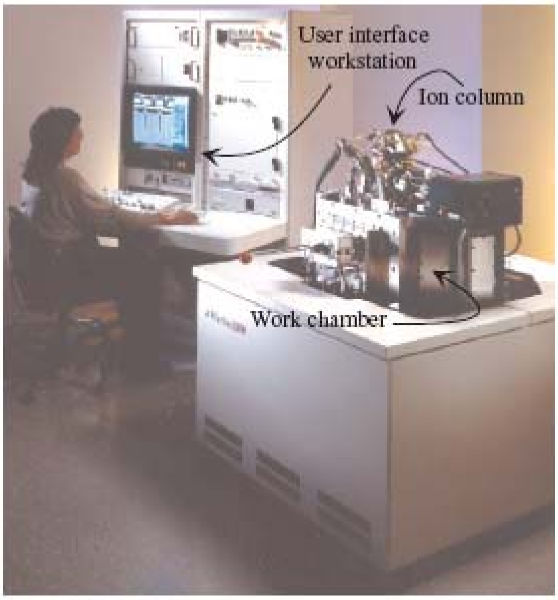

Figure 1.1: A typical FIB system (Micrion 2500). The most important components are indicated in the photograph[14].

1.2.1 Ion column

The ion beam is generated from a Liquid Metal Ion Source (LMIS) by the application of a strong electric field. This electric field causes the emission of positively charged ions from a liquid gallium cone, which is formed on the tip of a tungsten needle. A typical extraction voltage is 7000V. The extraction current under normal operating condition is ~ 2μA.

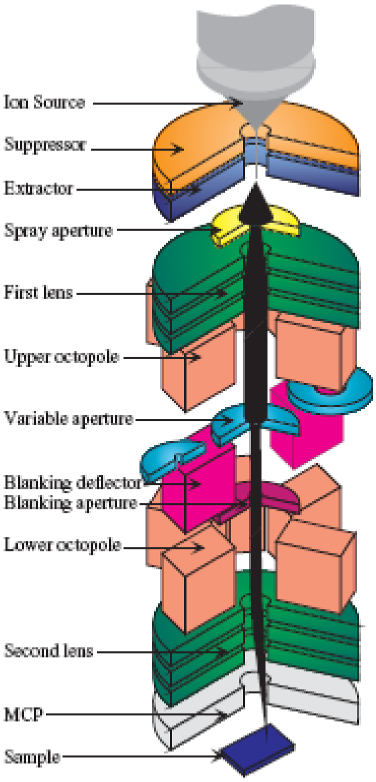

Figure 1.2: Schematic diagram of a commercial FIB ion column[14].

After a first refinement through the spray aperture, the ion beam is condensed in the first electrostatic lens. The upper octopole then adjusts the beam stigmatism. The ion beam energy is typically between 10 and 50keV, with beam current varying between 1pA and 10nA. Using the variable aperture mechanism, the beam current can be adjusted over four decades, allowing both a fine beam for high-resolution imaging on sensitive samples and a larger beam for fast and rough milling. Typically, seven values of beam current can be selected. Their exact values depend on the machine type and the users' preferences.

Blanking of the beam is accomplished by the blanking deflector and aperture, while the lower octopole is used for raster scanning the beam over the sample in a user-defined pattern. In the second electrostatic lens, the beam is focused to a fine spot, enabling a best resolution in the sub-10nm range. The multichannel plate (MCP) is used to collect secondary particles for imaging.

1.2.2 Work chamber

The samples that are treated by a FIB are mounted on a motorized five-axis stage, inside the work chamber. Under normal operating conditions, inside this stainless-steel chamber a vacuum in the low 10^{-7}mbar range is maintained. Loading and unloading of the samples is usually performed through a loadlock, in order to preserve the vacuum inside the work chamber as much as possible. It typically takes a few minutes to load or unload a sample.

1.2.3 Principle of FIB imaging, milling and deposition

When energetic ions hit the surface of a solid sample, they lose energy to the electrons of the solid as well as to its atoms. The most important physical effects of incident ions on the substrate are: sputtering of neutral and ionized substrate atoms (this effect enables substrate milling), electron emission (this effect enables imaging, but causes charging of the sample), displacement of atoms in the solid (induced damage) and emission of phonons (heating). Chemical interactions include the breaking of chemical bonds, thereby dissociating molecules (this effect is exploited during deposition).

1.2.3.1 Imaging

As illustrated in figure 1.3(a), during FIB imaging, the finely focused ion beam is raster scanned over a substrate, and secondary particles (neutral atoms, ions and electrons) are generated in the sample. As they leave the sample, the electrons or ions are collected on a biased MCP detector. The detector bias is a positive or a negative voltage, respectively, for collecting secondary electrons or secondary ions. The secondary ions that are emitted can be used for secondary ion mass spectroscopy (SIMS) of the target material in a mass spectrometer attached to the system.

Inevitably, during FIB operations, a small amount of Ga^+ ions are implanted in the sample, and large numbers of secondary electrons leave the sample which cause sample charging problem especially on insulating sample materials. To prevent positive surface charges from building up, the substrate can be flooded with electrons from a separate electron source (only when collecting secondary ions for imaging). The system thus prevents damage due to electrostatic discharge and it enables imaging of non-conducting materials such as glass (which is often used in microsystems).

1.2.3.2 Milling

The removal of sample material is achieved by using a high ion current beam. The result is a physical sputtering of sample material, as illustrated schematically in figure 1.3(b). By scanning the beam over the substrate, an arbitrary shape can be etched. Typical sputtering yield varies for various materials, incident angle and energy. However, these number cannot be used directly to calculate the etch rate, because, depending on the scanning style, redeposition occurs, which drastically reduces the effective etch rate.

1.2.3.3 Deposition

FIB enables the localized maskless deposition of both metallic and insulating materials. The principle is chemical vapor deposition (CVD) and the occurring reactions are comparable to, for example, laser induced CVD. The main difference is the better resolution but lower deposition rate of FIB.

The deposition process is illustrated in figure 1.3(c); the precursor gases are sprayed on the surface by a fine needle (nozzle), where they are adsorbed. In a second step, the incending ion beam decomposes the adsorbed precursor gases. Then the volatile reaction products desorb from the surface and are removed through the vacuum system, while the desired reaction products remain fixed on the surface as a thin film. The deposition material is not fully pure however, because organic contaminants as well as Ga^+ ions (from the ion beam) are inevitably included.

The smallest features that can be deposited are of the order of 100nm (lateral dimension). The minimal thickness is about 10nm. Aspect ratios between 5 and 10 are obtained, at a typical deposition rate of $0.05\mu m^3 s^{-1}$.

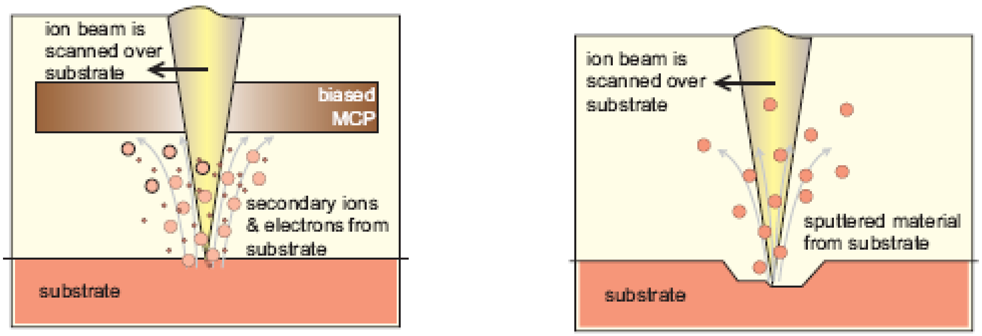

(a) (b)

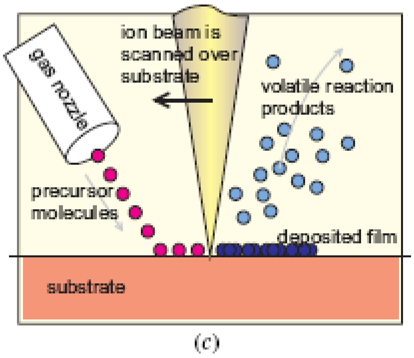

Figure 1.3: Principle of FIB (a) imaging, (b) milling and (c) deposition[1].

1.3 FIB Application and limitation-Motivation on new ion beam systems development

1.3.1 Metal beam implantation and contamination

Low energy focused ion beam systems are versatile tools frequently used for high precision surface processing. With diameters below 10nm, focused ion beams not only allow local removal and deposition of material by physical sputtering or ion induced chemistry, but it can also be used for high resolution scanning ion microscopy (SIM). Common areas of application for FIB are the modification of integrated circuits, the preparation of TEM samples, failure analysis, mask repair, micro machining, ion doping, direct resist writing and the processing of nano-structures with dimensions less than 100nm and high aspect ratio.

Conventionally, a liquid-metal ion source is used which, due to their small emission area and high brightness (>10^6A/cm.sr), enables small beam diameters and current densities between 2 and 10 A/cm^2. During the processing of target material with focused ion beams, simultaneously to the intended surface modification (sputtering, deposition of a defined volume), there is always modification of the sample surface by swelling, unintentional sputtering, ion implantation, and defect generation. Due to the high current density of the focused ion beam, these changes not only occur during milling and deposition but they also take place during imaging by scanning ion microscope (SIM), inspection and navigation. To some extend these side-effects do limit the application of FIB micro-machining.

Currently, high resolution ion beam processing is limited to mostly gallium ion beams. Gallium implantation and contamination, as well as defect generation occur during the processing. For practical applications, both effects have to be minimized. For example, when LMIS is used for sputtering of copper, a Cu_3Ga phase alloy can be formed, which is particularly resistant to milling and contributes to the uneven profiles.[15] L. Scipioni and coworkers [16] have demonstrated that when gallium ion beam is used for photo mask repair, implanted gallium ions can absorb 73% of incident 248 and 193nm ultraviolet light. However only 0.7% of the incident light is absorbed when krypton ion beam is used for mask repair. It has been shown that even for low dose applications (inspection), gallium is implanted up to peak concentrations of $5x10^{19}$ cm^{-3}. For material processing, peak ion concentrations of $6x10^{21}cm^{-3}$ are required. For extended FIB processing in nano-structuring and in sensitive devices, care has to be taken with respect to gallium dose to the sensitive area.

One way to address the contamination issue is to eliminate the source of contamination which is the gallium ion beam. If a non-gallium gas phase ion source can replace the LMIS to generate focused ion beam of similar size, the contamination can be greatly reduced and can even be eliminated completely. Furthermore, if the source has some flexibility to generate several ion species, one can select the most suitable species for a specific application. For example, when graphite is the sample to be processed, O_2^+ ion beam will be a good candidate to use. It won't cause any contamination like Ga^+ ions. In the meanwhile, the chemical reaction between oxygen and carbon also generates a volatile byproduct, which reduces the redeposition of the sputtered C debris greatly and results in a much cleaner cross-section.

1.3.2 Sample charging issues

Sample surface charging is another important issue associated with the FIB application. When a sample is irradiated by the primary ion beam, primary ions, secondary ions and secondary electrons produce a net electric current at the sample surface. If the sample material conducts, the current flows through the sample into the instrument grounding. However, insulating samples undergo charge buildup. For scanning ion microscope (SIM) sample charging can diffuse the primary beam out of the analytical area and eliminate secondary ion/electron signal. When the focused ion beam is used for circuit modifications, FIB-induced charging changes transistor parameters, such as threshold voltage (V_{th}) and sub-threshold swing, and in some cases, destroys the device during processing.[17,18] Several techniques are available to manage sample charging, and they are often used in combination.

Electrons compensate for positive charge buildup which results from positive primary ions and/or negative secondary ions and electrons. In this case, low energy electron beams work better because higher energies produce more than one secondary electron for every incoming electron.

Conducting grids placed over the sample reduce the effects of charging on ion optics and bring a source of electrons near to positively charged area of the sample. When struck by a primary ion, the conductors emit secondary electrons that migrate to the charging area. Similarly, samples are often coated with conducting materials such as gold or carbon for SIM applications. Before starting the analysis, the coating must be sputtered away, but only in the analytical area.

A continuously variable voltage offset can be applied to the accelerating voltage for samples that are only slightly charged up. Automatic voltage offset procedures are often incorporated into instrument control software. The software invokes an energy distribution measurement and adjusts the voltage offset as needed to keep the peak of the distribution constant[19]. There are also some other ways for charge compensation. But each method requires extra part (software or hardware) integrated to the system, and has its own limitations.

1.3.3 Throughput increase for semiconductor processing

For a single beam operation, it is always throughput limited, which makes the ion beam tool not suitable for mass production. Tools using a single scanning-ion beam to write patterns directly have not been widely accepted in manufacturing environments, essentially because of the long time required to write over a production-sized sample. In an exposure strategy in which the entire sample area A is scanned by a single ion beam with a beam spot size a and ion current I, if the required dose is Q for one pixel, the time to write the whole sample is given by:

$$t = \frac{A * Q}{a * I} \qquad \text{1-1}$$

In a production environment, it would give a great economic benefit to achieve a high throughput. In other words, the capability of improving throughput will effectively extend the application of ion beam tools especially in the semiconductor manufacturing industry. There are several possible ways to achieve the goal: first, to further increase the beam brightness, which is already as high as 10^6A/cm^2 sr for a convention FIB system[20]. The other way is to reduce the whole processing time t by increase the effective exposure area “a”. In order to achieve this, one way is to have an ion beam tool capable of transferring patter directly, which means to form a certain pattern in one exposure shot instead of scanning every single pixel one by one. By transferring the patterns directly with one shot, the complicated beam switching and scanning process are eliminated, thus improving the throughput. The concept is illustrated in figure 1.4. But in order to transfer patterns other than round dots, rectangular shaped pattern for example, the beam extraction aperture (the mask) needs to be specially designed. Since ion beams coming out from different part of the pattern have different demagnifications and aberrations, this will eventually cause the deformation of the transferred pattern. A lot effort needs to be taken on designing and fabricating the pattern on the mask, which will also result in a high cost of the mask. Beam optical column design will be another big issue to be resolved. The other approach to increase the effective exposure area “a” is to extend the single beamlet formation to multiple-beam generation. Therefore, multiple patterns can be processed at the same time. The process can be orders of magnitude faster than a single beam process, depending on how many beamlets are formed simultaneously. The concept schematic is shown in figure 1.4b.

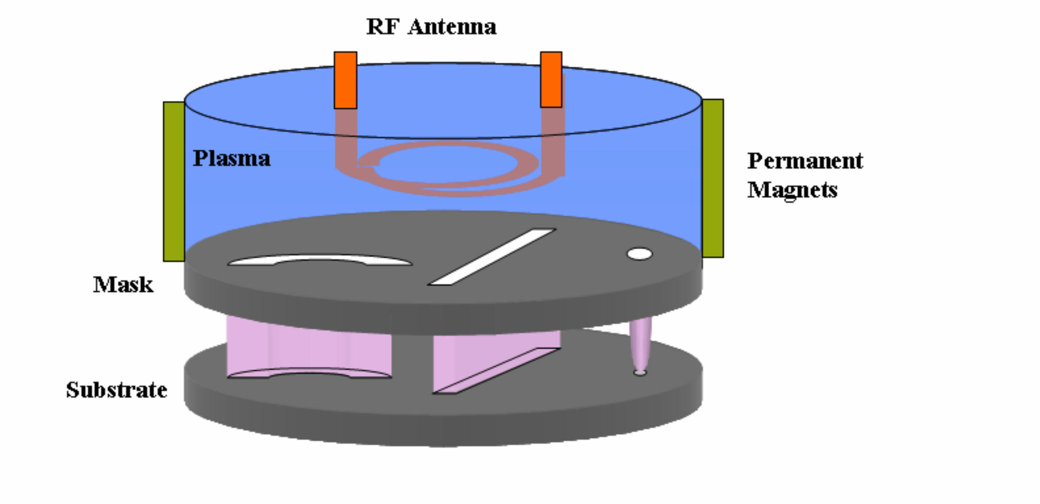

Figure 1.4a Concept of direct patterning[21].

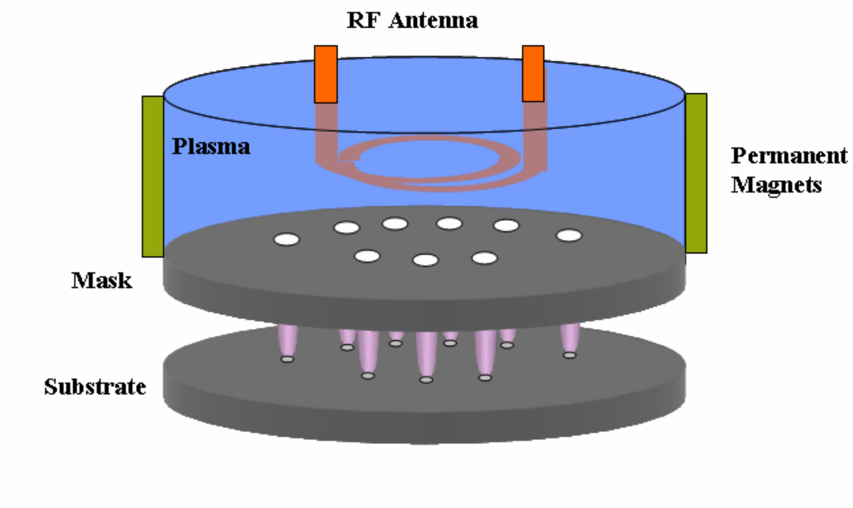

Figure 1.4b Concept of multiple-beamlets processing.

It is very obvious that neither scheme is achievable by LMIS. The mechanism of the liquid metal ion generation has determined that liquid metal ions can only be formed in a tiny round spot, and the engineering complexity has severely limited the possibility of integrating tens or hundreds LMIS together to make FIB array. But the two scenarios can be realized by a plasma ion source which is capable to generate plasma with large area uniformity, for instance, the multicusp plasma ion source. By manipulating the shape of the aperture on the beam forming electrode, ions can come out of the ion source as a single focused ion beam, a shaped ion beam pattern or as an ion beam arrays.[21]

1.3.4 New ion beam systems development

The concerns over gallium contamination, charging and low throughput have severely limited the opportunities for semiconductor fabrication lines to get the rapid critical dimension control information that could be gained if FIB metrology systems were placed inline. Because of these factors, there is a great motivation to develop "non-gallium" focused ion beams suitable for such applications.

Attempts to develop an inert species FIB system have been undertaken. Several investigators have considered the gas field ion source as an alternative to LMIS[22]. With an image-side brightness of 10^9-10^{10} A/cm.sr^2 at 30-50keV and an energy spread of 1eV, this source could provide excellent performance. Unfortunately, the source is limited to operating with light ions at lower currents, so it is not efficient for high speed milling applications. Also, there are many challenging technical requirements for the source and associated optics. All of these have until this time prevented a practical incarnation of GFIS FIB system from being developed.

Another option for producing a beam of gaseous ions is to extract from a plasma. A plasma source is very flexible at generating various ion species, from very light ions like H^+, D^+, T^+, and He^+, to medium mass ions like Ar^+, P^+, O^+ even to very big molecular ions like C_{60}^+ [23]. It is also achievable for plasma source to generate metallic ions such like Cu^+, Pd^+, Ni^+ etc. Basically, ions of nearly of all the elements in the periodic table can be produced with a plasma source. It is also not difficult for such a source to meet the ion current requirement for various applications. The main issue with these sources is the low source brightness.

There has been work performed on the use of the multicusp plasma ion source for focused beam applications[24]. This source has the advantages of a low energy spread[25] $\Delta E \leq 1\text{eV}$ and low ion temperature, T_i= 0.1eV. What is most interesting, however, are the predictions of high axial brightness (10^5A/cm^2 sr at 75keV) that have been made for the source, based on calculation[26]. The multicusp plasma source has many advantages that make it very useful for a FIB system, especially for contamination-critical applications such as inline metrology and defect review or photomask repair. It provides a stable ion beam and is simple to use.

As a conclusion, compared with LMIS, plasma based ion source has several advantages and disadvantages. The source brightness is right now two orders of magnitude lower and beam spot size of nanometers has not been achieved experimentally yet. But plasma-based ion source has a high flexibility in generating a variety of ion species, thus meets the various requirements in nanofabrication applications. Also, the capability of generating large area uniform plasma has made this kind of source a promising candidate for next generation high-throughput ion beam tool.

The drive towards controlling materials' properties at nanometer scales relies on the availability of more flexible tools. Driven by the more and more strict requirements from FIB related applications, several novel ion beam systems utilizing plasma-based ion sources have been developed at Lawrence Berkeley National Laboratory, such as: a FIB/SEM dual beam system, a combined electron- and ion-beam system, and a compact sputtering metallic ion source. The systems will be discussed in details in chapter 2 to chapter 5, and will be summarized in chapter 6.

Reference:

[1] Melngailis J "Critical review: focused ion beam technology and applications", *J. Vac. Sci. Technol.* B 5, 469 (1987).

[2] Stewart D. K., Doyle A. F. and Casey J. D. Jr., "Focused ion beam deposition of new materials: dielectric films for device modification and mask repair, and Ta films for x-ray mask repair" *Proc. SPIE* 2437, 276 (1995).

[3] Reyntjens S., De Bruyker D. and Puers R.., "Focused ion beam as an inspection tool for microsystem technology" *Proc. Microsystem Symp.* 125 (1998).

[4] Ward B. W., Economou N. P., Shaver D. C., Ivory J. E., Ward M. L. and Stern L. A., "Microcircuit modification using focused ion beams" *Proc. SPIE* 923, 92 (1988).

[5] Glanville J., "Focused ion beam technology for integrated circuit modification" *Solid State Technol.* 32, 270 (1989).

[6] Stewart D. K., Stern L. A., Foss G., Hughes G. and Govil P. "Focused ion beam induced tungsten deposition for repair of clear defects on x-ray masks" *Proc. SPIE* 1263, 21 (1990).

[7] Daniel J. H. and Moore D. F., "A microaccelerometer structure fabricated in silicon-on-insulator using a focused ion beam process" *Sensors Actuators* A 73**,** 201 (1999).

[8] Brugger J., Beljakovic G., Despont M., de Rooij N. F. and Vettiger P., "Silicon micro/nanomechanical device fabrication based on focused ion beam surface modification and KOH etching" *Microelectron. Eng.* 35 401 (1997).

[9] Y. Zengliang, Y. Jianbo, W. Yuejin, C. Beijiu, H. Jiangun, H. Yuping, *Nucl. Instr.*

and Meth. B 80/81, 1328 (1993).

[10] Y. Hase, A. Tanaka, I. Narumi, H. Watanabe, M. Inoue, *JAERI Rev*. 98-016,81 (1998).

[11] S. Anuntalabhochai, R. Chandej, B. Phanchaisri, L.D. Yu, T. Vilaithong, I.G. Brown, *Appl. Phys. Lett*. 78, 2393 (2001).

[12] B. Phanchaisri, L.D. Yu, S. Anuntalabhochai, R. Chandej, P. Apavatjrut, T. Vilaithong, I.G. Brown, *Surf. Coat. Technol*. 158/159, 624 (2002).

[13] Qiao Y, Chen J, Guo XL, et al. "Fabrication of nanoelectrodes for neurophysiology: cathodic electrophoretic paint insulation and focused ion beam milling Nanotechnology" 16 (9): 1598-1602 (2005).

[14] S. Reyntjens and R. Puers, J. Micromech. *Microeng.* 11 287-300 (2001)

[15] J. David Casey. Jr., Michael Phaneul and Clive Chandler, Abstracts of the 46th EIPBN conference, 361 (2002).

[16] L. Scipioni, D. Stewart, D. Ferranti, and A. Saxonis, *J. Vac. Sci. Technol*. B 18, 3194 (2000)

[17] A. N. Campbell, K. A. Peterson, D. M. Fleetwood and J. M. Soden: *Proc. Int. Reliability Physics Symp*., IEEE, Piscataway, NJ, 72 (1997).

[18] J. Benbrik, P. Perdu, B. Benteo, R. Desplats, N. Labat, A. Touboul and Y. Danto: *Proc. Int. Symp. Plasma Process-Induced Damage*, IEEE, Piscataway, NJ, 128 (1998).

[19] A. Benninghoven, F.G. Rudenauer, and H.W.Wemer, "Secondary ion mass spectrometry: Basic concepts, instrumental aspects, applications, and Trends", Wiley,

New York, (1987).

[20] N.S. Smith, D.E. Kinion, P.P. Tesch and R.W. Boswell, "A high brightness plasma source for focused ion beam applications", *Microsc Microanal* 13, 180 (2007).

[21] Q. Ji, T.-J. King, K.-N. Leung, S. B. Wilde, "Production of various species of focused ion beam", *Rev. Sci. Instru.*, Vol 73, 822 (2002)

[22] R. Borret, K. Jousten, K. Bohringer, and S. Kalbitzer, *J. Phys.* D 21, 1835 (1988).

[23] Q. Ji, Y. Chen, L. Ji, S. Hahto, K. N. Leung, T.G. Lee, and D.W. Moon, "Development of C_{60} plasma ion source for time-of-flight secondary ion mass spectrometry applications", presented at 2007 international conference on Ion Source (ICIS) 2007.

[24] K.N. Leung, *J. Vac. Sci. Technol*. B 17, 2776 (1999)

[25] Y. Lee, K.N. Leung, *Nucl. Instrum. Methods Phys. Res*. A 374, 1 (1995)

[26] X. Jiang, Ph.D. dissertation, University of California, 2006.

Chapter 2:

A plasma-source based focused ion beam system

Current research to understand the science associated with mesoscale structures has shown the need for new approaches to fabricate of future small-scale devices. For many applications, gallium is an undesirable contaminant. Therefore, conventional FIB systems which utilize liquid gallium ion sources to achieve nanometer resolution severely limit applications and fundamental studies. Technology for selectively doping or modifying nanoscale device structures is needed to eliminate complex masking that become increasingly difficult as device dimension shrinks. Lack of integrated diagnostics in conventional systems also limits the information available from nanofabrication experiments. An integrated FIB/SEM dual-beam system will not only improve the accuracy, resolution and reproducibility when performing ion beam sculpting[1] and direct implantation processes, but also enable researchers to perform cross-sectioning, imaging, and analysis with the same tool.[2,3]

In this chapter, a FIB/SEM dual beam system is introduced. It employs a mini-RF driven plasma source[4] to generate various ion species of focused ion beams[5], a FEI two-lens electron (2LE) column for SEM imaging, and a five-axis manipulator system developed by Zyvex Corporation. It is developed for direct doping or surface modification. The advantage of this system over existing ones is that a plasma source instead of a LMIS is employed, allowing ions of almost all elements in the periodic table to be generated for diverse research purposes. The FIB/SEM dual-beam system is being developed as a joint effort between Harvard University and Lawrence Berkeley National Laboratory.

2.1 Ion Source

A mini-RF plasma source is employed in the system to produce various ion species[4]. As shown in Figure 1, it consists of an alumina (Al_2O_3) ceramic chamber with 1.5 cm inner diameter and a double-layer copper wire which act as an external antenna. Both ends of the ceramic chamber are covered with metal flanges. Contamination is minimized because O-ring seals are replaced with hard seals between the ceramic and metal joints.

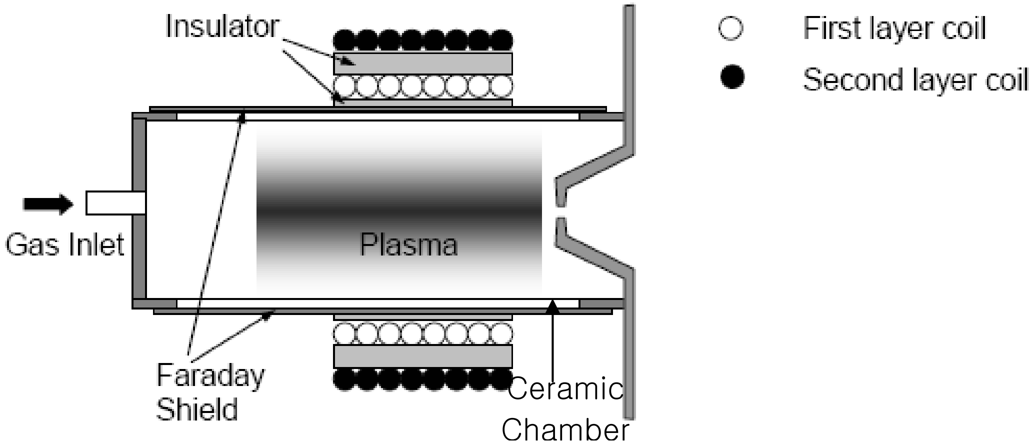

Figure 2.1: Schematic diagram of a mini-rf plasma source, which consists of an alumina (Al_2O_3) ceramic chamber with 1.5 cm inner diameter and a double-layer of copper wires as external antenna. To minimize capacitive coupling, faraday shielding is wrapped outside the chamber .

2.1.1 Antenna configurations

The antennas are made of 1-mm-diameter thin copper wire. It has insulation coating on the surface and therefore it can be wrapped tightly on the outside of the mini ion source chamber. Both single and double layer antenna coils have been tested. Since the volume surrounded by the double layer coils is less than the volume covered by single layer coils of the same turns, the power density is higher when double layer coils are used at the same RF power.

There are two kinds of antenna configurations for the double layer antenna coils: coils in series and coils in parallel. When double layer coils are wrapped in series, the coils are wound starting close to the first electrode and moving away in successive turns, followed by a Teflon layer of insulation. The coils are then wound in the opposite direction returning to the extraction on the surface of the Teflon insulation layer. In this case, the two ends of the coils are very close. A good insulation is needed to hold the high voltage drop between the two layers, especially at high RF power. When parallel double layer coils are used, two separate antennas of about the same length are wrapped spirally from the extraction to the other end of the plasma chamber with a Teflon insulation layer between the two layers. In this case, the voltage drop across the two layers of the coils is minimized. Capacitive discharge is induced by the voltage difference between the two ends of the coils which can be minimized if the antenna coils are wrapped in parallel in double layers. Because of the higher power efficiency in an inductive discharge, the double layer antenna coils can generate the plasma discharge at rather low RF power and it also can sustain higher

RF power without voltage breakdown across the insulation layer. For this reason, the double-layer antenna coil in parallel is used. The double layer antenna produces better plasma coupling for a given RF input power, and it has a higher power density compared to a single layer antenna arrangement. As a result, the extractable ion current density is higher. A 30% higher extracted ion current has been measured using the double layer antenna during the experiment.[4]

2.1.2 Operation mode

Both inductive and capacitive coupling plasmas can be ignited by using this mini-RF plasma ion source. Inductively coupled plasmas are more efficiently than capacitively coupled plasma for ion beam production. The inductive plasma has relatively low plasma potential and higher power efficiency. Low plasma potential can decrease the ion bombardment energy to the chamber walls, thus reducing the sputtering damage.[6,7] The plasma potential in capacitively coupled discharge can be over 100 V [8] while the plasma potential in inductively coupled discharge can be lower than 10 V when operated at low gas pressure operation region (tens mTorr).[9] The sputtering yield for 100 eV argon ion on molybdenum is 2 atoms/ion, but the sputtering yield is almost zero when the energy of the argon ion is lower than 10 eV. When an external antenna is employed in the plasma generator, the ceramic wall of the ion source will be coated by a thin metal film if sputtering damage from the metal electrode is significant. The thin metal film around the ceramic wall will shield the RF field and therefore decrease the power efficiency. In the meanwhile, the thin layer of metal film will heat up under the RF, causing alumina chamber wall to crack under different heat expansion thus limiting the lifetime of the ion source. With existence of the thin metal film, it changes the matching network, therefore the plasma is not stable. High power efficiency is the result of minimal electron and ion power dissipation in inductive discharge.

2.1.3 Other features of the mini RF source

Coupling of the RF power to the plasma is much reduced when a metallic coating is formed on the inner surface of the ion source chamber. A Faraday shielding is normally employed to further minimize capacitive coupling. In this case, the Faraday shielding is consisted of three copper strips which connect the two conducting ends of the source. With the Faraday shielding, the capacitive coupling is eliminated. The source has been operated for hours with and without the Faraday shielding for comparison. Without the shielding, the inner side of the source chamber is slowly grown with a very thin layer of sputtered metal film and the RF power coupling gradually changes after running for several hours. With the shielding, the source can be operated with good efficiency for the same time duration.

But even with the help of the Faraday shielding, the very slow metal thin film deposition on the inner side chamber still can not be eliminated. Further modification on the configuration of the inner side chamber has been performed. By installing several small quartz rods on the inner side chamber wall, the inner surface of the chamber is divided into several sessions. With this configuration, a complete circuit loop introduced by the metal film can not form on the chamber wall any more. The source has been continuously running for several hours with very stable performance.

When an RF signal is applied to the antenna, the coils dissipate power. With the presence of the plasma, heat can be conducted to the coils. These combined heat effects could crack the ceramic wall. Thermally conductive adhesive, which is also a good dielectric material, is used for heat conduction purposes. Copper tubes, with water passing through, are attached to the surface of the plasma chamber for cooling purpose. A photograph of the complete ion source is shown in figure 2.2.

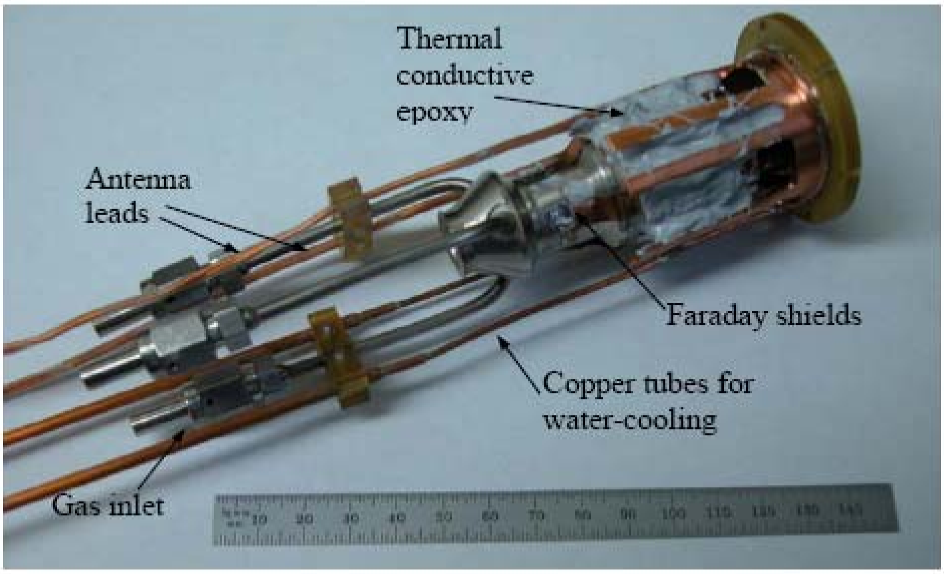

Figure 2.2: A photograph of the FIB ion source. Thermal conductive epoxy and copper tubes with water passing through are incorporated for better heat dissipation.

2.1.4 RF source ignition

To generate plasma, argon gas is introduced into both source chambers. For the mini RF source, because of the small volume of the source, electrons are relatively easy to get lost on the source chamber wall. The mean free path λ of the electron can be expressed as:

$$\lambda = \frac{1}{n \cdot \sigma} \tag{2-1}$$

where n is the number of the gas molecules per unit volume, σ is the collision cross section. To ignite a high-density plasma, the electrons must perform enough collisions before they are lost on the source chamber wall, which means the mean free path of the electrons should be smaller than the case in a bigger source chamber. Therefore, to start an inductively discharge plasma in the mini RF source, the gas pressure should be much higher than in a big source.

For our mini RF source with an inner diameter of 1.5 cm, usually 60W RF power and 100 mTorr gas pressure are used to ignite the inductively discharge plasma. When the gas pressure is not high enough, a dim capacitive discharge plasma is ignited first. The plasma density goes higher with the gas pressure. When the gas pressure is high enough (above 100 mTorr), the plasma jumped into a much brighter mode and the inductively coupled plasma thus is ignited. After the ignition, the source can then be operated at lower gas pressure (20 mTorr) and lower RF power (the plasma can be sustained at an RF power under 20W).

2.1.5 Current density measurement

The extracted current density of the mini RF source has been measured using a single gap extraction. The diameter of the extraction aperture on the plasma electrode is 50 µm, and the distance of the gap between the plasma electrode and the extractor is 1mm. The extracted ion current is collected on a Faraday cup. The current density at the extraction side thus is the current collected by the Faraday cup divided by the area of the extraction aperture.

$$J = \frac{I}{S} = \frac{I}{\frac{\pi}{4} d^2} \qquad 2\text{-}2$$

Where J is the current density at the extraction side, I is the total current measured at the Faraday cup, S is the area of the extraction aperture and d is the diameter of the aperture.

Argon gas is introduced to generate the plasma. As shown in figure 2.3, the Ar^+ ion current density increases with the input RF power. Through a 50-µm-diameter extraction aperture, the Ar^+ current density as high as 100 mA/cm^2 has been achieved with only 150 W of RF input power. This current density is comparable to a 7.5 cm diameter multicusp ion source operated at an input RF power of over 1 kW.[10] The beam current density is measured and plotted as a function of input RF power (figure 2.3a, extraction voltage is fixed at 1.5kV) and extraction voltage (figure 2.3b, RF power is fixed at 50w).

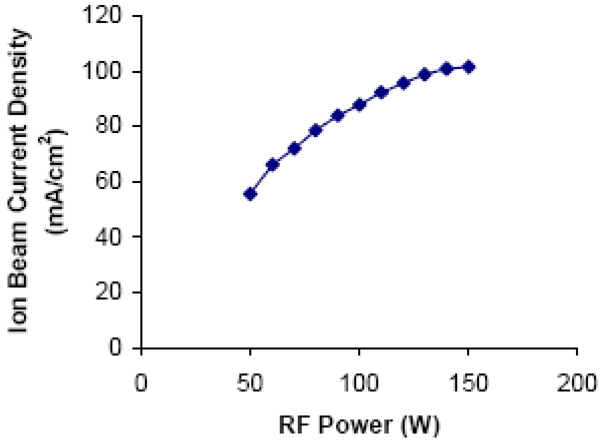

Figure 2.3a: Ar^+ ion beam current density extracted from the source through a 50-µm diameter aperture, as a function of input RF power, the gas pressure is 35mTorr.

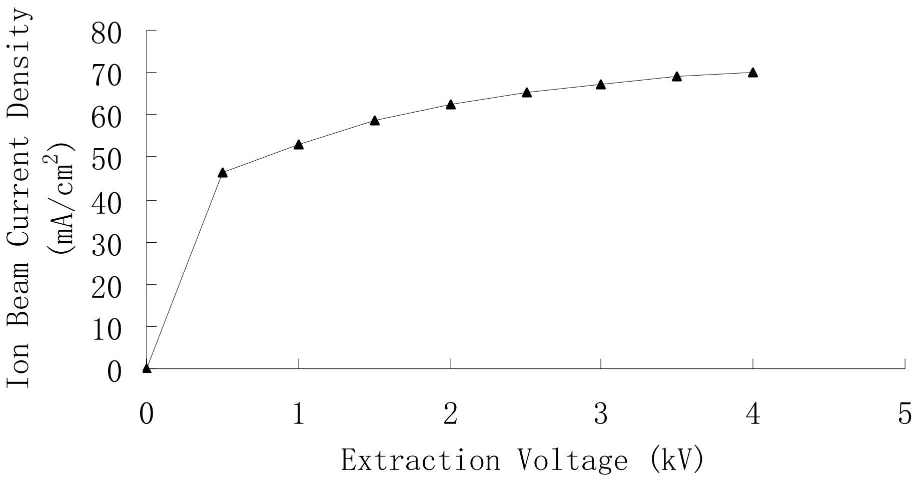

Figure 2.3b: Ar$^+$ ion beam current density extracted from the source through a 50-μm-diameter aperture, as a function of extraction voltage.

Besides Argon, the mini source can also be operated with other gaseous species like helium, krypton, oxygen, hydrogen, nitrogen and so on. The maximum current density calculated by the Child-Langmuir equation is:

$$j = \frac{4 \cdot \varepsilon_0}{9} \sqrt{\frac{2 \cdot q}{m}} \cdot \frac{\phi^{3/2}}{d^2} \qquad \text{2-3}$$

where ε_0, m, q, ϕ, and d are the permittivity of free space, the mass of ion, the ion charge state, the extraction potential and the extraction gap distance respectively. Since the current density is inversely proportional to the square root of mass, the extracted current density should be lower for species with higher mass like krypton, and higher for species with lower mass e.g. hydrogen.

But according to the experimental result, at lower RF power, the difference between the current densities of krypton and argon is very small and the current density of krypton is even higher than that of argon when the RF power is very low[4]. That is because krypton has a lower ionization potential and higher ionization cross-section than argon, which makes it easier to ionize. So at a low RF power, the plasma density of krypton can be higher than that of argon. The saturation value of ion current density that can be extracted from a plasma of certain density is given by:

$$j_s = 0.6 \cdot n_i \cdot q \cdot \sqrt{\frac{kT_e}{m}} \qquad 2\text{-}4$$

where n_i and T_e are plasma density and electron temperature respectively. This saturation current is proportional to plasma density; though the mass of krypton is heavier than argon, a higher current density for krypton at low RF power can be extracted from the plasma due to higher plasma density. The measured current densities level off at high RF power. When the plasma density is too high, the plasma meniscus will protrude out, and the extracted ion beam will have larger angular divergence. Some of the ions will be blocked by the extraction electrode and lost. This means that a higher electric field is needed to extract more current from higher density plasma.

2.2 Ion acceleration column

2.2.1 Aberrations in ion optics[11]

A conventional optical system consists of several rotationally symmetric (round) lenses which enable light to be focused and imaged. Ion optical imaging system also consists of several rotationally symmetric lenses that enable the ions to be focused and imaged. Similar to a light optical imaging system, the action of the ion optical system is to transfer the image from the object plane to the image plane. In the paraxial approximation, the ion optical system can form an ideal and clear image, but when aberration is present the image is distorted and unclear[12].

2.2.1.1 Aberrations in optics

The property of a lens has linear quantities such as focal length, position of foci, principle planes and nodal planes. But besides these low order terms, there exist perturbations to the imaging property of the lens. The deviations from the perfect images are called aberrations. The definition of aberrations in charged particle optics is very similar with light optics. The third-order geometrical aberrations of round lenses can be written as[13]:

$$\Delta u_i = C r_a^2 u_a \qquad \text{(Spherical aberration)} \tag{2-5}$$

$$+2(K+ik) r_a^2 u_0 + (K-ik) u_a^2 u_0^* \qquad \text{(COMA)} \tag{2-6}$$

$$+(A+ia) u_0^2 u_a^* \qquad \text{(Astigmatism)} \tag{2-7}$$

$$+F r_0^2 u_a \qquad \text{(Field curvature)} \tag{2-8}$$

$$+(D+id) r_0^2 u_0 \qquad \text{(Distortion)} \tag{2-9}$$

$r_0^2 = x_0^2 + y_0^2 = u_0 u_0^*$ Here r_0, x_0, y_0, u_0, u_0* are the spatial coordinates on the object plane. And $r_a^2 = x_a^2 + y_a^2 = u_a u_a^*$ Correspondingly, r_a, x_a, y_a, u_a, u_a* are the beam coordinates on the aperture plane, which measure the beam angles.

2.2.1.2 Spherical aberration

The spherical aberration occurred when the rays far from the axis are focused more strongly than those closer to it. As a result, the peripheral rays are focused in front of the Gaussian focus and the paraxial rays are focused further away. The circle of least confusion has the minimum diameter and corresponds to the best possible focus in the presence of spherical aberration (figure 2.4). From equation 2-5, spherical aberration is proportional to the third power of the aperture coordinates, e.g. beam half angle. And it is of the greatest importance in the first (objective) lens of magnifying system and in the final lens of probe-forming systems.

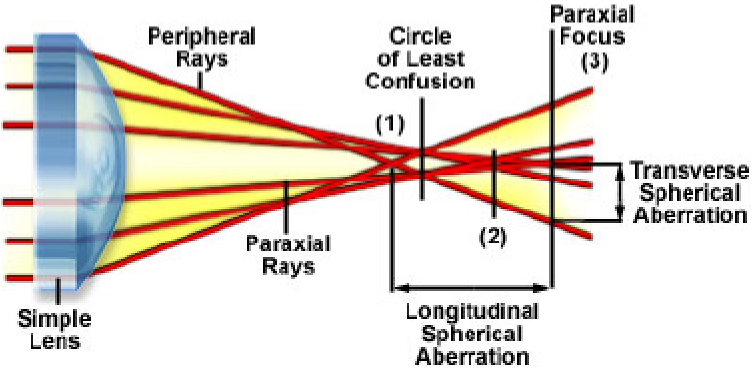

Figure 2.4: Formation and definition of spherical aberration in circular lens. Image courtesy of Olympus.

2.2.1.3 Coma aberration

For objective and probe-forming optics, coma aberration can be the next most important aberration after the spherical aberration if the rays are inclined to the axis at a relative steep angle.[12] Coma is similar to the spherical aberrations, but it is mainly encountered with off-axis rays. Coma is proportional to the first order of object off-axis position and the second order of the aperture angle. If off-axis incident rays that arrive on lens at different off-axis positions are focused to different heights, coma aberration is formed. The diameter of the spot increases with the incident angle. As a result, comet-like shape will be formed on the image plane. (figure 2.5)

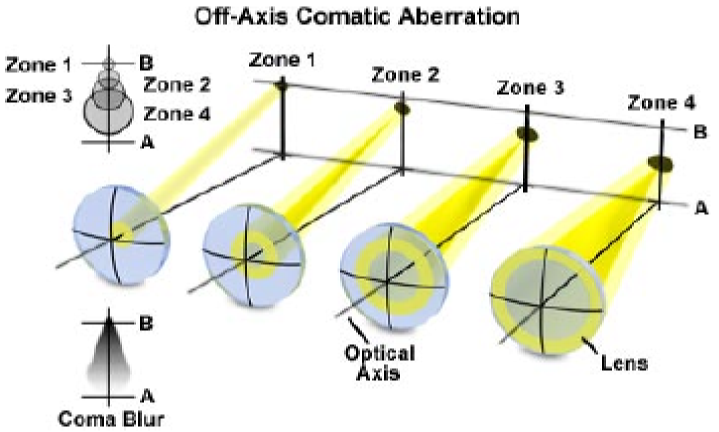

Figure 2.5: The mechanism of coma aberration formation. Image courtesy of Olympus.

2.2.1.4 Astigmatism and field curvature

Astigmatism and field curvature are usually the most important image blurs in charged particle projection optics because of the second order dependence to the object's spatial coordinates. They also change linearly with the beam half angle. When off-axis rays on the sagittal plane and the tangential plane are focused on different focal positions, astigmatism aberration will be formed, as shown in figure 2.6.

When rays are focused through a curved lens, the image plane produced by the lens will also be a curved surface (figure2.7). But usually the object and the image planes are flat. The curved Petzval surface will create an image blur on a flat image plane. This is called curvature aberration. Astigmatism and field curvature aberration can be dynamically corrected in probe beam systems (small-beam direct-write systems) or partially correct in projection system with variable axis, such as the PREVAIL system at IBM.

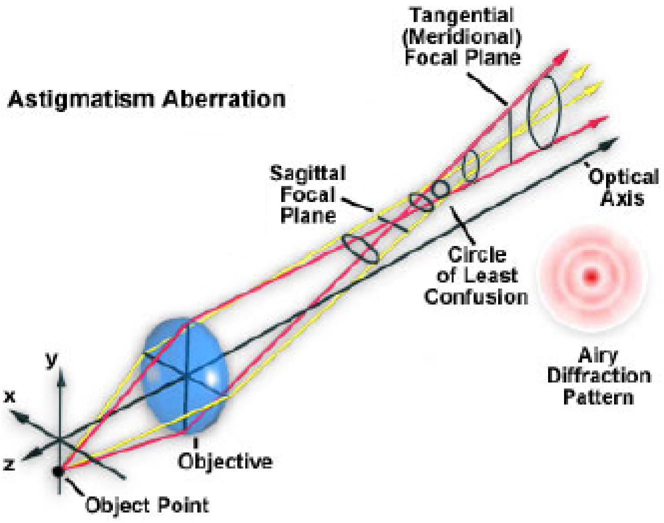

Figure 2.6: Astigmatism aberration. Image courtesy of Olympus.

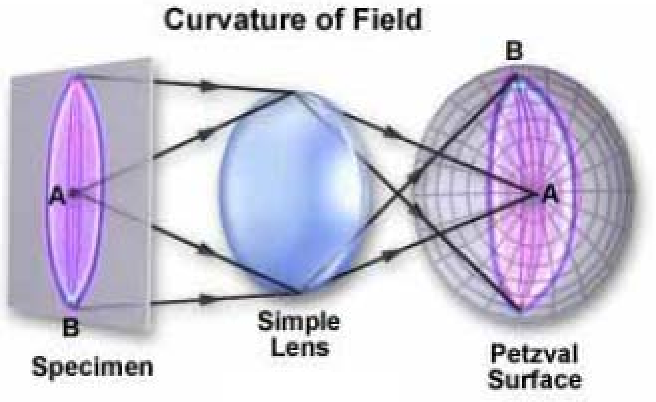

Figure 2.7: Field curvature aberration. Image courtesy of Olympus.

2.2.1.5 Distortion

Distortion aberration is of the most importance to large field projector systems. It is proportional to the third order of the object size according to equation 2-9. Unlike other aberrations, distortion does not cause image blur but merely destroy the proportionality between the image and the object coordinates. If $d=0$ and $D>0$ in equation 2-9, pincushion distortion exists in images (figure 2.8 B). If $d=0$ and $D<0$, the aberration is called barrel distortion (figure 2.8 C). Pincushion and barrel distortions are isotropic. They are created when lens magnification is dependent on off-axis positions. Magnetic lens rely on rotating the incoming electron or ion to generate focusing force. If the rotation angle changes with the off-axis position, it will create a special anisotropic distortion: spiral distortion (figure 2.8 D). Spiral distortion only exists in magnetic lenses.

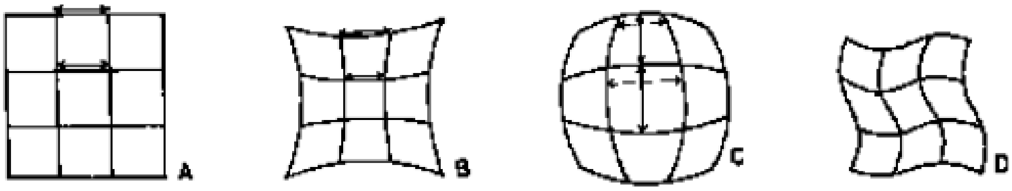

Figure 2.8: Distortion aberration. (A) Undistorted image; (B) Pincushion distortion; (C) Barrel distortion; (D) Spiral distortion

2.2.1.6 Chromatic aberration

The focusing power of an electrostatic or a magnetic lens depends on the energy of the incoming charged particles. Electron or ion sources can't produce exactly mono-energetic beams. And there are always some fluctuations in high voltage and current supplies for lenses. The energy spread will be broadened when charge particles pass through thin materials, such as a membrane mask used in the SCAPEL system at Lucent Technologies. The fluctuation of the beam energy will create another image blur-chromatic aberration, which has an axial component (axial chromatic aberration) and a radial component (shaped-beam chromatic aberration). Axial chromatic aberration is proportional to the product of $\alpha \cdot \frac{\Delta V}{V}$, here α is the beam angle, ΔV is the energy spread and V is the beam energy. Shaped-beam chromatic aberration changes linearly with $r \cdot \frac{\Delta V}{V}$, where r is the off-axis distance of the beam.

2.2.2 Ion beam accelerator column design

Charged particle optics column based on electrostatic and magnetic lenses has been studied for over a century. With more and more powerful computers readily available, complicated electrostatic or magnetic lens column can be simulated with a PC nowadays. Eric Munro and Xieqing Zhu have pioneered in the computer aided charged particle optics design since 1970s.[14] Their latest charged-particle optics design software package has been widely used in designing many high-resolution electron and ion beam imaging or lithography systems. The first step in their method is to calculate the magnetic and electrostatic field distribution with the first- or second-order finite element methods (FOFEM and SOFEM), the finite difference method (FDM) and the charge density method (CDM). Then the fields in the lens and the deflector are expended in series as powers of the off-axis distance. These field expansions are then substituted into ray equations. By excluding different orders of terms, first-order paraxial properties, third-order and fifth-order aberrations can be calculated.[15]

The first order optical properties are obtained by evaluating four paraxial rays: focusing ray, field ray, main-field deflection ray and subfield deflection ray. These paraxial rays have unit slope, position and deflection excitations. First order imaging and deflection properties can be extracted from the values of these rays at the image plane. The third-order/fifth-order aberrations can be calculated when third/fifth order expansions are included into the ray equation. And it can be solved through the methods of variation of parameters to yield certain aberrations in the form of an integral.[15] An alternative way to obtain the aberration coefficients is direct ray-tracing as long as the computation accuracy is high enough to obtain a reliable result.[16]

The goal of the ion optics simulation is to design a 35kV ion column to achieve a beam resolution of sub-100nm. The ion optics column for the dual beam system is simulated by employing the commercially available charged-particle optics design software: Munro.

An all-electrostatic column, as shown in figure 2.9 (a), has been designed to focus the ion beam extracted from the source. It consists of a total of five electrodes: a counterbored-shaped aperture as the plasma electrode, a second electrode for beam extraction and a three-electrode Einzel lens system.

2.2.2.1 The counterbore-shaped plasma electrode

Figure 2.9 (b) is a zoom-in view of the counterbore-shaped aperture. It can be described as a two-step aperture which have different diameters D_1 and D_2 and different thicknesses L_1 and L_2. As has been demonstrated in the previous research work by Qing Ji, a counterbored shaped plasma electrode is better than a single-hole aperture in reducing the beam aberration.[17] The plots in figure 2.10 shows how the geometry of the counterbore will affect the aberration. In this computation, a single-lens optics is simulated, ions are extracted through the counterbore-shaped aperture and image at 1mm distance. The aspect ratio of the first step is fixed at 5 with D_1= 50 μm and L_1=250 μm, and the diameter and the thickness of the second step are optimized to minimize the beam aberration. The spherical, coma, field curvature, astigmatism, distortion, and chromatic aberrations are plotted as the function of the diameter D_2 and the thickness L_2. In this case, the aberrations decrease when the diameter D_2 increase and reach the minimum value when D_2=300 µm, But the aberration didn't change significantly with L_2.

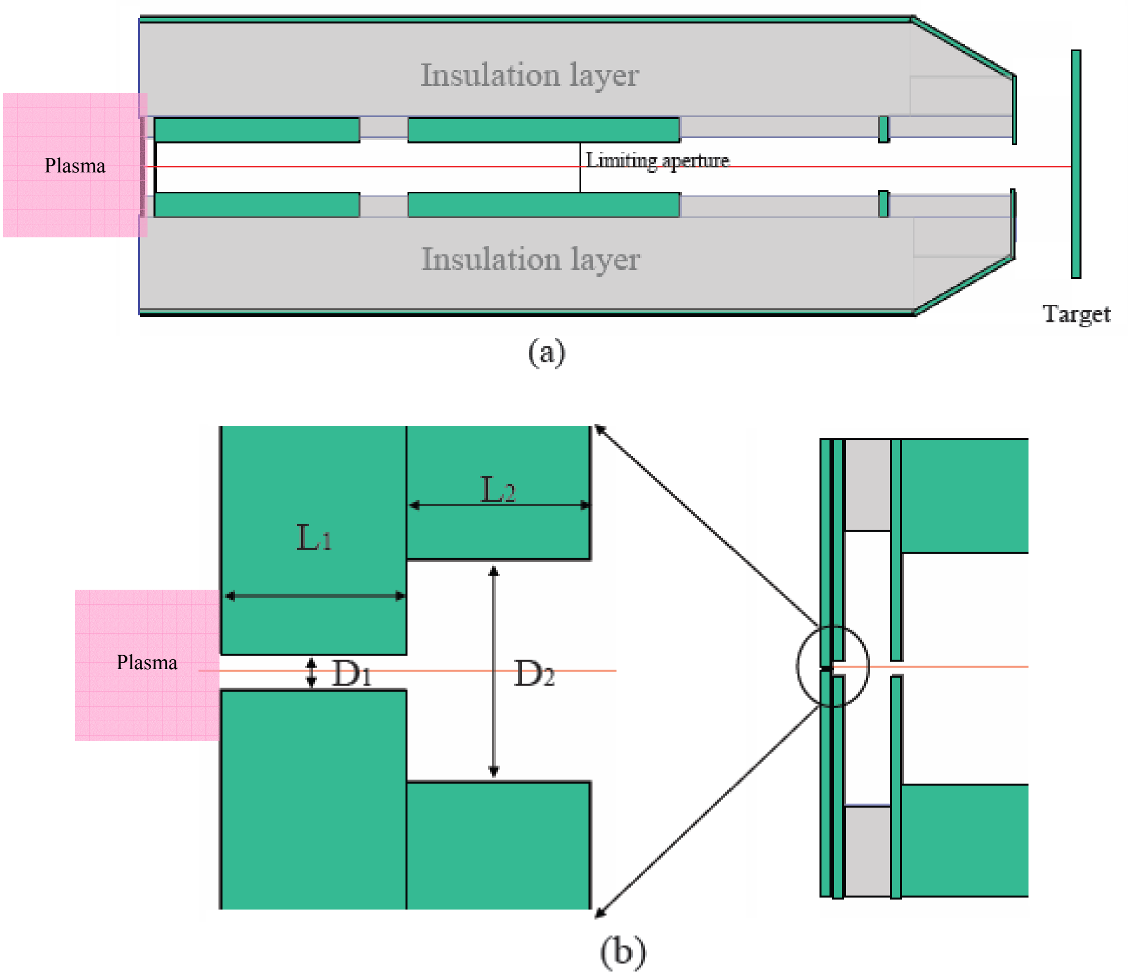

Figure 2.9: (a) Schematic of the all-electrostatic five-electrode accelerator column; (b) Zoom-in view of the counterbore-shaped aperture as the plasma electrode.

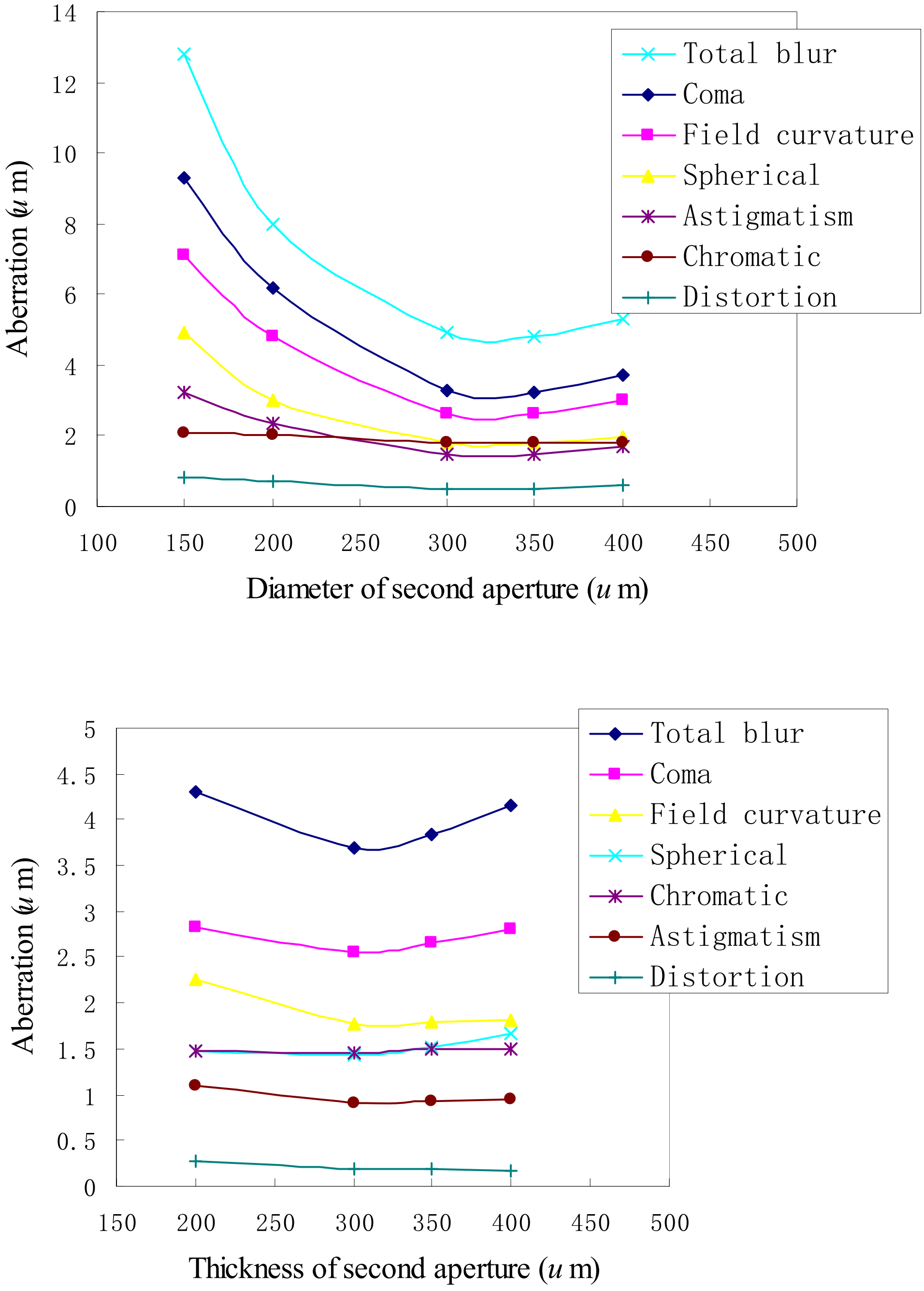

Figure 2.10: Aberration dependence on the diameter of counterbore-shaped aperture D_2 and on the thickness of the second step L_2 for D_1=50μm, L_1=250μm[17].

2.2.2.2 Limiting aperture

A big beam half angle α at the image plane will cause a large beam aberration. Since for the third-order geometrical aberrations (primary geometrical aberrations), the spherical aberration is proportional to α^3, coma is proportional to α^2, field curvature and astigmatism are proportional to α, the first-order chromatic aberration is also proportional to α[13], most of the aberration terms are related to the beam half angle α to a certain extent. Thus reducing the beam half angle is very important for achieving a small aberration. A limiting aperture is employed in the optics column design. It is installed in the middle of a very thick electrode, where the electric field is zero. It is essential for the limiting aperture to be installed in a field-free region; otherwise the electric field changes on both sides of the limiting aperture, the aperture will thus act as an additional electrostatic lens with extremely small diameter and generate additional aberration. The very thick electrode (27mm) ensures a field free region around the limiting aperture area. The potential distribution and its first and second order derivatives calculated by using the Munro code are shown in figure 2.11. As shown in the plot, the potential across the limiting aperture is a constant and the first and second derivatives are both zero at the limiting aperture plane.

The aberrations are plotted as a function of the diameter of the limiting aperture (shown in figure 2.12). For this 35kV optics column, spherical aberration and chromatic aberration are the most important aberrations. The spherical aberration is strongly related to the beam half angle. According to the calculation, the spherical aberration deceases to 1.6% when the diameter of the limiting aperture decrease from 200μm to 50μm, and the chromatic aberration decreases to 25% of the original value. The total aberration is greatly reduced but in the meantime, since the limiting aperture blocks beam with large half angles, some of the ion beam current is sacrificed.

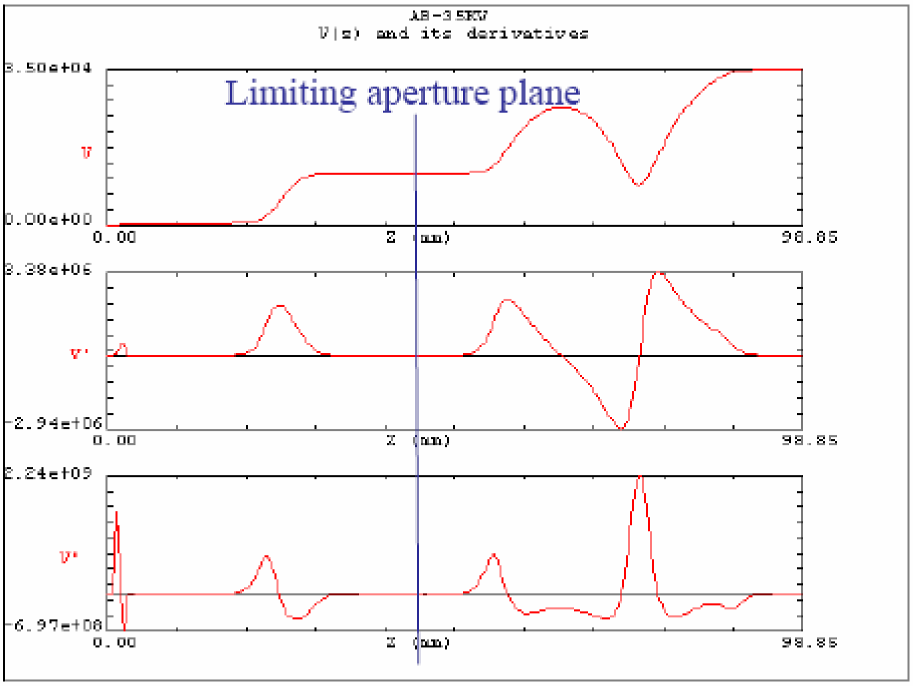

Figure 2.11: The axial potential distribution and the first and second order derivatives along the accelerator column, the blue line indicates where the limiting aperture plane locates.

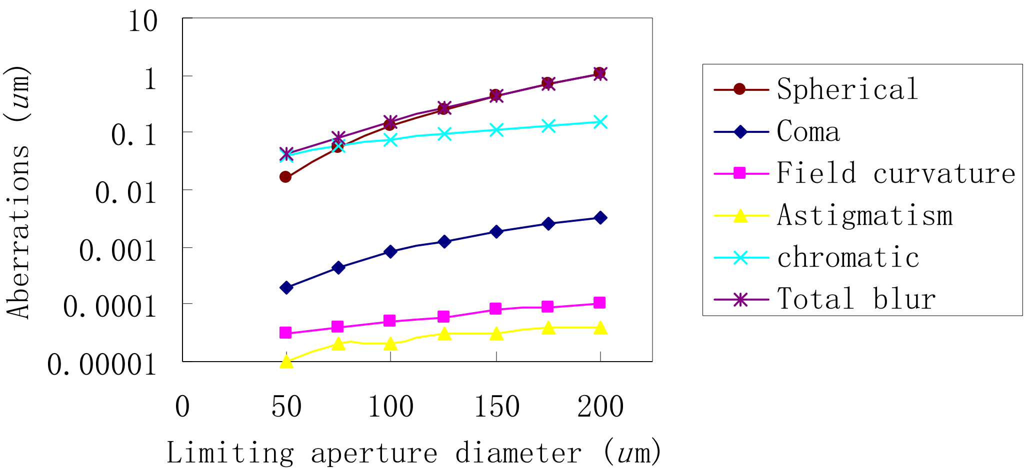

Figure 2.12: Aberrations vs. limiting aperture diameter for the 35kV accelerator column design.

2.2.2.3 The effect induced by the column housing

In the optics design simulation, boundary condition is one of the most important parameter which needs to be specified by users. Usually Direchlet boundary conditions will be applied for the starting plane and end plane, and Neumann boundary conditions will be used for all the boundaries in axial direction. This is usually true for an optics column with fixed voltages on the two ends and a set of electrodes in between to define a special potential distribution. Most of the time, the outside housing of the real system is far away from the electrostatic lens, and won't affect the potential distribution at the lens area. But for the 35 kV compact optics column design, a grounded outside housing with an inner diameter of 3 cm is assembled. The potential distribution with and without the outside housing are calculated and shown in figure 2.13. Very obviously, the potential distribution is totally different when a grounded outside housing is employed.

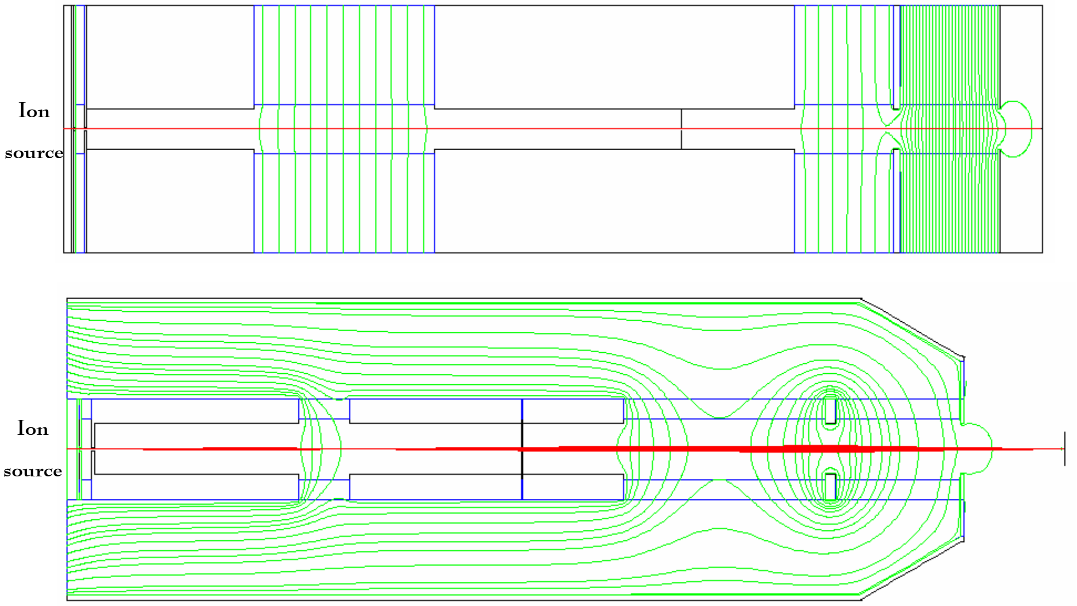

Figure 2.13: Potential distribution inside the five-electrode column. (top) without the outside housing; (bottom) a grounded outside housing is assembled.

2.2.2.4 Optical properties of the 35 kV accelerator column

A very compact optics column has been designed using the Munro simulation code. The maximum accelerating voltage is 35kV, the total length of the column is 88 mm, and the working distance is 10 mm. Based on the results of ion optics computation, beam spots of sub-micron size can be achieved at the target with beam energies from 5-35 keV if a 50-μm-diameter extraction aperture is used. Smaller beam spot sizes can be obtained with smaller apertures at the sacrifice of some beam current. Table 1 compares the beam spot size at the target for three different extraction aperture diameters. For a 5-μm-diameter aperture, a focused ion beam spot of approximately 100 nm in diameter can be achieved. Beam trajectories of the ions propagating through the 35kV column are calculated by ray tracing program from Munro code and are shown in figure 2.13.

Demagnification factor	**61**		
Extraction Aperture size (μm)	**50**	**10**	**5**
Image size (μm)	**0.8**	**0.2**	**0.1**
Blur (μm)	**0.2**	**0.05**	**0.03**

Table 2.1: Summary of the beam spot size of the FIB calculated using Munro’s code.

Mechanical design of the all-electrostatic five-electrode column is shown in figure 2.14. The five electrodes are separated with ceramic spacers. An outer housing is tapered down to the last grounded electrode. Three precisely machined ceramic rods are used to hold and center the electrodes. Photographs of the ion gun unit assembly are shown in figure 2.15. This ion gun will be installed into a working chamber together with a SEM tool. With this combination, one can perform surface processing and imaging in-situly.

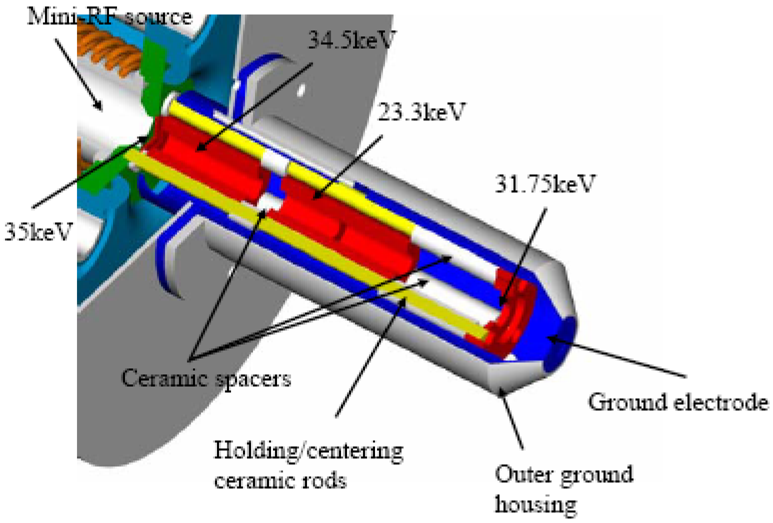

Figure 2.14: Mechanical design of the all-electrostatic system.


(a) (b)

(c)

Figure 2.15: Photograph of the ion gun unit. (a) all parts before assembling; (b) configuration of the electrodes assembly without outside housing; (c) whole view of the unit after assembling.

2.3 Scanning electron microscope (SEM) system for the dual beam system

An FEI two-lens (2LE) column, together with a channeltron for secondary electron detection, is employed for SEM imaging. Utilizing Schottky emission, electrostatic focusing optics, and stacked-disk column construction, it can provide high-resolution imaging capability. At typical imaging conditions (1nA probe current, 25 mm working distance, 25 keV beam energy), the 2LE can resolve features as small as 20 nm. Functions such as beam scanning, magnification, stigmation, blanking, and image rotation are all controlled by the deflection controller.

Figure 2.16 shows the set up of the FEI 2LE column for SEM imaging. It is mounted on the system chamber at an angle of 45^0. All the high voltage power supplies and pump controller are installed on the rack next to the worktable. Some preliminary results have been obtained after system integration and debugging. Figure 2.17 is the image of a dummy sample. More work is in progress to improve the image quality.

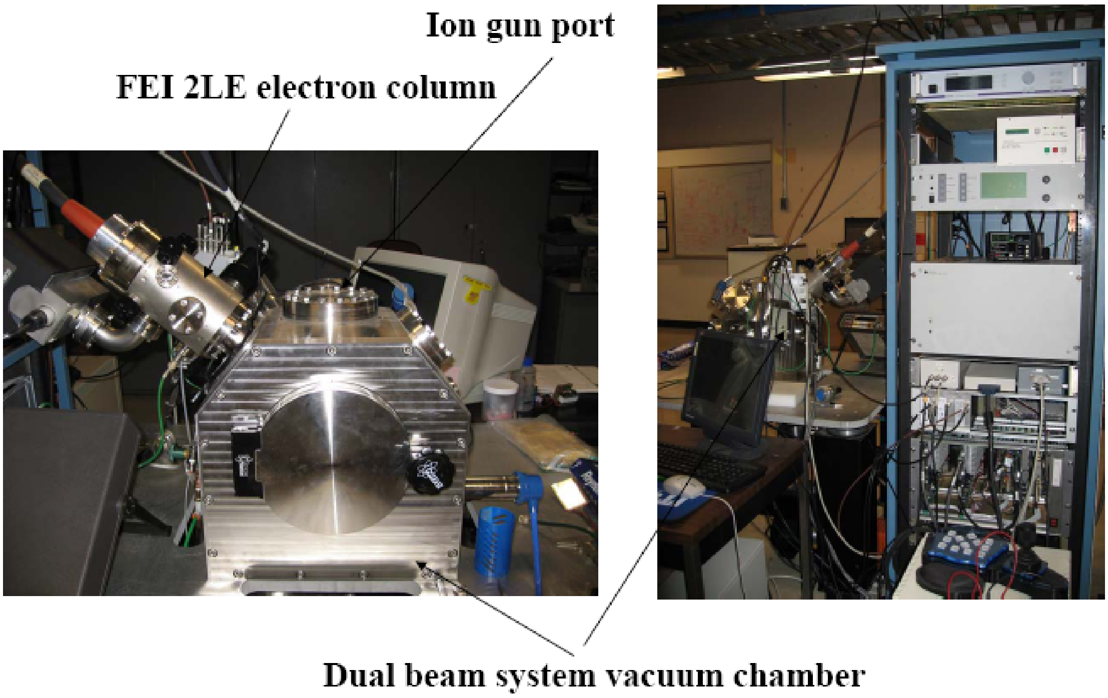

Figure 2.16: A FEI 2LE column has been set up for SEM imaging. It's aiming at the sample target with an angle of 45^0. (left) The cabinet with all the electronic control devices.(right)

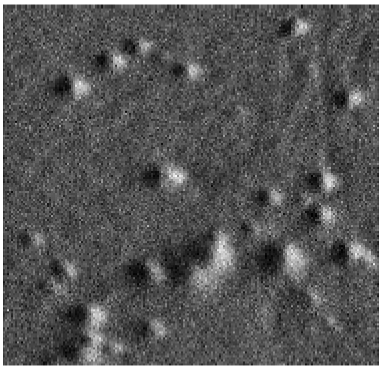

Figure 2.17: The first imaging obtained. More work is needed to improve the image quality.

2.4 System integration

Figure 2.18 illustrates the schematic design of the complete system. The ion source and the FIB column are mounted vertically, while the SEM column is aiming at an angle of 45°. A sample manipulator, constructed by Zyvex Corporation, has four degrees of freedom, including x, y, z movement and rotation. For normal operation, the sample is placed perpendicular to the FIB column. The sample stage can remain on the 0° axis so as to ensure the best reproducibility and minimal drift. The Zyvex stage sits on a tilt-stage, which allows the FIB to perform 3D machining when needed. A load-lock system is integrated on one side of the system chamber for sample loading and unloading.

The axis of other ports on the top and sides of the chamber are all aiming at the Eucentric point of the dual beam system. Additional probes or diagnostic tools can be added in the future.

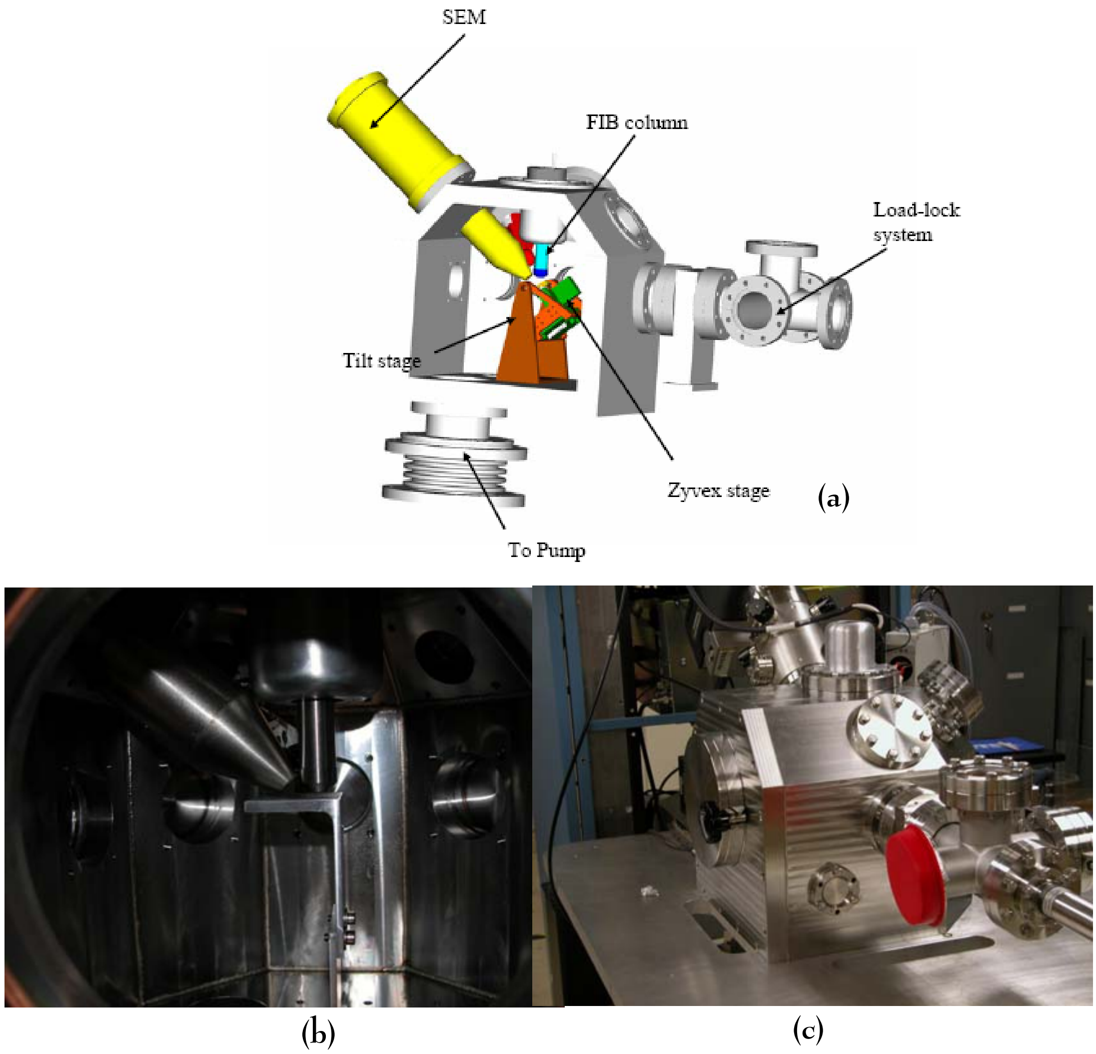

Figure 2.18: (a) Schematic diagram of the FIB/SEM dual beam system; (b) Photograph of the zoom-in view of the FIB/SEM integration inside the working chamber; (c) Photograph of the whole view of the system after integration.

2.5 Summary

A new multi-ion FIB/SEM dual beam system, which employs a plasma ion source instead of a liquid metal ion source in conventional FIB tools, provides selective implantation or machining with various ion species. Once developed, this technology will open up new opportunities in nanostructure fabrication and analysis. The mini-rf plasma ion source has been developed and tested. Ar^+ current densities as high as 100 mA/cm^2 have been extracted from the source with only 150 W of input rf power. Images have been obtained using the SEM. However, more work is needed to improve the image quality. The system is now in the final stage for integration, and a lot of electronic systems involved. After the integration, it will be delivered to Harvard University, installed and tested there.

Reference:

[1] J. Li, *et al.*, “Ion-beam sculpting at nanometer length scales”, *Nature*, Vol. 412, 166 (2001).

[2] S. Berger, *et al.*, “DualBeam metrology: A new technique for optimizing 0.13 μm photo processes”, *Proceeding of SPIE* Vol. 4344, 423 (2001).

[3] D. Sidawi, “Integrated FIB/SEM systems streamline throughput”, *R&D Magazine*, Nov. 33, (2003).

[4] X. Jiang, *et al.*, “Mini rf-driven ion sources for focused ion beam systems”, *Rev. Sci. Instrum.* 74, 2288 (2003).

[5] Q. Ji, *et al.*, “Production of various species of focused ion beam”, *Rev. Sci. Instrum.* 73, 822 (2002).

[6] T. Intrator and J. Menard, *Plasma Sources Sci. Technol.* 5, 371 (1996).

[7] R. B. Piejak, V. A. Godyak, and B. M. Alexandrovich, *Plasma Sources Sci. Technol.* 1, 179 (1992)

[8] N. A. Yatsenko, *Sov. Phys. Tech. Phys.* 26, 678 (1981)

[9] V. Kaeppelin, M. Carrere, and J. B. Faure, *Rev. Sci. Instrum.* 72, 4377 (2001)

[10] Q. Ji, *et al, J. Vac. Sci. Technol. B* 20, 2717 (2002).

[11] X. Jiang, Ph.D. dissertation, University of California, 2006.

[12] B. Lencova, “Electrostatic Lenses”, *Handbook of Charged Particle Optics*, edited by J. Orloff, 177 -222 (1997)

[13] P.W. Hawkers and E. Kasper, "Principle of electron optics: Basic Geometrical Optics". (1989).

[14] H.C. Chu and Eric Munro, "Numerical analysis of electron beam lithography systems. Part III: Calculation of the optical properties of electron focusing systems and dual-channel deflection systems with combined magnetic and electrostatic fields", Optik 61 (2), 121 (1981); Eric Munro, "Numerical modeling of electron and ion optics on personal computers", *J. Vac. Sci. Technol. A* 8 (6), 1657 (1990).

[15] Eric Munro, “Handbook of charged particle optics”, edited by Jon Orloff Vol 1, (1997),

[16] Eric Munro, Xieqing Zhu, John Rouse et al.,"Aberration analysis of wide-angle deflectors and lenses by direct ray-tracing, and comparison with conventional aberration theories" presented at *the Preceedings of SPIE Conference on Charged Particle Optics*, San Diego, California, SPIE, 2522, (1995).

[17] Q. Ji, Ph.D. dissertation, University of California, 2003.

Chapter 3:

A combined electron and focused ion beam system and its application

As discussed in the previous chapter, by replacing the liquid metal ion source (LMIS) with an ion source which is capable of forming ion beam of various ion species in the dual beam system, it has greatly enlarged the application area of ion beam.

3.1 Sample surface charging issue for focused ion beam application

Focused Ion Beam (FIB) systems have found important applications in micro-machining, mask repair, circuit inspection and ion doping for semiconductor fabrication. But for many of the ion beam applications involving either incoming or outgoing charged particles, sample surface charging of insulating materials can be a problem. These processes usually involve bombardment with primary positive ions, which gives rise to the emission of secondary ions and neutrals and large numbers of secondary electrons. The predominant species will usually be electrons and neutrals, thus with incoming positive ions insulating surfaces usually charge positively. The positive potential will build up gradually as the primary positive ions keep hitting on the sample surface. Ion optics will then be changed with the increasing potential. It broadens the incident focused beam and even deflects it out of the processing area. In applications such as secondary ion mass spectroscopy (SIMS), sample charging can deflect the primary beam from the analytical area, which often eliminates the secondary ion signal entirely. The charging effect also changes the energy distribution of the secondary ions, which affects their transmission and detection by the mass spectrometer. In the case of negative secondary ions detection, a positive surface potential will inhibit or totally suppress their emission. The rate of potential rise depends on the energy of the incoming primary ion beam. The limit will be determined by the capacitance of the material.[1]

Conventionally, there are two techniques to reduce target sample charging. An external electron beam can be aimed at the ion beam spot, and low energy electrons are flooded onto the processing area to compensate the positive potential. Alternatively, adding a gas cell on the path of the positively charged particles can partially neutralize the beam before it reaches the sample surface.

Either way is very complicated. To form electron beams, an electron source and column is needed. In addition, precise alignment of the ion and electron beam is inevitable. When multiple beamlets are required for some certain applications, it’s almost impossible to achieve neutralization using only one extra electron gun. The gas cell solution can reduce the sample charging effect to a certain extent, but cannot eliminate it entirely. Besides, it requires long working distance, depending on the cross-section of neutralization for different ion species.

In this chapter, a new system developed is discussed. It uses a double-chamber plasma source and a single acceleration column to form a beam containing both high-energy ions (designed to work at a few keV depending on the application) and low energy electrons (0 - 100eV) simultaneously. With the self-aligned low energy electrons, surface charging issue can easily be eliminated. The system can be applied to various ion beam tools, such as ion beam inspection systems, ion beam milling systems, and secondary ion mass spectroscopy[2].

3.2 System configuration and work principle

Different from the dual beam system described in chapter 2, the ion beam and the electron beam travel in the same direction and transport in one beam column. The working principle of the combined electron and focused ion beam system is illustrated in figure 3.1. As a source to generate both ion beam and electron beam simultaneously, it consists of two plasma chambers: one is used to generate ion beam (the one on the right) and the other one (the left one) is for electron beam generation. Both chambers, as shown in figure 3.1a, are RF-driven plasma sources with external antennas.

The electrons generated in the left chamber are extracted by a stack of electrodes which are installed in between the two plasma chambers. The stack of electrodes between the electron and ion source chambers serves two purposes: to extract and accelerate electrons from the electron source chamber and to prevent positive ions in the ion source chamber from streaming back into the electron source chamber. To achieve these purposes, the voltages applied on those electrodes are arranged in the way shown in figure 3.1b: Electrode 2 acts as an ion suppressor and is biased at a little higher positive potential than Electrode 3 (50V higher in the experiment), so that positive ions in the right chamber (ion chamber) are confined in their own chamber by this potential barrier. The potential on Electrode 1 is the most negative. Therefore, the electrons leaked from the ion source chamber can’t reach the left side either. The RF plasma source employs external antenna, thus it is empty inside the source chamber. Electrons extracted from the left chamber will pass through the ion source chamber without any obstacle. Since the electron beam energy is higher than the positive ion extraction voltage, the high-energy electrons and the positive ions with thermal energy are extracted from the right chamber into the column together. Thus, a beam consisting of both electrons and positive ions is formed. At the right end of the ion source, a molybdenum electrode is assembled as the plasma electrode and the beam transportation column is installed next to it. In the preliminary testing, a single gap extraction is employed. Later on a column consisting of a complete electrostatic lens system will replace the single gap extraction for beam focusing and acceleration purpose.

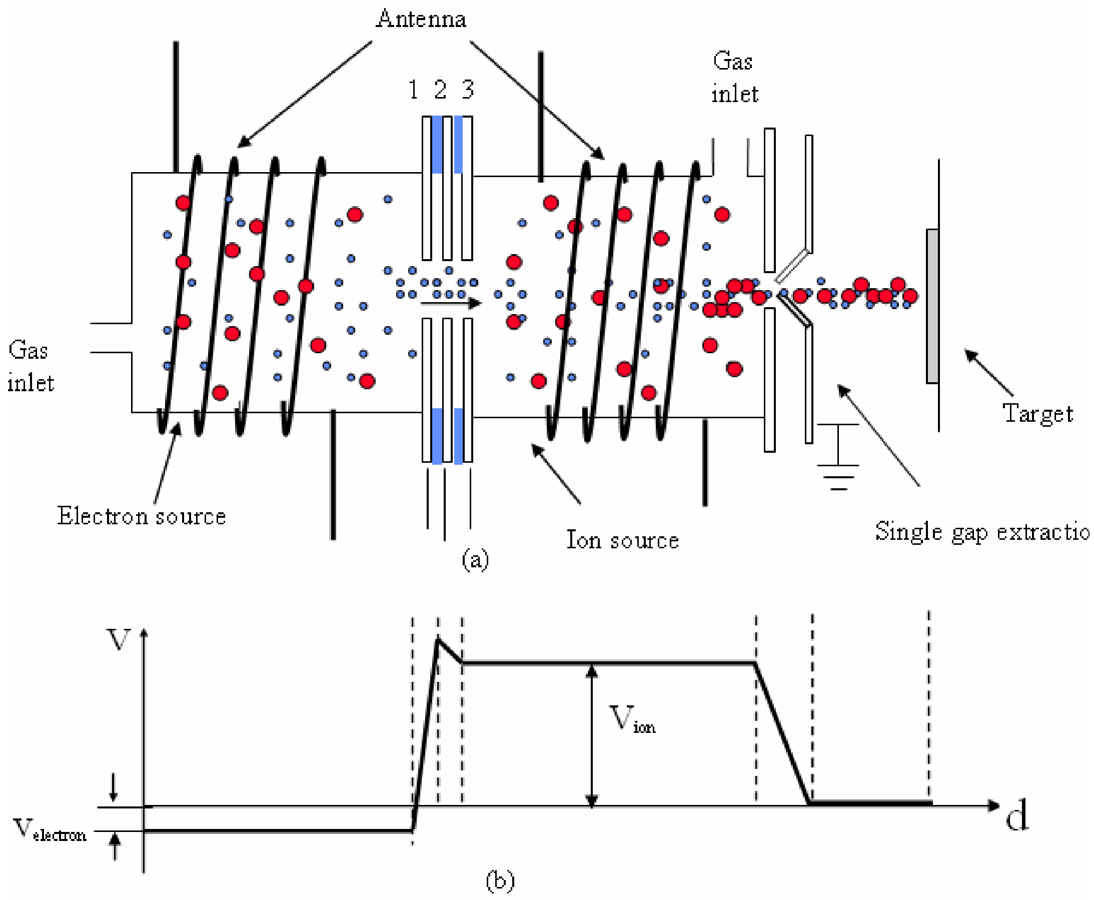

Figure 3.1: (a) Schematic diagram of a double-chamber source. A beam consisting of electrons and positive ions can be formed using a single column. Larger dots represent positive ions, while smaller dots represent electrons. (b) Axial potential distribution of the setup.

In the prototype device, the electron source and the ion source are made of two identical ceramic chambers. Each chamber has its own port for gas inlet; gas-line connecting from the needle valve is split into two by a “T” shape ultra-torr adapter and then connects to the gas inlets for each chambers. A quartz window is installed at the left end of the electron source so that the discharge plasma is visible externally. The inner diameter is 1.5 cm and the length of each source is 3 cm. Still, double layer antenna coils in parallel are employed.

The double-chamber plasma source can be operated using either one set of RF generator and matching network or two sets. If one set of RF generator and matching network is employed, the two plasma chambers will be controlled simultaneously. In this case, the antenna of the two chambers can be wrapped in series or in parallel. Using only one set of RF generator and matching network makes the whole system more compact, but with this setup, igniting the plasma in the double-chamber source is tricky. To generate plasma in both chambers, the number of the turns and geometry of the antenna coil and the gas pressure for each chamber have to be exactly the same. In another word, the two source chambers have to be operated under exactly the same condition. Otherwise, plasma will be ignited in one chamber first, then the impedance of the whole system changes. This again will cause most of the RF power coupled into the chamber which has already been ignited, which makes it even harder to ignite plasma in the other source chamber.

Independent control of each source chamber can be achieved by using separate RF generator and matching network. Then the electron source and the ion source can be turned on and off separately, without affecting the other source's operation. Also each source chamber can be running at different gas pressure and RF power thus at different plasma density.

Air cooling is required during the source operation. Photographs of the double chamber source in operation with both sources on (a), ion source on electron source off (b), and ion source off electron source on (c) are shown in figure 3.2

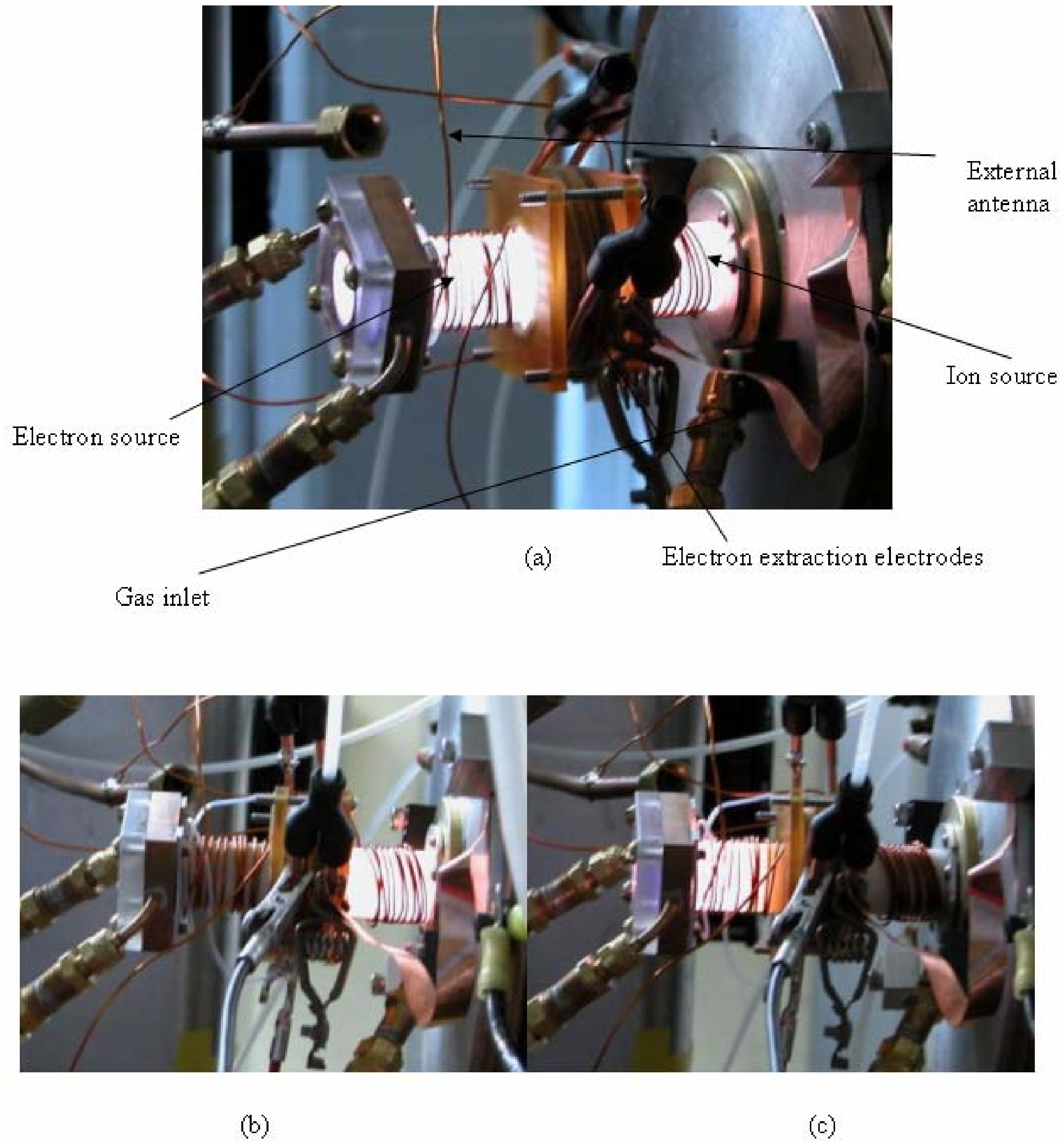

Figure 3.2: Picture of the double-chamber source operation, electron source and ion source can be switched on and off separately: (a) both the electron source and ion source are ignited; (b) only the ion source is ignited; and (c) only the electron source is ignited.

3.3 Combined electron and ion beam generation

3.3.1. Plasma ignition

Each plasma chamber for the double-chamber-source is similar to the mini RF source discussed in chapter 2, but a little shorter in length. As mentioned in the previous chapter, to ignite plasma in such a small size chamber, high gas pressure is required. For plasma ignition, 100 mTorr gas pressure is introduced in both chambers first, and RF power for each chamber is increased. Usually high density inductively-coupled plasma appears when the RF power is over 60W. After the ignition, the gas pressure can be tuned down to 20 mTorr to maintain the plasma. The RF power for each chamber can also be reduced to get a desired plasma density.

3.3.2. Beam current measurement

In the experiment, each chamber is controlled separately. The RF input power on the electron chamber is 30 watts and that on the ion chamber is 50 watts. A permanent-magnet mass separator (figure 3.3) is installed next to the extraction electrode. When the combined electron and ion beam come out from the double-chamber-source and enters the mass separator, where a magnetic field of 100 Gauss in the center is formed by a pair of permanent magnet. The magnetic force will bend the electrons onto the sidewall of the mass separator where they are collected and the current is measured while the accelerated ions will travel almost un-deflected and are collected in another Faraday cup.

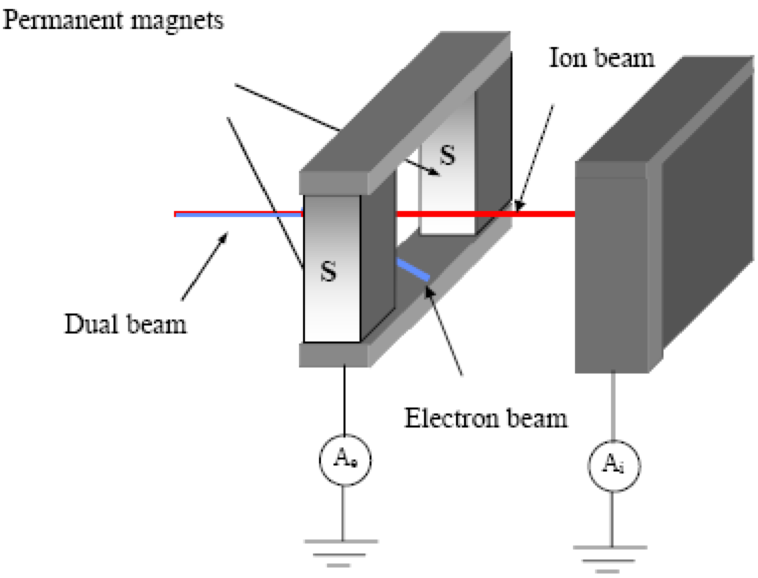

Figure 3.3: Schematic diagram of the beam separator used for dual beam detection.

As shown in Table 1, the ion or electron current is measured under three different conditions. When only the electron source is switched on, with an electron extraction voltage of 600V, an electron current of 260 nA is measured. When the ion source is also switched on and a 200V ion extraction voltage is applied, besides the 260 nA electron current, an ion beam current of 1520 nA is collected on the ion beam collector. With the electron source off, the ion current decreases to 567nA.

$V_{electron}$ (V)	V_{ion} (V)	Beam current (nA)	
		Electron	Ion
600	0	260	0
0	200	0	567
600	200	260	1520

Table 1: Electron and ion beam current detected by the beam separator.

This current measurement was taken under special conditions: the extraction voltage of the ion beam is very low (200V only); the electron source was operating at a very low plasma density; and the extraction voltage for the electron beam is much higher than that of the ion beam. With a measurement condition like this, several conclusions can be made from the results. The current measurement results confirm the co-existence of both electrons and ions in the beam. It also shows that the presence of electron beam can increase the ion beam current by reducing the space charge effect.

When the plasma density is high and the electric field at the extraction aperture is weak, the plasma meniscus protrudes out, and the extracted ion beam will have a large angular divergence. Some ion current will be intercepted by the second electrode.[3] The presence of the electron beam can reduce the angular divergence of the plasma meniscus and shrink the ion beam size, thus increase the ion beam current. Of course one cannot expect that the ion current will always increase by a big amount as in this case. This is only a case of a low extraction electric field. The curvature of the plasma meniscus will decrease when extraction electric field becomes higher. Thus the increase in ion current will also become smaller.

Even with the condition of low plasma density in the electron source and an 800V electron extraction voltage ($V_{electron} + V_{ion}$), most electrons are lost on the electrodes and the ion source chamber wall. Thus only a very tiny portion of the electron beam can contribute to the combined beam. In the current measurement experiment, 40μA of electron current can be extracted from the electron source chamber and only 20μA of it reaches Electrode 3. After a long propagation in the ion source, 2μA electron current is collected on the plasma electrode and 260nA can go through the extraction hole and finally be measured on the electron collection Faraday cup. The large quantity of electrons lost on the electrodes and the ion source chamber causes severe sputtering and secondary electrons emission, which induces damage on the electrodes. The main reason that causes the electrons to keep being lost during the transportation is the poor electron optics of the three-electrodes electron acceleration column design. An electron delivery column thus was designed to replace the existing electrodes. It will accelerate the electrons to an initially higher energy than any of the subsequent ion accelerating voltages in the lens column and at the same time forming a parallel beam. According to the simulation results shown in figure 3.4, over 80% electrons can pass the ion source with the new electron delivery column, which means a much higher electron current is achievable.

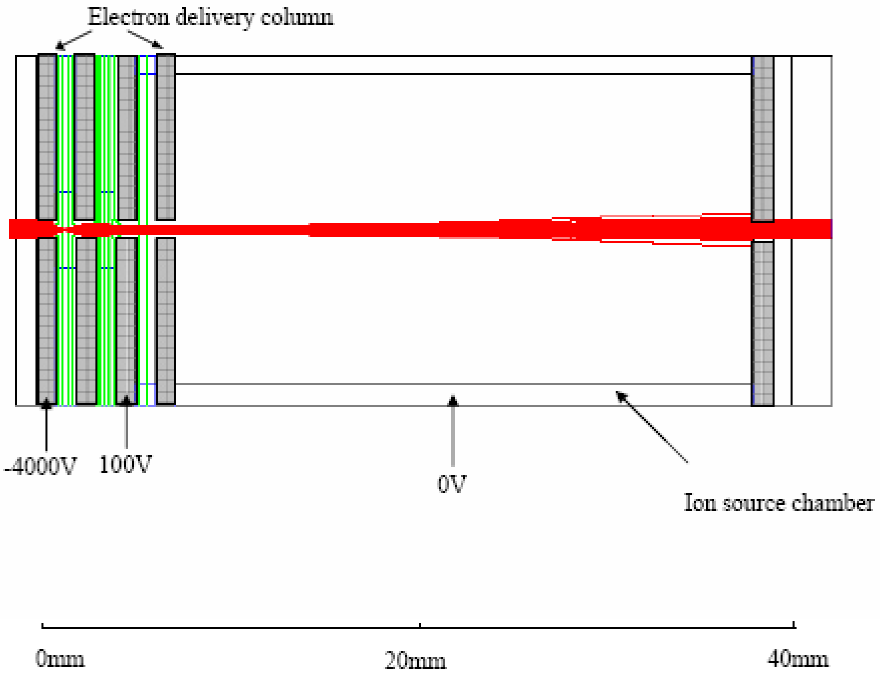

Figure 3.4: Ray tracing result of electron beam extracted from the electron source chamber passing through an electron delivery column and the ion source chamber. The simulation is performed using the MUNRO code.

3.3.3 Surface neutralization effect

Experiments have been conducted to demonstrate the surface neutralization effect. A piece of silicon wafer coated with a thin film of silicon nitride film is irradiated with the combined electron (with energy of 100eV) and ion (with energy of 1.5keV) beams for 20mins. For comparison, the electron source is turned off and a separate target is exposed to the ion beam extracted with the same energy and for the same time duration. The exposure results are shown in figure 3.5a. The beam spot size of the sample sputtered with dual electron and ion beams is approximately 60% of the one with ions alone. This shrinkage is mainly due to two reasons: with the presence of electrons, the insulator is better neutralized; and at the same time, the ion beam angular divergence is reduced which shrinks the ion beam spot size. For comparison, another experiment has been performed to investigate the effect of the second factor alone. Under the setup described above, stainless steel sheet is used as the substrate instead of silicon wafer. Since stainless-steel is a good electrical conductor, surface charging will not occur. Any observed difference between the two exposure results will only due to the reduced space charge effect. Figure 3.5 b shows the exposure results with dual ion/electron beam (left) and with ion beam only (right). The reduced space charge effect shrinks the beam size to almost 80% of the original size.

Combined with the former results, again this confirms the presence of surface neutralization effect.

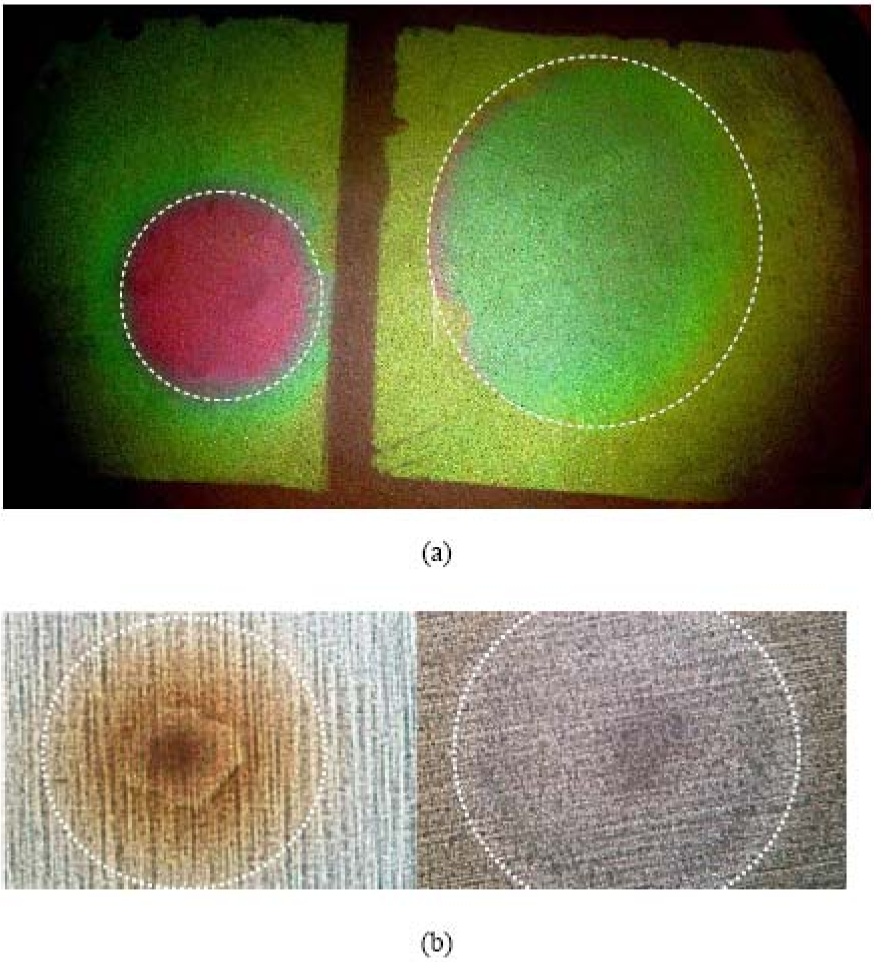

(a)

(b)

Figure 3.5: Photographs of two Ar^+ ion irradiated (a) silicon nitride films with electrons (left) and without electrons (right); (b) stainless steel sheets with electrons (left) and without electrons (right).

3.3.4 Multiple-beamlet generation

This approach for surface neutralization also has another advantage: one can easily extend a single beamlet formation to multi-beamlet generation. Figure 3.6 shows the schematic drawing of a modified system for multi-electron-ion beamlet formation. In this configuration, the electron beams produced in the electron source chamber take the shape of ribbons, which overlap columns of circular positive ion beamlets that are generated in the ion source chamber. All electrons will cover the area from where ions are extracted, which eliminates the complicated alignment procedure. This kind of large-area multi-beam neutralization is difficult to accomplish by using the conventional external electron beam compensation method. In addition, the capability of multiple beamlets generation will greatly increase the large area sample analysis efficiency for ion spectrometry tools.

Some test results on the multiple beamlets exposure are shown in figure 3.7. Four beamlets are generated at the same time and hitting on a piece of N-type heavily-doped silicon wafer for 10 min. Four dents are formed on the target and the depth profiles of the dents are measured using KLA-Tencor ASIQ step profiler. With same exposure time, the dents drilled by the combined electron and ion beam are 50% deeper than those drilled without electron beam. The beam spot size shrunk a little (2.5%) with the presence of the electron beam. The possible reasons may cause this difference: one is the electrons in the beam have reduced the space charge effect, which leads to an increase of the primary ion current density; in the same time, the total extracted ion current has also increased with the presence of electrons. A model needs to be developed to study this effect.

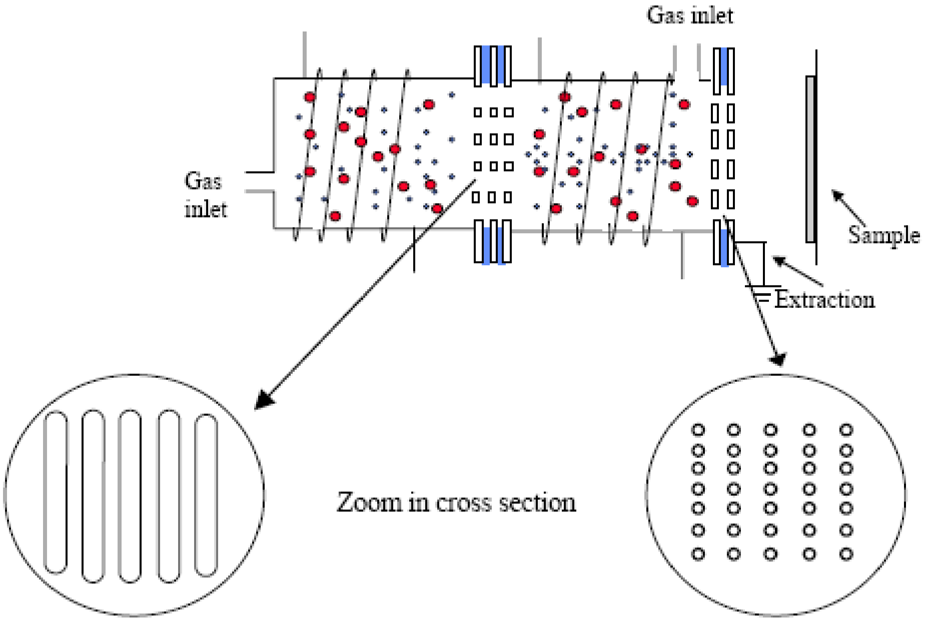

Figure 3.6: Schematic diagram of a double-chamber source with multiple beamlets. Beams consisting of electrons and positive ions can be formed using a single column. Larger dots represent positive ions, while smaller dots represent electrons.

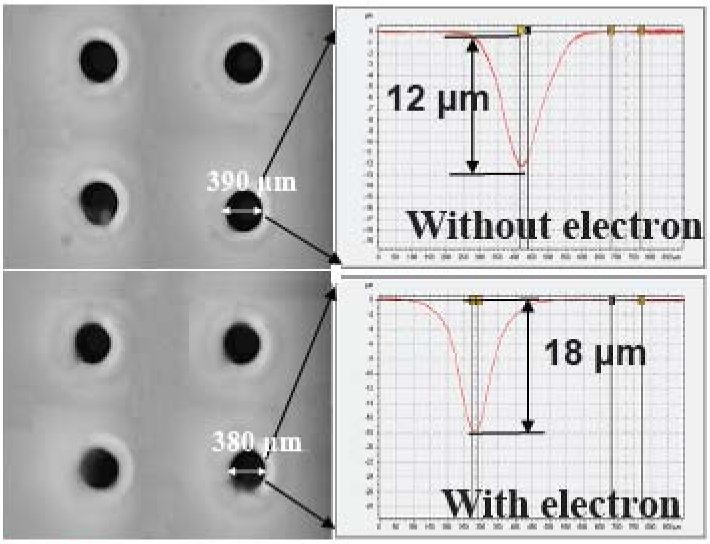

Figure 3.7: Photographs of the multiple dents milled by positive ion beam (upper left) and combined electron and ion beam (lower left), and depth profile measured by a KLA-Tencor ASIQ step profiler (right).

3.4 Applications: the combined electron and focused ion beam system can improve the secondary ion yield in SIMS system by electron post-ionization

3.4.1 What is SIMS

SIMS is the mass spectrometry of ionized particles which are emitted when a surface, usually a solid, though sometimes a liquid, is bombarded by energetic primary particles. The primary particles may be electrons, ions, neutrals, or photons. The emitted (so-called "secondary") particles will be electrons; neutral species, atoms, and molecules; atomic and cluster ions. It is the secondary ions that are detected and analyzed by a mass spectrometer. It provides a mass spectrum of a surface and enables a detailed chemical analysis of a surface or solid to be performed. In a development of SIMS, those particles initially emitted as neutrals may be post-ionized and contribute to the analysis.

Figure 3.8 schematically outlines the mechanism of SIMS. In the case of ion or atom bombardment, the energy of the primary beam is transferred to the atoms in the solid by a billiard-ball-type collision process. A cascade of collisions occurs between the atoms in the solid; some collisions return to the surface and result in the emission of atoms and atom clusters, some of which are ionized in the course of leaving the surface and can be analyzed with a mass spectrometer.

The basic arrangement for the SIMS experiment is shown in figure 3.9. The primary particle source is capable of producing a beam of ions or atoms in the 0.5-50 keV energy range. The emitted secondary ions are collected by an ion transport optics and directed into a mass spectrometer which may be of the magnetic sector, quadrupole, or time-of-flight type.

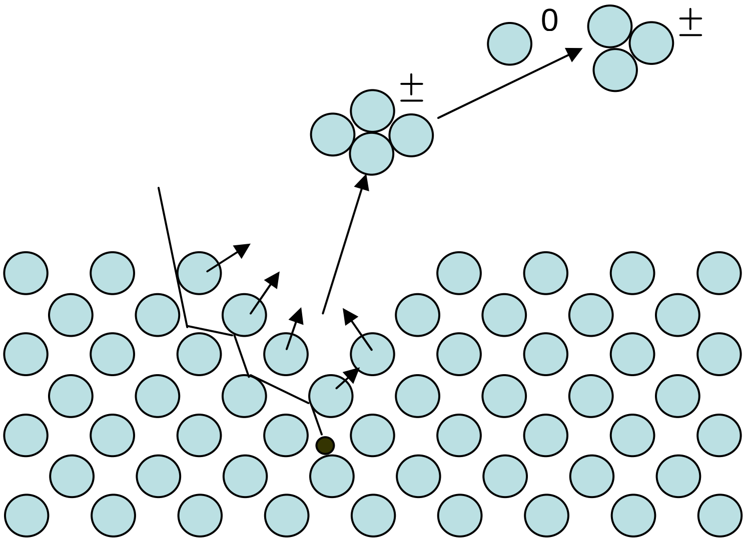

Figure 3.8: Diagram of the SIMS principle indicating the collision of the primary particles with a solid surface and the emission of secondary particles.

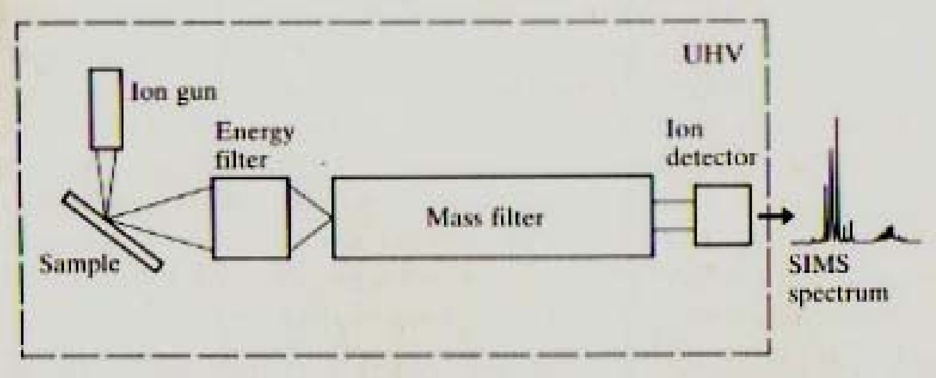

Figure 3.9: Schematic diagram of the main components of the SIMS instrument.

3.4.2 Matrix effect

In the research area of secondary ion mass spectrometry, as the demands for surface analyses combining high sensitivity and quantification are increasing, the conventional SIMS method is facing several limitations[4,5]. Perhaps the most severe is the significant limitation of ion yield that results from matrix effects, which is the (often unknown) relationship between the chemical composition of a solid, and the secondary ion yield. A matrix element concentration is more difficult to determine than a minor element concentration because of the matrix effect. Matrix effect is due to the fact that ionization rates of atoms are highly dependant on their chemical environment within the analyzed material. As a consequence, when one measures the signal of an ion made up of one matrix atom, this signal is generally not proportional to the element concentration[1].

3.4.3 Some post-ionization techniques and issues

In order to increase the efficiency of SIMS tools, various post-ionization techniques have been developed. In these techniques, an electron beam, plasma or a laser beam is generated and passes through an ionization zone, where the secondary neutrals are ionized[6-8]. By decoupling the ionization step and the desorption step, the secondary neutrals can be detected. Since the chemical matrix effect has much less influence on the emission of neutrals than ions, the limitation from the matrix effect can be greatly reduced [2].

Up to the present, electron bombardment post-ionization, electron plasma post-ionization and laser induced post-ionization are the most frequently used post-ionization techniques[1].

3.4.3.1 Electron bombardment post-ionization

Simple electron bombardment method was introduced many years ago. It is compatible with UHV and involves a relatively simple modification to a SIMS system. An electron beam ionizer is incorporated in the secondary ion optics. This can be similar in form to the type of ion source used for residual gas analysis, and is basically a beam of electrons emitted from a hot filament, accelerated to 30-100eV across the path of the secondary neutrals. Ionization occurs within the electron cloud by electron bombardment phenomenon.

The region of ion production is small meaning that relatively fewer neutrals are sputtered in the correct direction and drift into this region. Additionally, the probability of ionization is rather low, so that for most elements the sensitivity is significantly low. Some improvement can be obtained using magnetic confinement of the electrons. The ionization yield, however, is always low, about 10^{-4} -10^{-3}. The schematic of the electron bombardment ionizer combined with a parallel-plate energy analyzer is shown in figure 3.10[1].

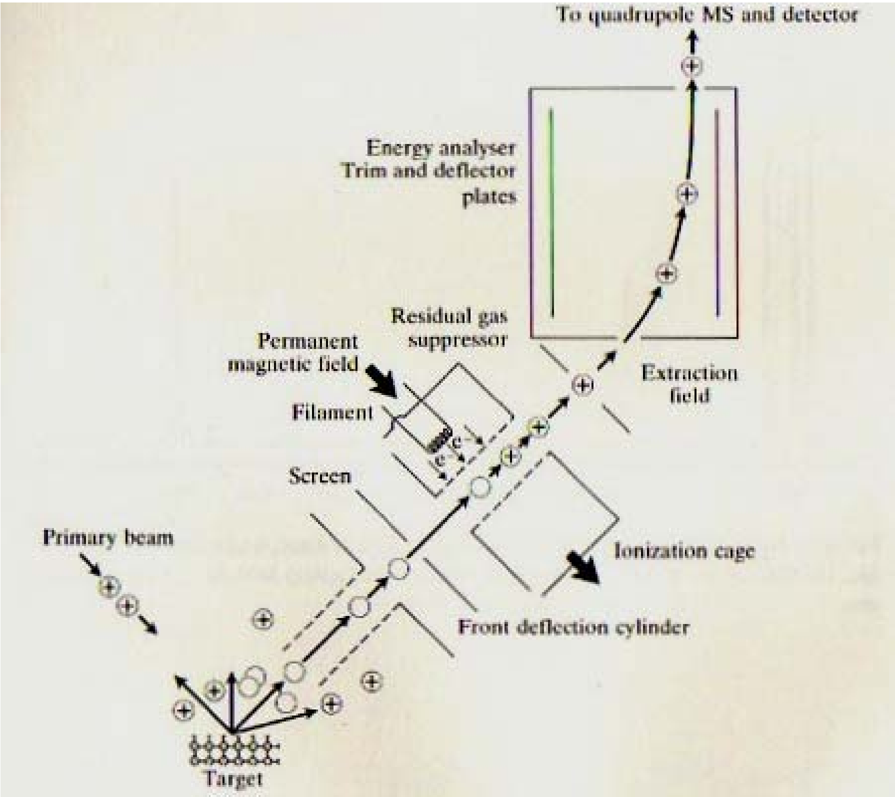

Figure 3.10: Schematic diagram of an electron bombardment ionizer together with a parallel-plate energy analyzer.[1]

3.4.3.2 Electron plasma post-ionization

The low ionization probability can be improved by a factor of about 100 by increasing the electron density. Oechsner et al.[9] have used a low pressure (10^{-4} mbar) argon plasma, or hot electron gas, to increase the electron density and hence to increase ionization efficiency to about 10^{-2}. The great advantage of this method is that the space charge of electrons is compensated by the background of positive ions. High electron densities (10^{10} cm^{-3}) are thus generated. The post-ionization factor depends on the plasma parameters, the density of electrons; the electron impact ionization function; and the path length of the ion through the ionizer. A schematic diagram of a commercial version of this instrument is shown in figure 3.11[1].

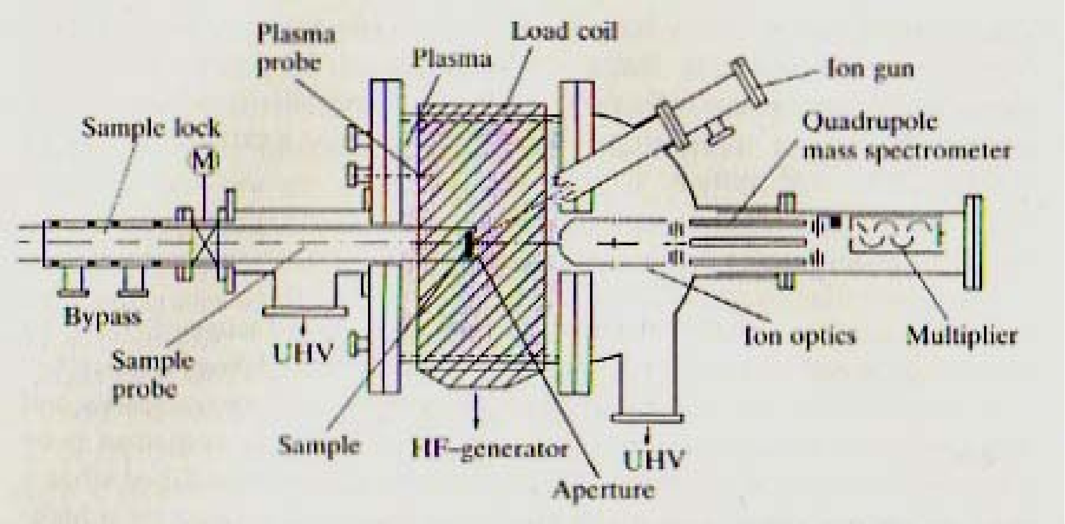

Figure 3.11: Schematic diagram of a commercial combined SNMS-SIMS instrument.[1]

3.4.3.3 Laser-induced post-ionization

The most elegant method of post-ionization is to use a pulsed high-energy laser to ionize the neutrals as they leave the surface. This means that the SIMS system must use a TOFMS. Ionization requires that the energy of the highest energy electron be elevated to the vacuum level. This may be accomplished by a progressive “climb” up the energy levels, by carefully tuning the laser energy to the energy differences between the energy levels. Sometimes only one photon will be required. Unfortunately, for some of the most interesting elements, several photons of different energy will be required to achieve ionization (Si and Sb four photons; P, As and Se, five photons), which necessitates an array of several different lasers tuned to specified frequencies. This is known as multi-photon resonance ionization (MPRI). Clearly, as all the elements have unique energy level arrangements, the process will be element specific.

The laser beam is directed parallel to and a few mm above the sample surface, and is pulsed $\leq 10^{-6}$ s after the moment of secondary ion emission. The pulsed nature of the operation required a TOFMS and in practice the primary beam source is also pulsed to minimize sample consumption. Pulse timing is crucial. The schematic of a laser-induced post-ionization apparatus is shown in figure 3.12[1].

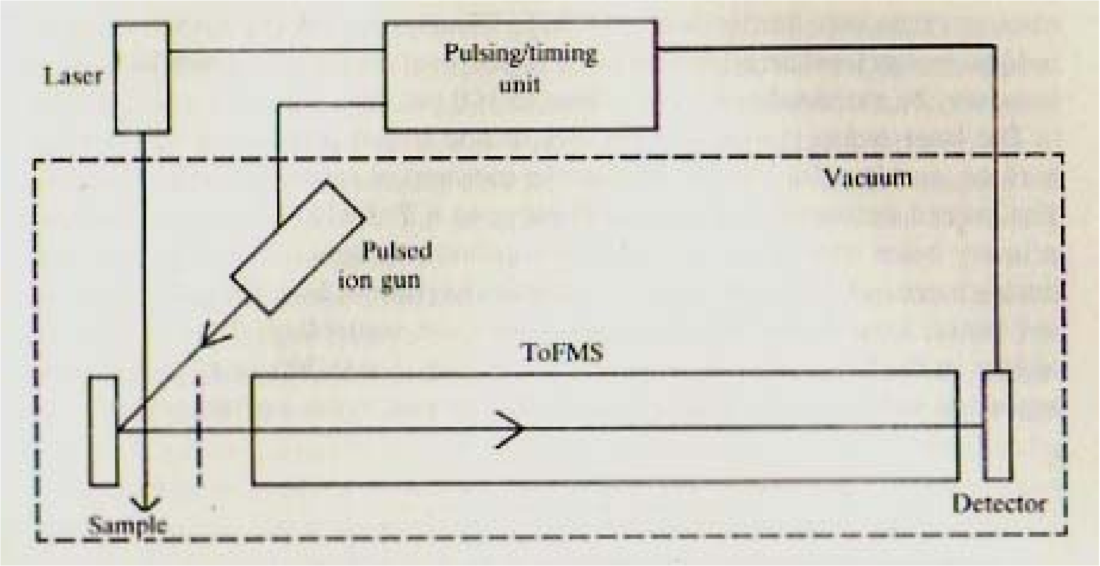

Figure 3.12: Schematic diagram of a laser-induced post-ionization apparatus.[1]

3.4.4 Surface charging problem for SIMS

Another problem for SIMS is the analysis of insulating materials such as biomaterials, glass, ceramics and plastics. Many industries, such as those involving biotechnology, polymers, and flat panel displays, rely heavily on these materials[10]. These insulating samples often undergo charge buildup on their surface during analysis, which greatly limits the detection efficiency. Unintentional changes in the sample potential during the course of the depth profile will modify the secondary ion extraction field, produce a change in instrumental transmission and lead to a profile distortion. It also diffuses the primary beam and diverts it from the analytical area, often eliminating the secondary ion signal entirely.

Charge compensation can be achieved by use of simultaneous electron beam "flooding" of the sample. In many SIMS instruments, a separate electron gun is employed and floods the analytical area with electrons[8]. Relatively high (couple hundred eV) electron energy, though less effective, is widely used. However, since high energy electrons produce more than one secondary electron from the sample, low energy electrons work much better[11]. Charge compensation can also be achieved by providing a conduction path, e.g. by gold coating; or by continuously monitoring for any change in the sample potential and applying a DC potential to the sample holder to correct for it.

3.4.5 Significantly increasing post-ionization efficiency by employing the combined electron and focused ion beam system

Being able to generate low energy electrons and high energy positive ions simultaneously in one beam, the combined electron and positive ion beam system may become an ideal candidate for SIMS to replace the single primary ion beam. With only the single primary ion beam hitting the sample, secondary ions and neutrals are both sputtered off, but typically more than 95% of the sputtered atoms are neutrals. When an electron beam is co-propagating with the ion beam, the low energy electrons induce electron impact ionization of the neutrals. At a certain optimized electron energy, the ionization rate can be significantly increased, thus greatly increasing the secondary ion yield and improving the secondary ion signal. At the same time, the low energy electrons also compensates for the positive potential induced by the localized surface charging for insulating target materials. In addition, a complicated alignment procedure is no longer needed for this setup; and much simple and compact system configuration can be achieved. Experimental investigation has been carried out.

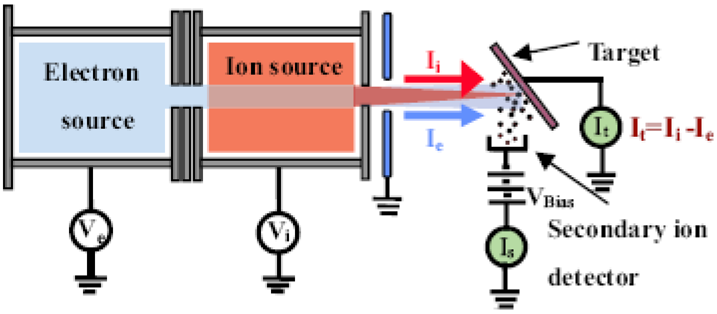

Figure 3.13: Schematic of the experiment setup. Self-aligned low energy electron and high energy ion beam are generated by the double-chamber source and hitting on the target at an incident angle of 45°. Current on the target I_t and current on the secondary ion detector I_s are monitored.

The experimental setup is shown in figure 3.13. On the left, the electron beam is extracted and accelerated by the series of electrodes. The high energy electrons pass through the ion source and come out with the positive ions into the electrostatic column, which simultaneously accelerates the positive ions and decelerates the electron beam. Finally self-aligned high energy ions and low energy electrons reach the sample surface together at an incident angle of 45 degrees. During the primary ion beam bombardment on the sample surface, secondary particles emit from the exposure area, most of which are secondary neutrals. At the same time, the low energy electrons in the combined beam then will collide with the sputtered neutrals, inducing post-ionization process. Hence, the secondary ion current can be increased.

3.4.5.1 Experimental results on conducting target

A conducting material- aluminum is used as the target for first demonstration. The total current on the target I_t is monitored. The target current I_t consists of four components: the primary ion current I_i, the primary electron current I_e, the secondary ion current I_{si} and the secondary electron current I_{se}. It can be described as:

$$I_t = I_i + I_{se} - I_e - I_{si} \tag{3-1}$$

Where I_i I_e I_{si} I_{se} are scalar values and the "+" and "-" are indicating the direction of the current. I_{si} and I_{se} are induced by both the primary electron beam and the primary ion beam. Since the primary ion energy is set below 1.5 keV and the primary electron energy is less than 100 eV, secondary electron yield is small compared with the primary beam current. Also secondary ion yield direct from the primary ion and electron bombardment is very small (most of the sputtered secondary atoms are neutrals). Both I_{si} and I_{se} can be neglected for the first order estimation. Thus equation 3-2 can be modified as:

$$I_t = I_i - I_e \tag{3-2}$$

The electron current I_e can be measured separately by turning the ion source off and measuring the remaining current on the target, again, the secondary electron current induced by the primary electron is neglected. Thus the primary ion current I_i can be calculated by adding I_t and I_e together.

A secondary ion detector is installed near the secondary ion emission area as indicated in figure 3.12, part of the secondary ions are collected on the detector and the secondary ion current I_s is measured. In the experiment, the energy of the primary ions, which is indicated by the ion source biasing voltage V_i, is fixed at 1.1 keV and the electron source biasing voltage V_e is adjustable from -100 eV to 100 eV. When V_e is positive, the electron source is biased positive to the grounded target, the electron beam will not have enough energy to reach the sample surface; when V_e is negative, the electron beam then will reach the target with an energy of eV_e; thus the electron energy at the target can be tuned by adjusting the electron source biasing voltage V_e to optimize the post-ionization rate.

Since I_s is only part of the total secondary ion current, the ratio I_s/I_i can be define as the "partial" secondary ion yield, which is proportional to the secondary ion yield. It is plotted as the function of electron source biasing voltage V_e. As shown in figure 3.14, when the electron source is biased positive, electrons don't have enough energy to reach the grounded sample target. Only primary ion sputtering occurs in positive V_e range, so the value of I_s/I_i is the secondary ion yield without electron beam post-ionization. As the electron source biasing voltage becomes negative, electrons start to flood the target. The electron impact ionization begins to take effect even at a small electron energy. At a certain electron energy, the total ionization rate reaches the maximum value which results in a peak of the secondary ion yield. As shown on the plot the secondary ion yield increases with the energy of the electron beams and peaks at around 50 eV.

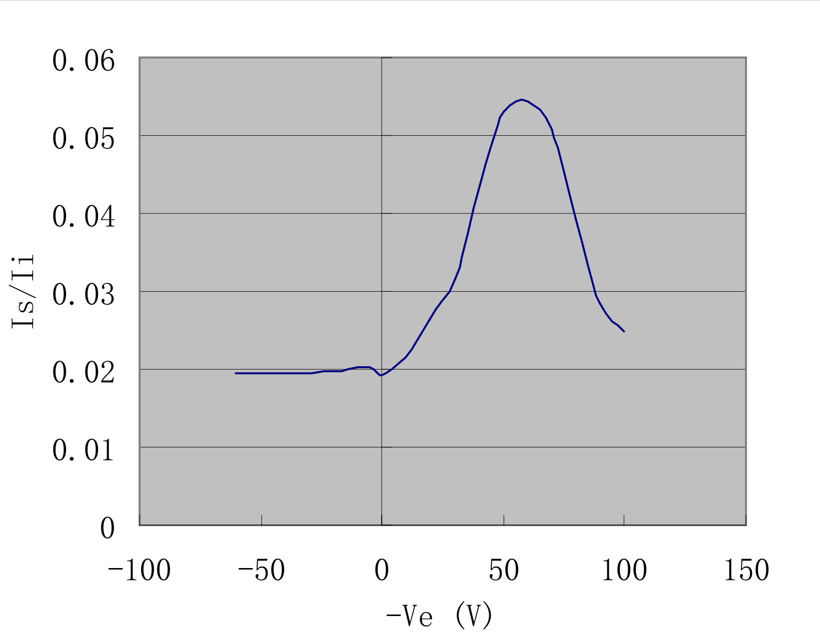

Figure 3.14: I_s/I_t which is proportional to the secondary ion yield is plotted as a function of electron source biasing voltage V_e. When V_e is positive (left area of the axis), no electrons can reach the target; when V_e is negative (right area of the axis), electrons reach the target and induce post-ionization, $-eV_e$ is the electron incident energy.

The secondary ion yield can be described as:

$$I_s^{total} \Big/ I_i = Y(\alpha + \sigma\varphi) \qquad 3\text{-}3$$

Where Y is the number of secondary particles produced per incident ion, α is the ionization probability without post-ionization, σ is the cross-section for electron impact ionization which is controlled by the energy of the electron, and φ is the electron flux. Among the many factors which affect the secondary ion yield, the primary electron energy and current are the two most important parameters which can be precisely controlled in this experiment. Different incident electron energy has different post-ionization cross-section, and the ionization rate also depends on the primary electron current.

Experimental test has been carried out to find out how the electron current will affect the secondary ion yield. With same biasing condition, the electron source chamber was operating at different conditions to get different primary electron currents. In measurement 1, the electron source chamber is operating at an RF power of 20W. A weak plasma was ignited to generate a small electron current. The secondary ion yield is measured as a function of V_e. Then the RF power on the electron source chamber was increased to 40W, much brighter plasma was ignited, and the similar data set was recorded in measurement 2. The two sets of data were plotted in the same diagram (figure 3.15) for comparison. In the two cases, the primary electron current in measurement 2 is roughly 8 times bigger than the low electron current in measurement 1. The two curves indicate high electron current and low electron current cases respectively. Compared with the low electron current case, the peak secondary ion yield for the higher electron current case is almost five times higher. This indicates post-ionization plays a very important role in secondary ion yield enhancement.

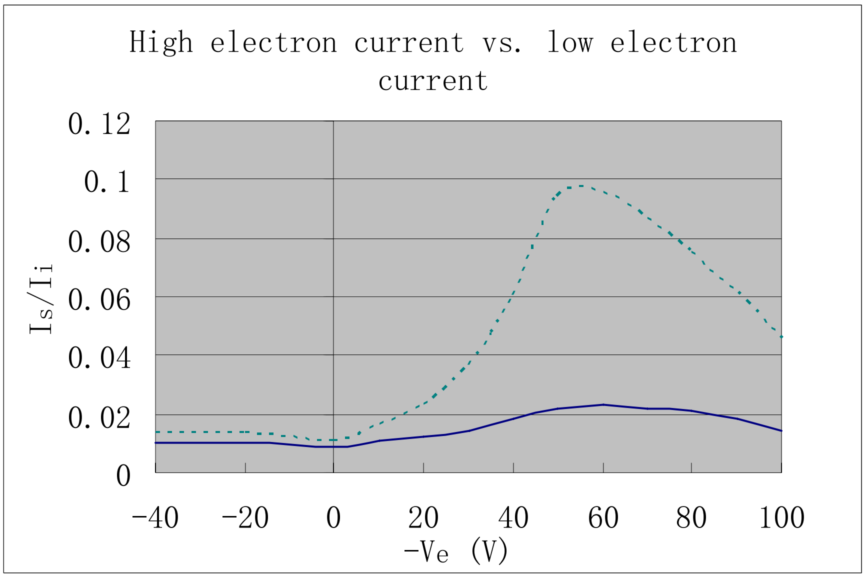

Figure 3.15: "partial" secondary ion yield I_s/I_t is plotted as a function of electron source biasing voltage V_e. The green dot line is measured under high primary electron current and the blue line is measured under low primary electron current.

As can be determined from the previous experiment and discuss, even higher secondary ion yield can be achieved by further increasing the electron current, or, in another word, by adjusting the ratio of the primary ion beam current and the primary electron current. In measurement 3, the electron source chamber was operating at 40W with a bright plasma. The RF power on the ion source chamber is reduced from 50W to 20W to lower the extracted primary ion beam current. So in the combined beam, electron beam is taking a bigger portion than that in measurement 2. Both of the data sets were plotted in a same diagram as shown in figure 3.16. The "partial" secondary ion yield I_s/I_t in measurement 3 in is 12 times bigger than that in measurement 2. The ion current is about 10 times lower in this measurement than that in the previous measurement.

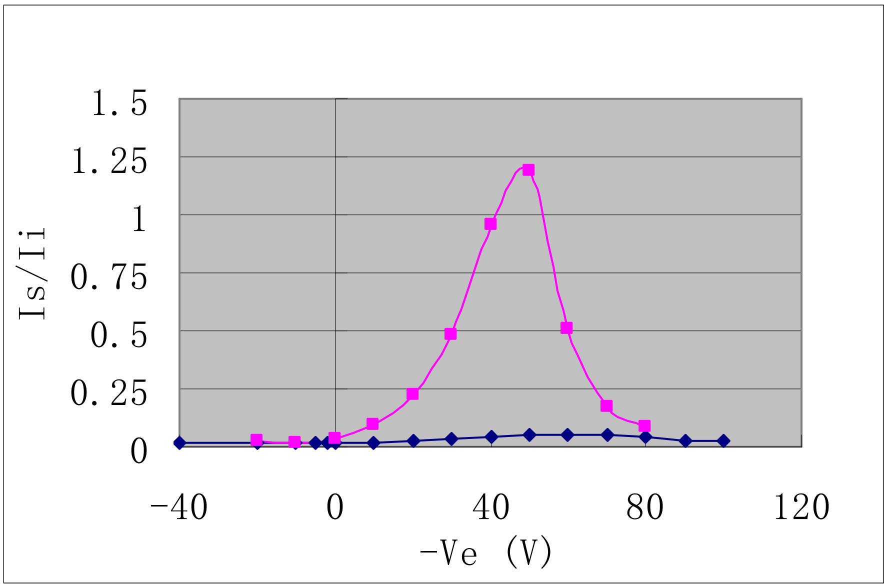

Figure 3.16: "partial" secondary ion yield I_s/I_t is plotted as a function of electron source biasing voltage V_e. The red line is measured under low primary ion current and the blue line is measured under high primary ion current, the primary electron current for each case is the same.

3.4.5.2 Experimental results on insulating target

The combined beam system demonstrated additional advantages when applied to insulating targets. The low energy electrons in the combined beam not only induce electron post-ionization but also compensate for the positive potential from the surface charging. Thus the analysis efficiency on insulating materials is greatly improved.

In this experiment, a small piece of Teflon replaced aluminum as the target material. It is attached on a grounded backing electrode which is used to define the potential. Current on the backing electrode I_b and the secondary ion detector current I_s are monitored. When the electron source is biased positively, only the focused positive ion beam reaches the insulating material, the sample charges up very quickly.

As the positive potential on the sample surface built up, it started to change the ion optics. The beam spot size was broadened, and eventually the potential on the sample surface is so high that some of the ions started to be deflected out from the analytic area onto the backing electrode and even were deflected into the secondary ion detector. Figure 3.17 illustrate the concept schematically.

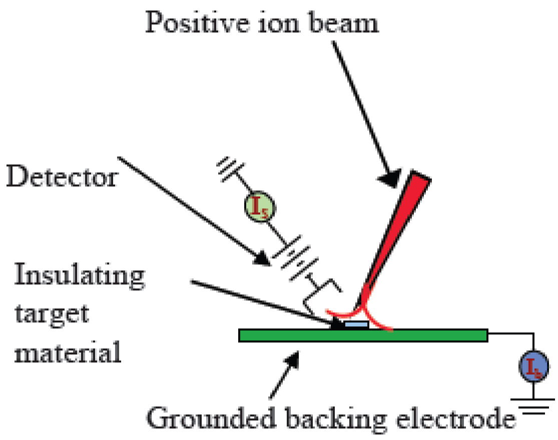

Figure 3.17: Schematic of the sample charging effect. The positive potential on the charged-up insulating sample surface direct the primary ion beam out from the sample, the primary ions are collected on the grounded backing electrode and the secondary ion detector.

As shown in figure 3.18a, both the currents on the backing electrode and the signal detector are high at positive V_e range, which confirms that due to the surface charging problem, the primary ion beam is deflected. When the electron source biasing voltage decreases and becomes closer to ground, the electrons are able to approach the sample surface closer. The deflected primary ion beam shrinks back by the electron cloud near the sample as indicated by the current drop on both I_b and I_s. In the negative V_e region, electrons reach the sample surface, and sample charging is compensated, so there is no more current detected on the backing electrode. So it can be concluded that the left part of the plot demonstrated the surface neutralization effect very well. On the right part of the plot, the secondary ion current starts to increase from a very small value (6nA) to a maximum value (470nA) at electron energy of around 35 eV (figure 3.18b). The secondary ion current is almost two orders magnitude higher with the electron beam flooding on the sample surface.

The big increase of the secondary ion current signal may due to two reasons: first, the electrons ionized a big percentage of the secondary neutrals; second, Teflon is a polymer, during the primary ion sputtering, some of the segments sputtered from the sample are still in the form of big molecules. Those big molecules were broken by the low energy electrons into much smaller segments, which were further ionized and contribute to the great increase of the secondary ion signal.

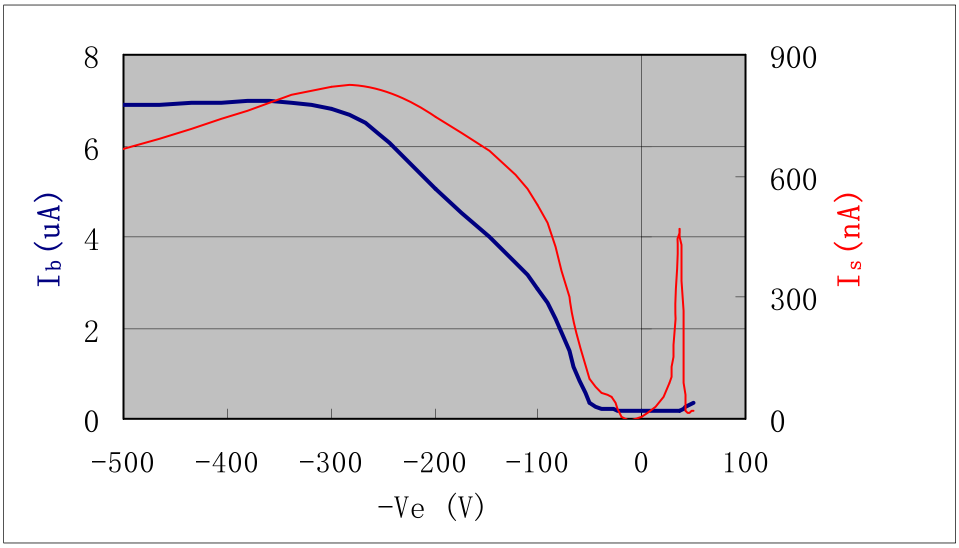

(a)

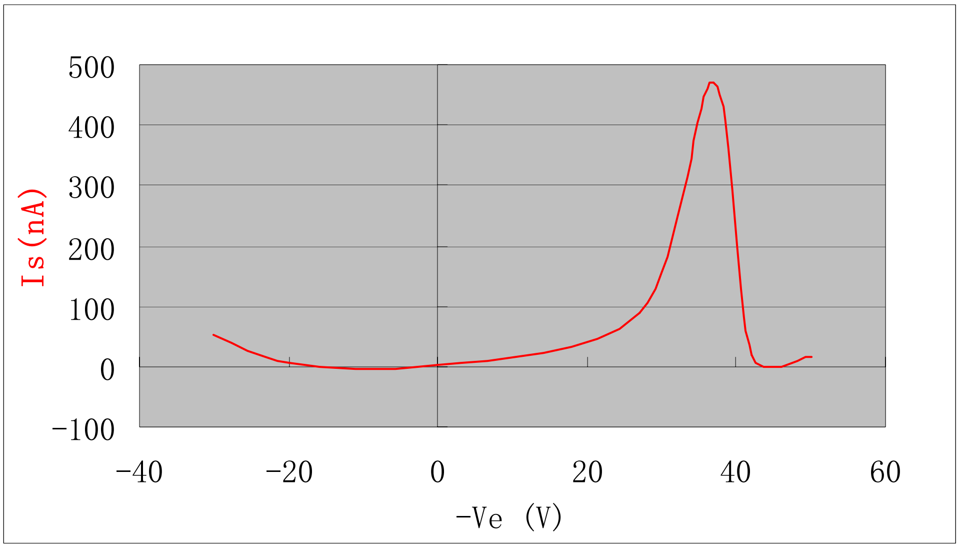

(b)

Figure 3.18: (a) Current measured on the secondary ion detector I_s and on the backing electrode I_b are plotted as the function of V_e when the target is an insulating material (Teflon). (b) I_s measured at a small range of electron biasing voltage.

3.5 Discussion and summary

In summary, the combined electron and focused ion beam system provides a new way to improve the performance of the SIMS instruments. The self-aligned, low-energy electron beam introduces an electron post-ionization effect, and a surface neutralization effect. Therefore, secondary ion yield and signal can be enhanced for both conducting and insulating target materials. During the experiment, it has also been observed that the primary ion beam current density increases with the presence of the electron beam, which may come from the reduced space charge effect. More experimental and computational investigation of this effect is being carried out.

There are some facts need to be pointed out about the experiment:

A couple approximations and assumptions have been made during the previous discussion, such as:

1. The secondary ion and secondary electron currents have been neglected from the total target current when adding the primary electron current and the target current together to get the primary ion current. Thus the calculated partial secondary ion yield differs from the real value, even though the approximation won't affect the shape of the partial secondary ion yield curve and the conclusion which has been made above.

2. When the electron source biasing voltage changes from 40V to -100V, with the ion source biasing voltage fixed at 1.3kV, the voltage difference between the two source increases and the extracted electron current also increases with the voltage. So on those plots of the partial secondary ion yield, there is more electron induced post-ionization on the right side of the plot than that on the left side.

3.5.1 Electron post-attachment

When the energy of the electrons in the combined beam is tuned down to very low value, there is an increased chance for electrons to attach to the sputtered neutrals, this is called electron post-attachment. Electron attachment usually happens when the velocity of the electron and the secondary neutral are the same or very close. Since

$$E_e = \frac{1}{2} m v_e^2 \qquad E_n = \frac{1}{2} M v_n^2 \qquad v_e \approx v_n \tag{3-4}$$

where E_e, E_n are the kinetic energy of the primary electrons and the sputtered secondary neutrals, v_e and v_n are the velocities. For a sputtered neutral with mass of M, the energy of the electron which has the biggest cross-section for attachment can be expressed as:

$$E_e = \frac{m}{M} E_n \qquad 3\text{-}5$$

Since M >>m and E_n is usually within couple tens eV, E_e is very close to zero.

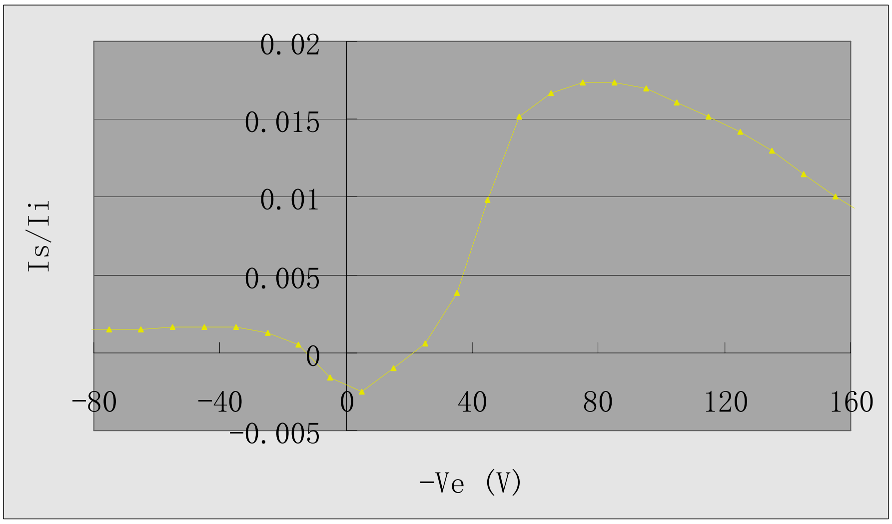

Figure 3.19: A small Is/Ii drop happened at low electron energy region, which may partially due to electron post-attachment effect.

During the experiment shown in figure 3.19, when the secondary ion current is small (Is/Ii is within only a few percent), a small drop of the secondary ion current was observed at the low electron energy area near Ve = 0. Electron post-attachment may contribute a little for that phenomenon. But the target material is Al, which has a very small cross-section for electron post-attachment, most possibly, the current drop is because an electron cloud is formed near the surface of the sample when the incoming electron energy is low, the negative electron cloud confines the positive secondary ions and stop them from emitting to the secondary ion collector, which cause a current drop on the secondary ion collector.

The electron induced post-attachment will help in increase the secondary ion signal for negative secondary ion detection. But a better experimental design instead of the current experiment setup is necessary. The secondary ion collector need to be biased positively to repel positive secondary ions, also an electron filter is required to filter the electrons. This will be another interesting topic to explore on the combined electron and positive ion system.

References:

[1] A. Benninghoven, F. G. Rüdenauer, and H. W. Werner, "Secondary Ion Mass Spectrometry: Basic Concepts, Instrumental Aspects, Applications, and Trends", Wiley, New York, (1987).

[2] Q. Ji, L. Ji, Y.Chen, and K.-N. Leung, *Appl. Phys. Lett.* 85, 4618 (2004)

[3] X. Jiang, Q. Ji, A. Chang, K.N. Leung, Rev. Sci. Instrum. 74, 2288 (2003).

[4] S.M. Daiser, *IEEE Circuits and Devices Magazine* 7 (4): 27-31 (1991)

[5] I. Veryovkin, W. Calaway, C. Tripa, J. Moore, A. Wucher, M. Pellin, *Nucl. Instrum. Methods Phys. Res. B* 241, 356 (2005)

[6] O. Ameziane, J.M. Blanco, J.J. Serrano, B. Guzman, and M. Aguilar, *Eur. Phys. J. AP* 22, 231 (2003)

[7] A. Schnieders, R. Mollers, A. Benninghoven, *Surf. Sci.*471, 170 (2001)

[8] M.J. Pellin, G.K. Nicolussi, *Proceedings of the SPIE The International Society for Optical Engineering,* 3270, 148 (1998)

[9] H.Oechsner, W. Ruhe, and E. Stumpe, *Surf. Sci.*, 85, 289, (1979)

[10] T. Fister, T. Schuerlein, P.Lindley, http://www.eaglabs.com/en-US/papers/papers.html.

[11] J. C. Vickerman, A. Brown and N. M. Reed, *Secondary Ion Mass Spectrometry Principles and Applications*, Clarendon Press, Oxford, (1989)

Chapter 4

Computer simulation of the combined electron and focused ion beam system

4.1 Background for the simulation study

In chapter 3, a combined electron and focused ion beam system has shown its particular advantages in reducing sample surface charging as well as the space charge effect of the ion beam. What is more interesting is the demonstration of the electron beam induced post-ionization effect, which will make it a very promising candidate for Secondary Ion Mass Spectroscopy (SIMS). The potential of the combined beam being able to increase ion current density can even further extend its advantages in Nano-SIMS applications.

Differing from current available ion beam tools, the new system combines positive ions and negative electrons together in one beam. This new form of beam contains species with different mass and different charge polarity which brings up a lot new opportunities and applications, at the same time, the opposite response to electric and magnetic field of the ions and electrons has raised new requirements and challenges to the system design, such as beam optics design, beam deflection design and beam pulse generator design etc. Details of how to design the beam optical column, beam deflector and beam pulsing will be discussed one by one in this chapter.

The previously tested system is a prototype for principle demonstration. The beam spot size is a couple hundred microns determined by the size of the extracting aperture and the single gap extraction electric field, which is not suitable for many applications where finely focused ion beam is required. To push the system into real applications, a more delicate design of the system is a must. First of all, ion optics is the most important thing to be improved. For the prototype device, no designed ion optical lens was employed. Instead, only a simple set of electrodes was involved for concept demonstration. As mentioned in the previous chapter, there are some issues related to the poor ion/electron optics, such as low achievable electron current, secondary electrons generation, electrodes heating and degradation due to the huge amount of electrons hitting on the electrodes (only less than 10% of the electron current is finally present in the combined beam). But till now there is no available simulation software which can simulate electrons and positive ions simultaneously. This makes it very difficult to design an optics column for the combined beam.

Basically, when a combined negative electron beam and positive ion beam passing through an electric field simultaneously, we can consider that there are three different forces affecting the movement of each particle. An electron, for example, is affected by the electrostatic force imposed by the electric field, the Coulomb force from all the other local electrons and the Coulomb force from all the local positive ions. Compared with the single beam case, the Coulomb force from the other species is the new additional force introduced by the combined beam. In another word, for a single positive ion beam, only electrostatic force and space charge affect the beam trajectory; but when a combined electron and positive ion beam replaces the single ion beam, interaction between electrons and ions has to be considered in order to determine both the ion beam and the electron beam trajectory.

Lack of appropriate simulation tool, the design of the optical column for the combined beam has been conducted in two steps: First, using the available simulation software to design a “reference” optical column ignoring the interaction between electrons and positive ions. Since for the combined electron and focused ion beam system, we are not talking about very high current, electron and ion interaction can be ignored on the first order approximation. In the meanwhile, a new simulation code was being developed at Lawrence Berkeley National Laboratory by Taneli Kalvas, which is capable of calculating the movement of multiple charge particle species with different charge polarities simultaneously. With the help of that simulation code, the previous design configuration of the optical column can be benchmarked and corrected more precisely.

The ion beam energy in this design has been set at 4 keV; a tunable electron energy is desired from couple tens eV to about 100eV, in this way the electron energy can be optimized for different target materials. Since electron beam and positive ion beam go through the same optical column, while ions are accelerating, electrons are decelerating. To ensure both ions and electrons can reach the target, there is a limitation for the voltages on the electrodes in the column. In this case, the lowest voltage V_- cannot be smaller than V_e (the electron source biasing voltage), which corresponds to the lowest electron energy. Otherwise, the potential barrier will stop the electrons from getting across and reaching the target. For similar reason, the highest voltage V_+ can not be bigger than V_i (the ion source biasing voltage). This is illustrated in figure 4.1.

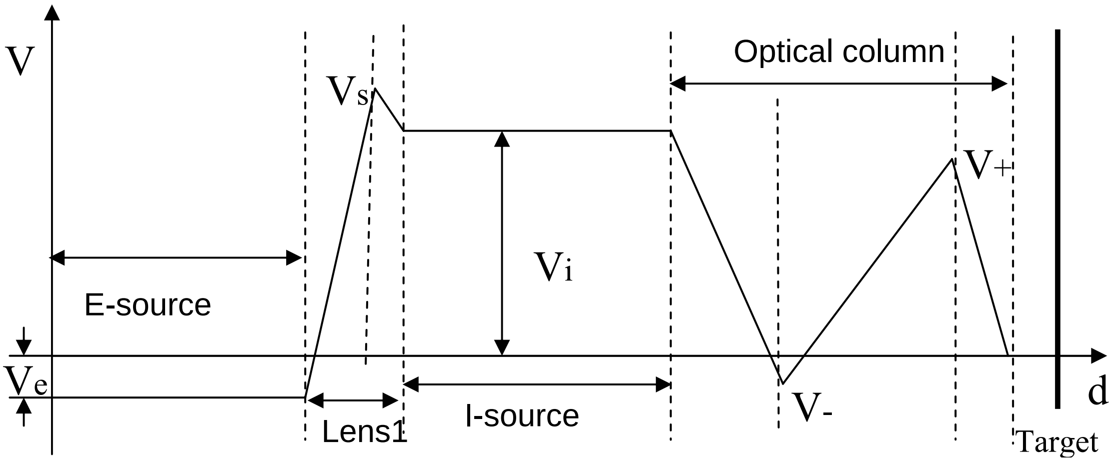

Figure 4.1: A schematic showing the potential distribution of the combined electron and focused ion beam system, started from the electron source (left side) to the target (right side).

The goal of the optical column design is to deliver the combined electron and positive ion beam and form a focused high energy positive ion beam and low energy electron beam at the sample target. The electron beam does not necessarily to be a focused beam. Instead the electron beam spot size will be designed much bigger than that of the ion beam on purpose. The reason is discussed in below.

In most ion beam applications, ion beam deflection is required to direct the ion beam writing patterns on the sample. This usually is not an issue for a conventional focused ion beam system, but it brings up problems for the combined beam. With opposite charge polarities, the electron beam and the positive ion beam in the combined beam will be deflected in opposite directions. This means the ion beam and the electron beam will be separated instead of being "combined". But this can be compensated by making the electron beam spot size much bigger than the ion beam spot size. The concept is illustrated in figure 4.2. If both electron beam and ion beam have comparable beam spot size as shown in the left side scenario, when the deflector turns on, ion beam and electron beam shift to different locations and become two separate beams. But if the electron beam spot size is much bigger than the ion beam spot size as shown in the right side of the figure, even though the electron beam and the ion beam are deflected in opposite directions, the big electron beam spot can still cover the area where ion beam irradiates on. Also, the electron beam is not necessarily to be a focusing beam for neutralization purposes.

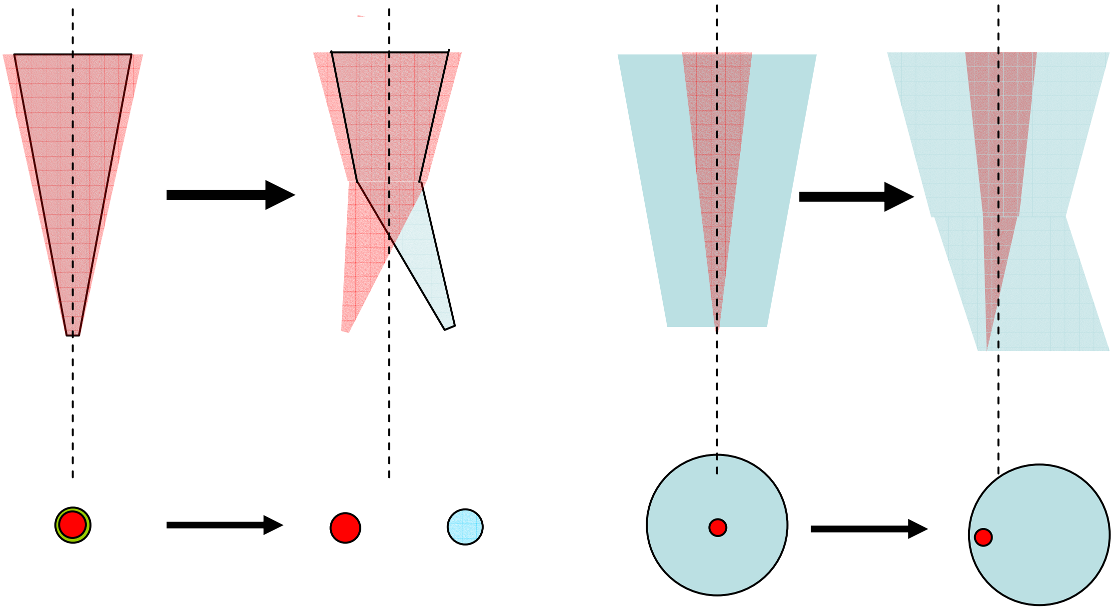

Figure 4.2 Deflection concept for the combined beam: (left) ion beam and electron beam have comparable beam spot sizes and are separated by deflection; (right) electron beam has a much bigger beam spot size, it can still cover the ion beam after beam deflection.

4.2 Simulation of the ion accelerator column by using the Munro code

Simulation design was first carried out using Munro code. A compact two-lens system design was used for the combined beam delivery. The lens configuration and ion beam trajectory is shown in figure 4.3a. The first part of the column is consisted of a counter-bore shaped plasma electrode and a second electrode for extracting the ion beam. The counter-bore shaped plasma electrode is at the same potential as the ion source, which is 4000 V, and the second electrode is biased at -1100 V relative to the plasma electrode. The following part of the column is an Einzle lens with three electrodes, which is for focusing the extracted ion beam in a decelerating-accelerating mode. The electron beam trajectory is shown in figure 4.3b. According to the Munro simulation based on a 10 μm extraction aperture, the demagnification for the ion beam achieved on this two-lens system is about 10, and the aberration information is listed in table 4-1. This result is corresponding to the case where only ion beam or electron beam alone is passing through the optical column, it didn’t take into account of the interaction between the ions and electrons, but it provides a reasonable design reference for the combined beam case. Based on this simulation result, only minor modification will be needed.

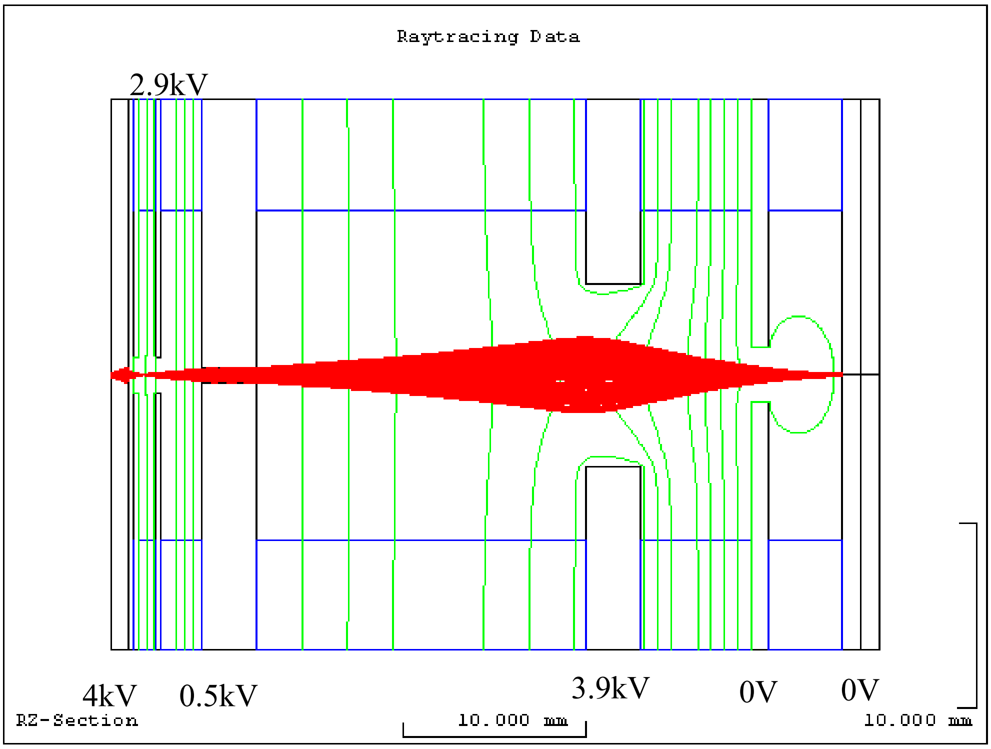

Figure 4.3a: The layout of the two-lens system design, and the ion beam trajectory calculated by using the Munro ray tracing (SORAY, SORAYP) programs.

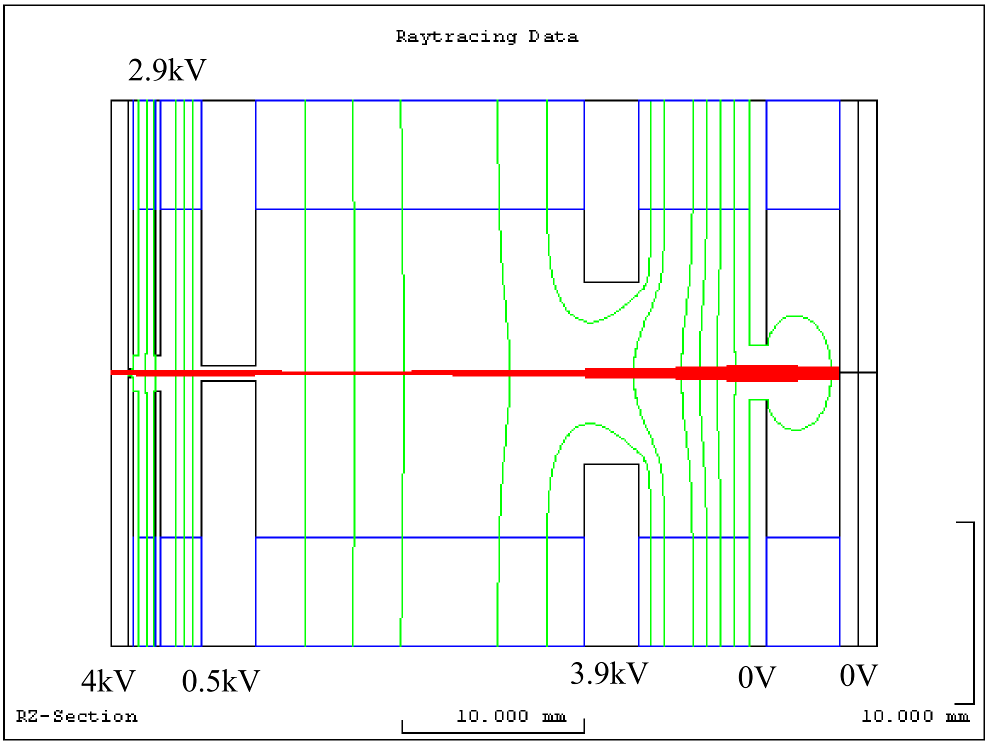

Figure 4.3b: The electron beam trajectory calculated by using the Munro ray tracing (SORAY, SORAYP)programs with initial energy of 100 eV.

Mag.	Spherical aberration	Coma	Field curvature	Astigmatism	Distortion	Chromatic aberration	Total Blur
0.104	0.086 µm	0.005 µm	0.002 µm	0.001 µm	0.001 µm	0.139 µm	0.146 µm

Table 4-1: Magnification and aberration for the two-lens ion optical column with a 10 µm aperture calculated by Munro simulation code.

4.3 Simulating electrons and positive ions simultaneously using the IBSimu code

After the first stage of simulation work, electrons and ions interactions need to be considered in the calculation to modify and improve the optical design. A computer program for 3D ion beam simulation-- "IBSimu" has been developed and optimized to address this design issue by Taneli Kalvas from the Ion Beam Technology (IBT) group at Lawrence Berkeley National Laboratory.

IBSimu combine the particle-in-cell (PIC) technique commonly used for plasma modeling with a description of the "lattice" of electrode elements. IBSimu is a time-dependent plasma code. The particles are advanced in time and the applied fields are applied directly to update the particles' momentum. The calculation can follow the time-dependent evolution of beams, or can efficiently be used to study steady-state beam behavior in 3-D or 2-D by solving for the self-consistent field only infrequently or using an iterative method. The beam can be initially generated from one of several general distributions or from first principles via space-charge-limited injection from an emitting surface. The self-consistent field is assumed electrostatic- Poisson's equation is solved on a Cartesian mesh that moves with the beam[2]. Both positive charged particles and negative charged particles are included in the calculation by specifying beam current, charge and mass for different particle species. Typical IBSimu simulations consist of three steps. First, a geometry is made for the simulation. In the second step the simulation is run using a custom program made for the problem at hand. After running the program, the output data is analyzed with a post-processing tool, if necessary. The data analysis and output can also be made with the program running the simulation. Typically the running program is written in C programming language. But so far the IBSimu program does not have the capability to give out aberration information, only beam trajectory can be simulated.

Lens geometry and potential distribution designed by Munro code has been applied to the IBSimu code, beam trajectories were calculated starting with this condition, and then based on the calculated beam profile, voltages and the geometry of the electrodes were adjusted to modify the previous design. After modification, the beam trajectories for the final design of ion beam only, electron beam only and the combined beam are calculated and shown in figure 4.4 a, 4.4 b and 4.4 c.

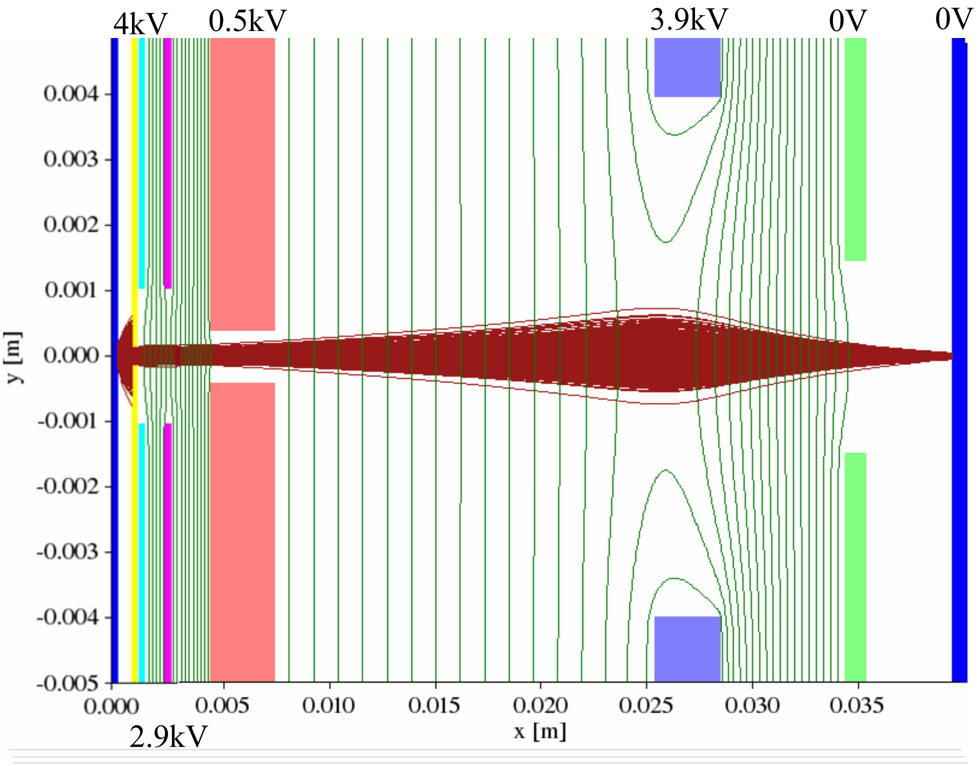

Figure 4.4a: The ion beam trajectory simulated by using the IBSimu code.

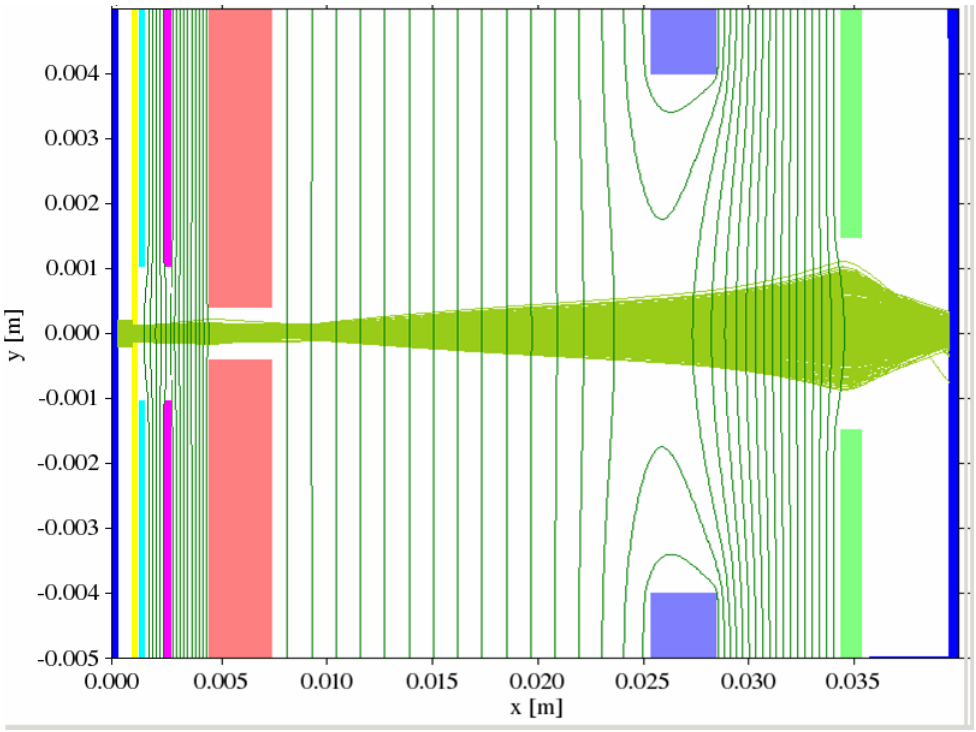

Figure 4.4b: The electron beam trajectory simulated by using the IBSimu code.

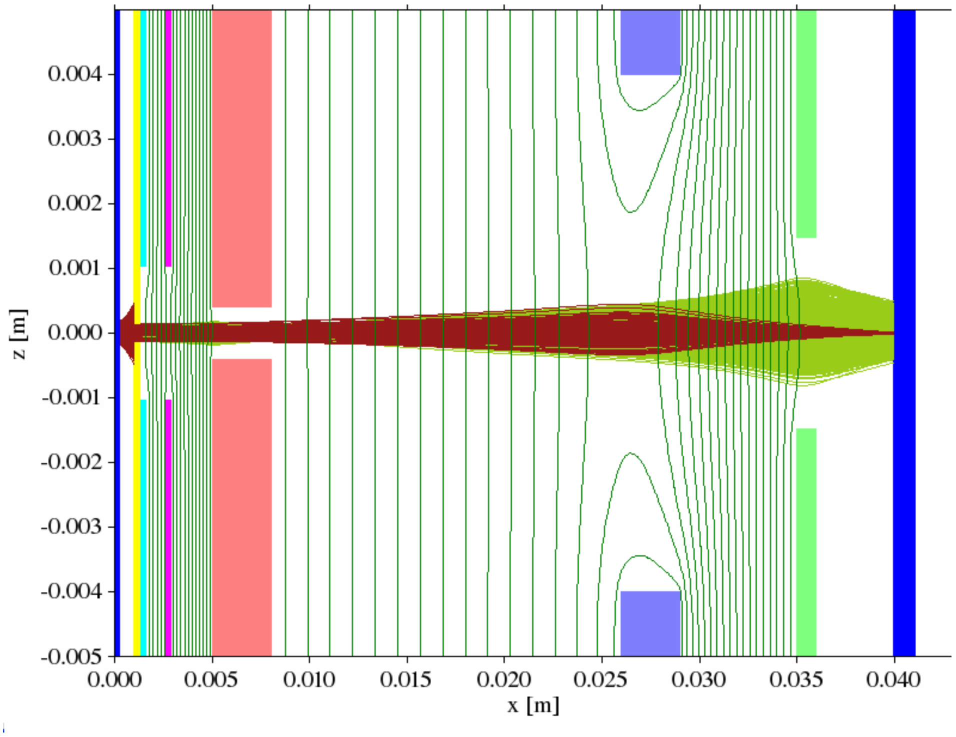

Figure 4.4c: The trajectory of the combined electron and focused ion beam simulated by using the IBSimu code.

4.4 Simulation of beam deflection

Beam deflection is also simulated using the IBSimu code. To deflecting the beam, the last electrode of the Einzle lens is split into two segments instead of keeping a whole cylindrical piece. A +10V and a -10V bias relative to the original voltage are added on each of the parts respectively. The beam trajectory after beam deflecting is shown in figure 4.5.

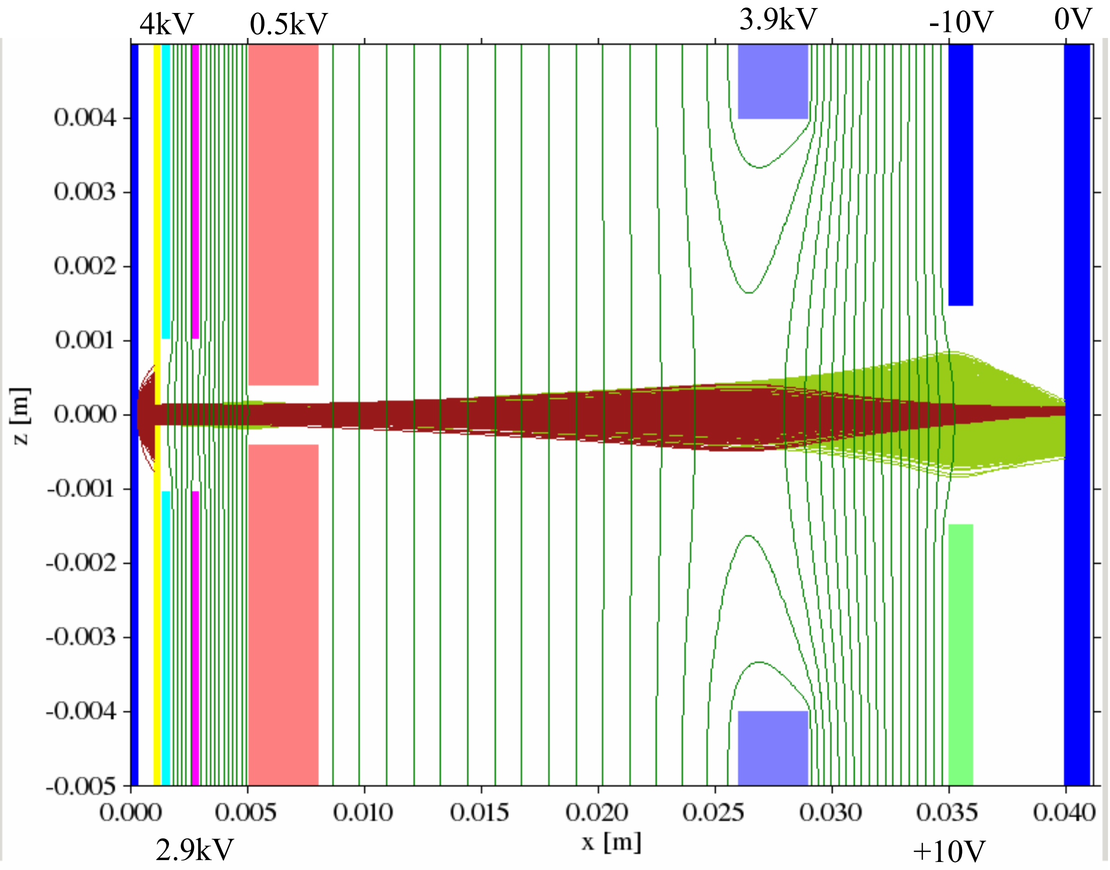

Figure 4.5: The beam trajectory of the combined beam with beam deflection simulated using IBSimu code.

4.5 Pulse generation for the combined beam

Design of a combined beam pulse generator with pulse width of 50ns and duty factor of 50% is discussed below.

A deflecting electric field is designed to turn the beam “ON” and “OFF” by deflecting the ions and electrons away so that they can not pass the exiting aperture of a beam collimator. As illustrated in figure 4.6, a DC pulsed voltage signal is generated between two parallel electrodes, when the voltage is switched on, the positive ions and electrons trajectories are bended by the electric field to opposite directions and in different curvatures, thus no beam reaches the sample target. This time period is pulse "OFF" period. When the electric field is shut off, the combined beam will go straight and then the beam on the target is switched "ON". The pulsing time and duty factor are controlled by the pulsing signal on the electrodes and the geometry of the pulse generator.

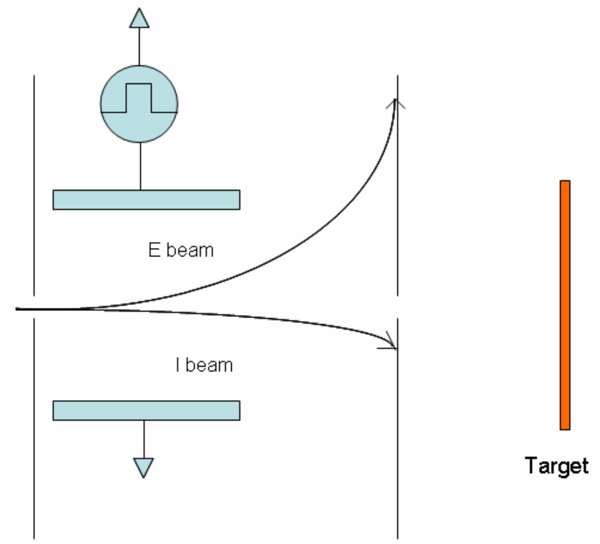

Figure 4.6: Schematic of the beam pulse generator.

To design a pulse generator for this combined beam, energy/ velocity difference between the positive ion (Ar^+) and the electron is a big concern.

For a combined beam consisting of 4kev Ar^+ ions and 50ev electrons, the

velocity of Ar^+ ion $V_i = \sqrt{\frac{2E_i}{M}} = 1.386*10^5$ m/s, 4-1

and the velocity of electron $V_e = \sqrt{\frac{2E_e}{m}} = 4.193*10^6$ m/s. 4-2

The total time for Ar^+ to travel through the deflecting field L_d and the field-free region L_f to the sample surface is $t_i = \dfrac{L_d + L_f}{V_i}$ 4-3

And the travel time for electron is $t_e = \dfrac{L_d + L_f}{V_e}$ 4-4

A DC pulsing voltage signal with 50ns pulse time and 50% duty factor is applied on the deflecting electrodes. In 50ns Ar^+ can travel about 7mm which is the length for the deflecting field; electron can travel about 210mm in the axial direction. Since electron moves much faster than Ar^+, the travel time is a lot shorter. To ensure ions and electrons can reach the sample target at same time, the difference between t_i and t_e need to be

$$t_i - t_e = N * 50ns \qquad (N=1,2,3,4\ldots..) \qquad 4\text{-}5$$

But this also means for the first N cycles after the pulse generator turned on, only electron beam will hit on the sample target due to the velocity difference of ions and electrons.

Simulation of the dual beam pulse generator has been performed using the XOOPIC code. XOOPIC[3] (Object Oriented Particle in Cell code for X11-based Unix computers) is presently a serial 2D particle-in-cell plasma simulation. It is time explicit, fully electromagnetic simulation. This effort focuses on using parallel and distributed processing to optimize the simulation for large problems. The benefits include increased capacity for memory intensive problems, and improved performance for processor-intensive problems[3]. The standard PIC (Particle in Cell) scheme solves the equations representing a coupled system of charged particles and fields. The particles are followed in a continuum space, while the fields are computed on a mesh. First, forces due to the electric and magnetic fields are used to advance the position. Particle boundary conditions such as emission and absorption are then applied. If collisions with background atoms are included, the velocities are updated to reflect elastic and inelastic collisions. Next the particle positions and velocities are used to compute the charge density and current density on the mesh. The charge density and current density provide the source terms for the integration of the field equations (Poisson equation in the electrostatic limit, Maxwell's equations in the electromagnetic limit) on the mesh. The fields resulting from the integration are then interpolated to particle locations to provide the force on the particles[4].

Ions and electrons movements in the pulse generator are simulated separately using the XOOPIC code and the simulation is time-dependent. Results of the beam trajectory at some certain time points are shown in figure 4.7 and a plot showing electron and ion current pulses with time dependence in the first 10 cycles after the pulse generator turned on is also shown.

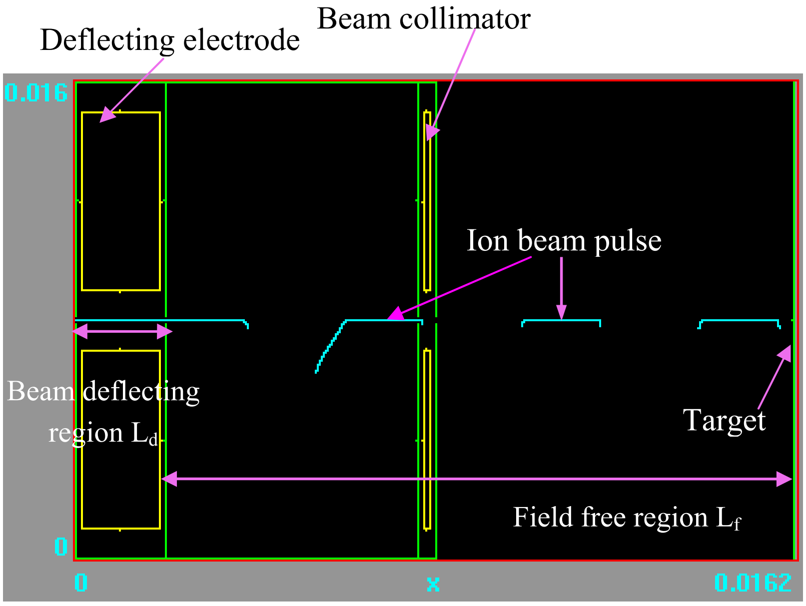

Figure 4.7 a1: During the pulse “off” period, the positive ions have not reached the target.

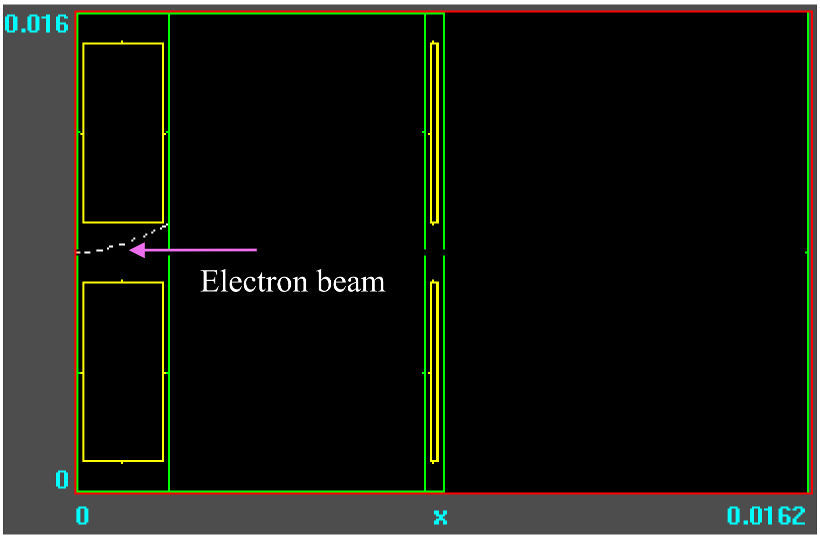

Figure 4.7 a2: During the pulse “off” period, electrons are deflected on the deflecting electrodes.

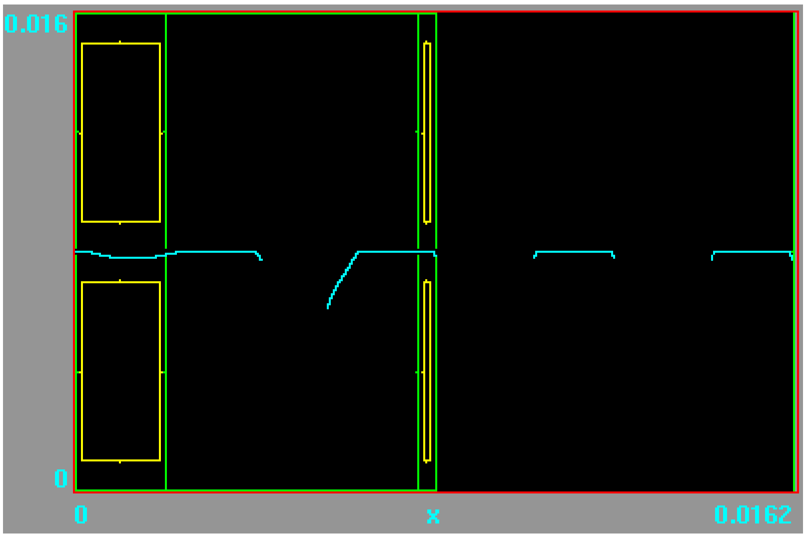

Figure 4.7 b1: The time when the electric field is shut off, one ion pulse starts to reach the target.

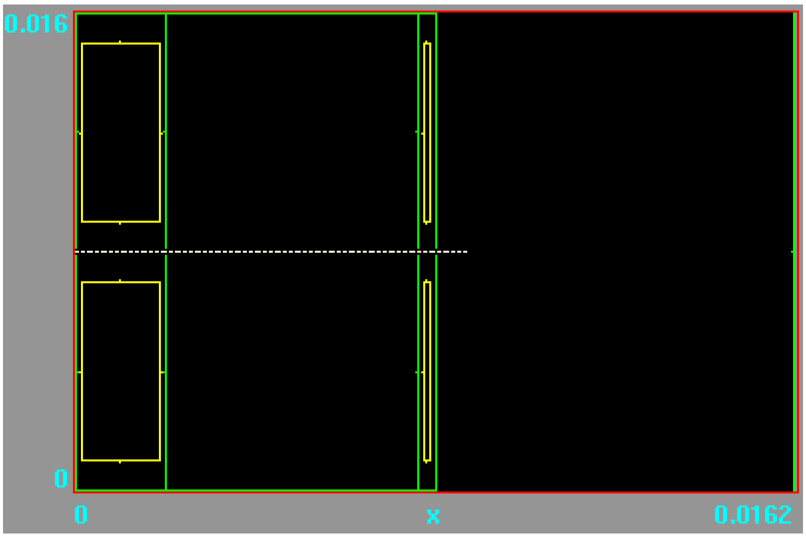

Figure 4.7 b2: The time when the electric field is shut off, electrons starts to travel straightly through the collimator.

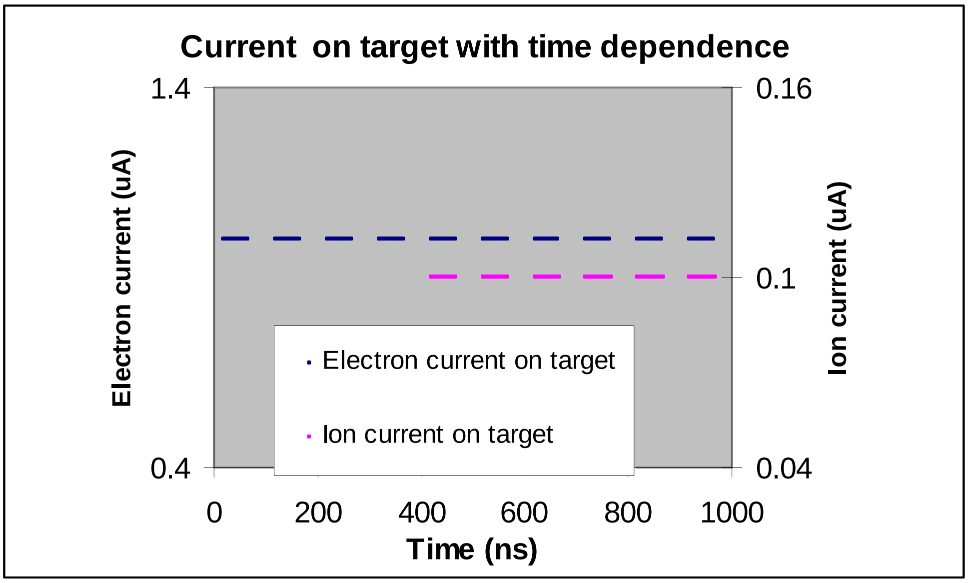

Figure 4.7c: Ion and electron current on the target with time dependence for the first 10 periods after the pulse generator is turned on. In the first 4 periods, only electrons hit on the target.

4.6 Space charge reduction effect

In the simplest sense, space charge effects are a consequence of the mutual repulsion between particles of like charge. Space charge is a consequence of Coulomb's law, which quantifies the force (F) between two point charges (q and q') separated by a distance r as:

$$F = k(qq'/r^2) \qquad \text{4-7}$$

where k is a proportionality constant that depends upon the units chosen for the other variables in equation 4-7. Note that Coulomb's law describes both the force of attraction between particles of opposite charges, and the force of repulsion between like charges. In a charged particle beam, the particles (ions) are usually of like charges, and the intervening medium (a vacuum) does not mediate the force significantly.

However, even at atmospheric pressure, the correction is relatively small. Space charge changes the effect of an external field (such as a focusing lens) on the ion beam of an external field, either reducing or increasing any focusing action otherwise achieved. Rigorous derivation shows that the space charge effect increases with the amount of ion current carried by the beam (more ions result in more space charge), and is inversely proportional to the ion velocity (slower ions are more perturbed in their trajectories than faster moving ions).

Compared the ion beam in the combined beam with a single positive ion beam, the ion beam in the combined beam has a negative charge background supplied by the electron beam, it induces Coulomb's attraction force which cancels the Coulomb's repelling force among the positive ions, thus reduces the space charge effect. This effect has also been investigated by IBSimu simulation. Different ion currents are applied to the combined-beam system, both ion beam only case and ion beam with electron beam case are simulated and the beam distribution cross-section at the target surface are plotted in figure 4.8.

As shown in figure 4.8a, for ion beam only case, when the ion current increased from 10^{-7}A to 10^{-5}A, the ion beam spot size increased about 15% due to increased space charge effect. When electron beam is also present with ion beam, the ion beam spot size further decreases as shown in figure 4.8b. This simulation result is consistent with the experiment data shown in figure 3.5b.

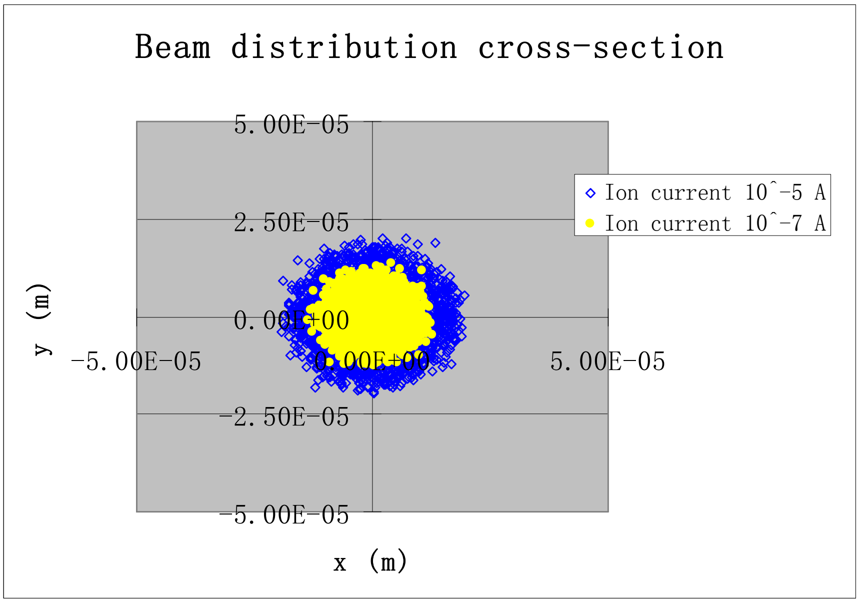

Figure 4.8a: Beam distribution at the sample surface calculated by the IBSimu code. Ion beam only case. Two ion currents are compared.

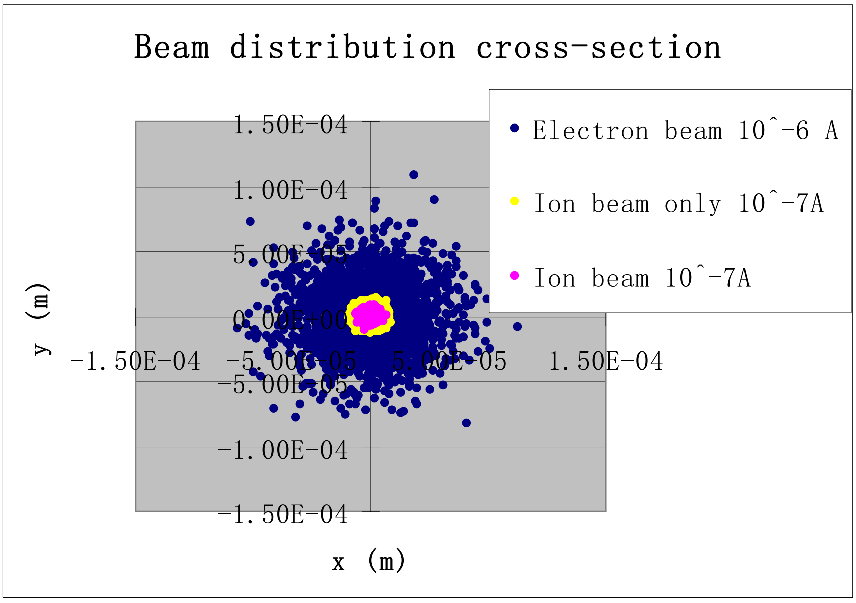

Figure 4.8b: Beam distribution at the sample surface calculated by IBSimu code. Yellow dots represents ion beam only case. Blue dots and pink dots represent electrons and ions in the combined beam.

Reference:

[1] www.cc.jyu.fi/~tvkalvas/thesis.html

[2] www.hif.lbl.gov/theory/WARP_summary.html

3 www.slac.stanford.edu/econf/C980914/papers/L-Tu28.pdf

[4] J.P. Verboncoeur, A.B. Langdon, and N.T. Gladd, “An object-oriented electromagnetic PIC code.” Computer Physics Communications 87, 199-211 (1995).

Chapter 5:

Ion source for metallic ion beam generation and thin film deposition

Ion beam has played an important role in semiconductor manufacturing, nanoscience and technology and many other research fields. Currently, high resolution ion beam processing is limited to mostly gallium ion beams. The drive towards controlling materials properties at nanometer scales relies on the availability of more flexible tools. Besides H^+, He^+, Ar^+, O^+, B^+, and P^+,[1] there has been an increased need for metallic ion beams such as transition metal ions (V^+, Cr^+, Mn^+, Fe^+) [2] for ion implantation in new material research, magnetic species (Ni^+, Fe^+) for magnetic-film manufacturing, and some special metallic ion species (Cd^+, Ca^+) for biophysics and medicine research[3]: for example, applications of metal ion-protein binding. RF-driven plasma ion sources have been widely used to generate various ion beams of gaseous substance. Ion sources capable of generating various metallic ions are highly desired for extending the application areas of ion beam.

A compact RF-driven ion source was developed for generation of metallic ion beams. The source is capable of generating various metal ion species. Almost any solid-state metal materials in the forms of a rod, a tube or a foil can be assembled into the source for generating metal ions. Many species have been tested such as: copper, iron, nickel, titanium, palladium, aluminum, and manganese etc. Combined with an ion extraction, an electro-static lens system and a mass separator, a focused metallic ion beam can be achieved. The source itself can also be used as a sputtering deposition source.

5.1 Source development and operation

5.1.1 Source configuration and operation

The schematic of the first prototype source and its photograph are shown in figure 5.1. The source body is made of cylindrical shaped copper with a circular opening in the middle. The source has an inner diameter of 1.5 inches. Such a small source can be operated at high power density and thus a high plasma density is achievable. A straight thin copper tubing going all the way through in the axial direction acts as an internal antenna. Water flows inside the antenna for cooling purpose. The two leads of the straight antenna are connected to a 13.56 MHz RF power supply through a matching network. The metal material to be sputtered is assembled as part of the RF antenna, exposing into the plasma. All the other part of the antenna is covered with quartz tube. So only the target material will be sputtered. The source has a quite flexible requirement on the configuration of the sputtering target. Tubing, rod and metal foil can all be assembled easily in the source chamber. Thus most of the metallic ion species in the periodic table can be generated using this approach.

Argon is introduced into the source chamber as the background gas to generate plasma. It has relatively high atomic mass, and is chemically stable so that it won't react with the metal materials during the sputtering process. Permanent magnets are installed on the outer surface of the source body, the magnetic field generated by the permanent magnets will confine the electrons from being lost to the source wall. The magnets also help to ignite and maintain high-density plasma.

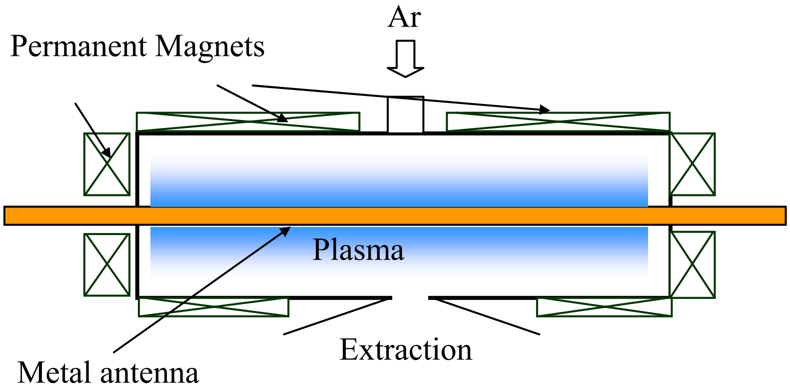

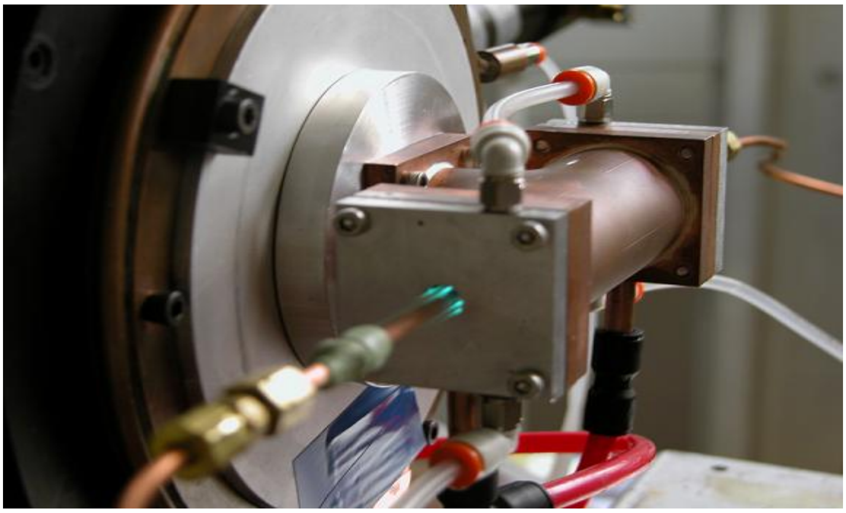

Figure 5.1: Schematic of the sputtering source for metallic ion generation (top) and the photograph of the prototype of the source in operation (bottom).

In order to ignite the plasma in the source, relatively high pressure of argon gas is needed. In this system, over a hundred mTorr argon gas pressure is required. Under 450W forward RF power, plasma with a relatively low density (a very dim plasma) appears first due to capacitive coupling. When the gas pressure keeps increasing, the plasma density becomes higher and higher. When the gas pressure exceeds two hundred mTorr, the plasma jumps into a much brighter high-density inductively-coupled mode. This is also indicated by the change in the RF matching condition. When the plasma mode changes, the plasma density changes greatly, which induces the change of the plasma resistance and inductance, thus affecting the matching condition. In the presence of a plasma, the RF antenna will serve as a sputtering target. Due to the electrode-size effect shown in equation 5-1:

$$\frac{\overline{V}_{RF}}{\overline{V}_{G}} = (\frac{A_G}{A_{RF}})^4 \qquad 5\text{-}1$$

where $\overline{V}_{RF}$ and $\overline{V}_{G}$ are the mean voltages across the plasma sheath around the RF antenna and the grounded source body respectively; A_{RF} and A_G are the area of the RF antenna and the source body, the RF antenna is self-biased at a bigger negative voltage. The argon ions in the plasma sheath are driven onto the antenna surface by this voltage, sputtering off the metal material from the antenna. The metallic neutrals will diffuse into the high-density plasma. Since the ionization potential for most metal species is lower (e.g. 6~7 eV) than argon (15.8 eV), the metal atoms are easily ionized in the high-density argon plasma.

The first ionization potential energy for copper is 7.7264 eV, so a great percentage of the neutral copper atoms are ionized in the high-density plasma. A high ion to neutral ratio compared with other sputtering systems can be achieved with this ion source, which can be seen from the color switch of the plasma. When a great percentage of neutral copper atoms are ionized, the color of the plasma will switch from purple to green (as shown in figure 5.1), which is the characteristic color of copper plasma. The change in color of the plasma is easily observed from a quartz tube extending out from the source.

The straight antenna configuration has several characteristics: First, it is easier to install the metal materials. Second, when the source is used as a sputter deposition source, it is very suitable for uniformly coating the inner surface of cylindrical shaped targets; moreover, it can accommodate a very wide range of the cylindrical target size, big or small, long or short.

The straight internal antenna has a low inductance, and a large part of the antenna is exposed outside the ion source. As a result, the RF power is easily radiated or coupled outside of the system instead of coupling into the support gas. Thus it requires a very good RF shielding and firm grounding to get an effective RF coupling into the plasma.

The prototype source is small with an inner diameter of 1.5” and 4” long. Thus the power density of this source usually is more than five times higher than a regular commercial sputter machine. This will lead to a much higher plasma density and ion current density. But it also requires fairly high gas pressure to start and maintain the plasma discharge in such a small volume. Usually at least two hundred mTorr gas pressure is required, which is a very heavy load for the pumping system.

In order to reduce the gas pressure and to keep the vacuum at high level, the second source was design and developed. The source size has been enlarged to 12” diameter and 16” in length. Four straight antennas connected in parallel replaced the single straight antenna, forming a cage-like area. The gas pressure required to run this source is ten times smaller, but the enlarged size will reduce the plasma density and therefore the extractable current density.

The new antenna has another advantage: under such a setup, the area surrounded by the antennas can produce the most uniform plasma and the highest plasma density. So when the system is used as a deposition source, the sample is located in the center of this "cage", where the deposited film can be more uniform and the deposition is more efficient. The schematic and the photograph of the source are shown in figure 5.2.

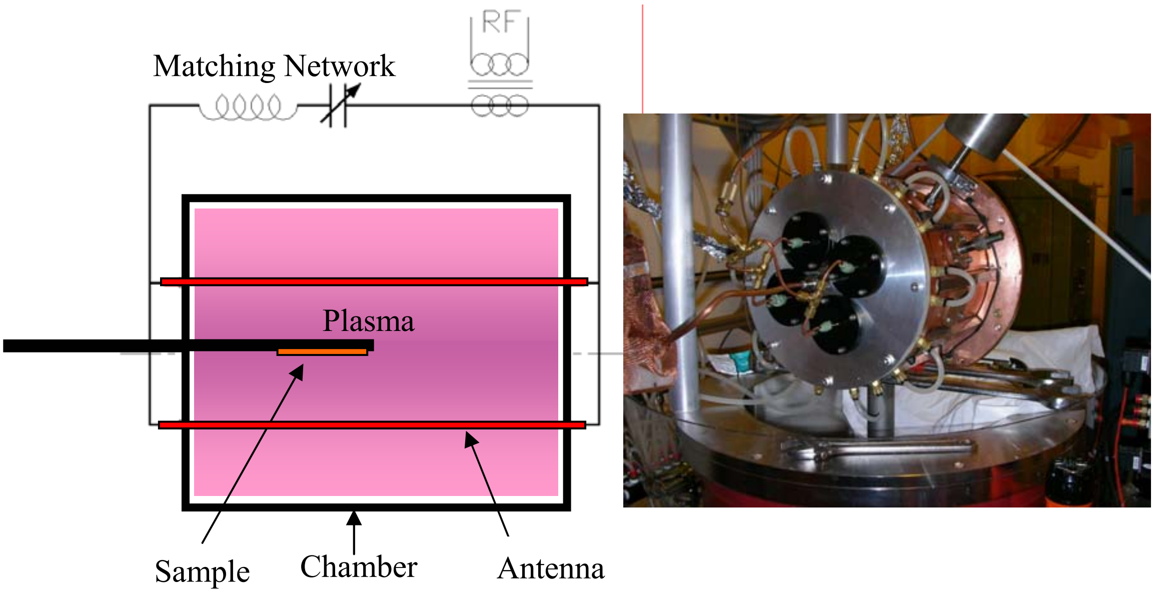

Figure 5.2: Schematic diagram of the later design of the sputter system (left); and a photograph of the system (right).

5.1.2 Current Measurement

Since the source is generating both argon and metal ions, to measure the ion current of each species, a mass separator is needed. An E x B filter was designed for ion selection. As shown in the schematic figure 5.3 (a), the extracted ion beam containing multiple ion species goes through an E x B field, different ion species are deflected into different direction due to the magnetic force.

$$\mathbf{r_L} = \frac{\mathbf{mv}}{\mathbf{qB}} = \frac{1}{\mathbf{B}}\sqrt{\frac{\mathbf{2mV}}{\mathbf{q}}} \propto \sqrt{\mathbf{m}}, \sqrt{\mathbf{V}} \qquad 5\text{-}2$$

As shown in equation 5-2, where r_L is the gyro radius of an ion in the magnetic field, m is the mass, q is the charge, B is the strength of the magnetic field, and V is the acceleration voltage. For singly ionized ions with the same acceleration voltage V, the lighter ions will have a smaller gyro radius, which means they will be deflected more in the B field.

A pair of parallel electrodes is installed to form an electric field in the perpendicular direction to the beam initial direction and the B field. The electrodes are biased at a same voltage (V_b) but with opposite polarities, an electrostatic force on the ions is formed in the opposite direction of the magnetic force. By increasing the biasing voltage, the electrostatic force cancels the magnetic force and ions are gradually bending back towards the beam exit slit. When the biasing voltage reaches the point where the electrostatic force equals to the magnetic force for a certain ion species, the corresponding ion can go straight trough the E x B field and pass the slot opening at the other side of the E x B filter and detected by a signal detector. The voltage V_b can be calculated using equation 5-3, where E is the strength of the electric field, d is the distance between the parallel electrodes.

$$E = \frac{2 \cdot V_b}{d} = B \cdot v = B \cdot \sqrt{\frac{2 \cdot q \cdot V}{m}} \qquad 5\text{-}3$$

As can tell from the equation, heavier ions are always detected at lower biasing voltage. The photograph of the E x B device is shown in figure 5.3 (b). It consists of a beam collimator in the front, the parallel plates and the permanent magnets, a slot aperture and a piece of graphite at the end. The beam collimator has a diameter of 100 μm, and is 3 mm away from the beam extraction electrode. It blocks away the beams with big angles and only a beam with very small half angle can go through and enter the E x B field thus enhancing the detection resolution. The ions with different masses are bended off and only the unbended beam will then pass through the slot aperture, and detected by the graphite signal detector.

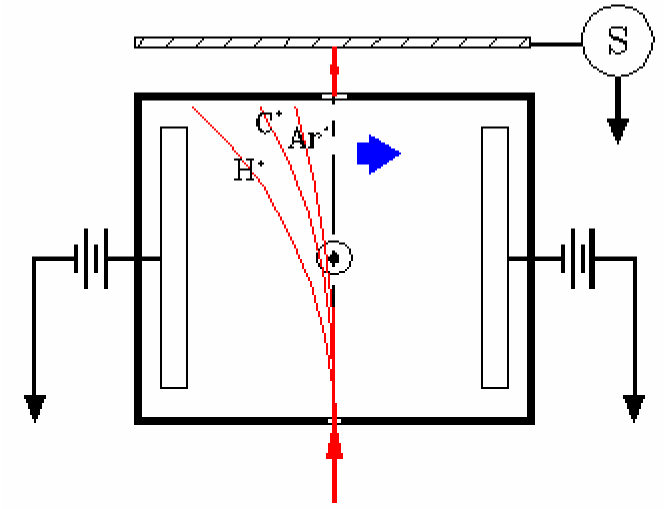

Figure 5.3 (a): Schematic of the E x B ion mass separator.

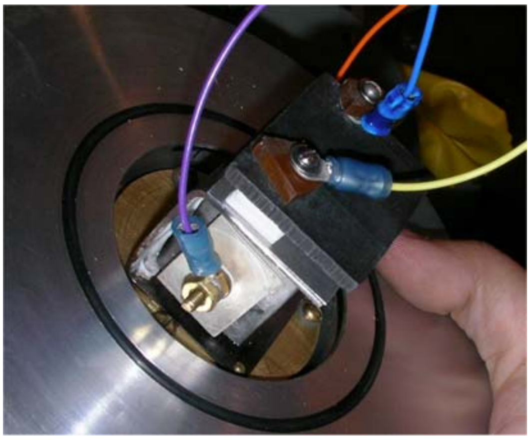

Figure 5.3 (b): Photograph of the E x B device assembled on the system.

The magnetic field is 400 Gauss in the center which is generated by a pair of permanent magnets, and the electric field is formed by a pair of parallel plates which are connected to two sets of high voltage DC power supplies at same voltage but with opposite polarities. The voltage is increased from 0 to ± 1.5 kV and the current signal is measured on a graphite detector.

As shown in figure 5.3(a), heavier ion will be detected at lower voltage. Due to the limitation of the small size of the E x B field and the B field strength, the device does not give a good resolution. Since most metal ions are heavier than argon ion, the metal ion signal appear at lower voltage than argon, this device with a small dimension design can not separate Ar^+ and heavier metal ions very well. However, a much bigger device size and stronger magnetic field will improve the detection resolution. For ions with lower mass, current can be measured. In one of the measurement, the antenna is covered with graphite; the source is running at an RF power of 400W and extraction voltage of 2.5 kV. Carbon ions are generated, the measured current is 15 nA on a 100 μm diameter area. The calculated current density at the target is then $0.2 mA/cm^2$. The current density can be further improved by increasing the RF power, extraction voltage or by reducing the beam spot size.

To conduct the measurement more precisely, a computation was performed by Hannes Vainionpaa to simulate the beam transportation in the E x B field. Due to the size limitation of the field, the magnetic field and the electric field are not uniformly distributed inside the device. As a result, the ion trajectory is not like the ideal case as shown in figure 5.3a. Some sample simulation results are shown in figure 5.4. In this calculation, five ion species are traveling though the E x B field. The five ion species are H^+, D^+, T^+, Ar^+ and Cu^+. Figure 5.4(a), (b), (c) shows how H^+, D^+, T^+ passes through the exiting slit of the device respectively.

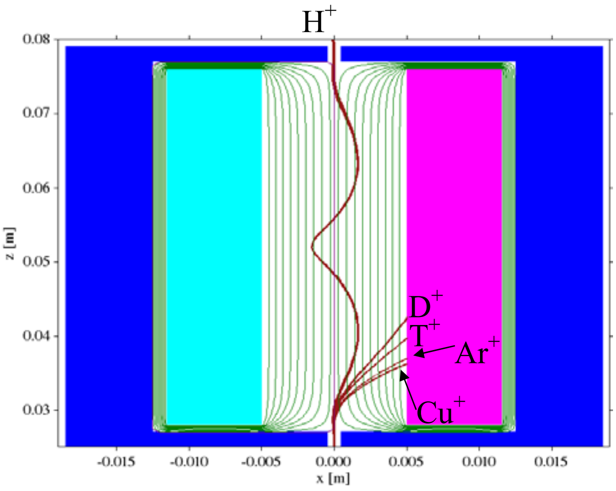

(a)

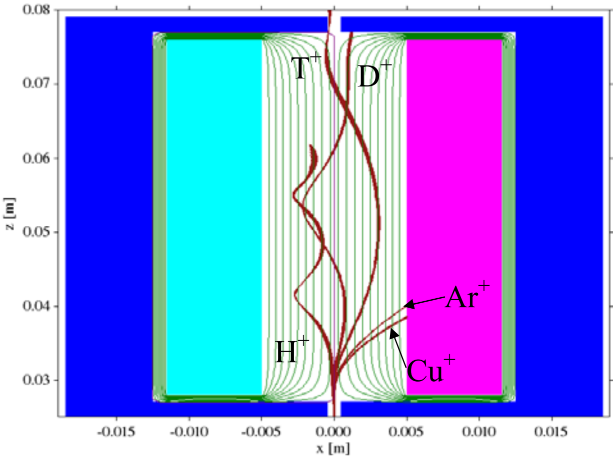

(b)

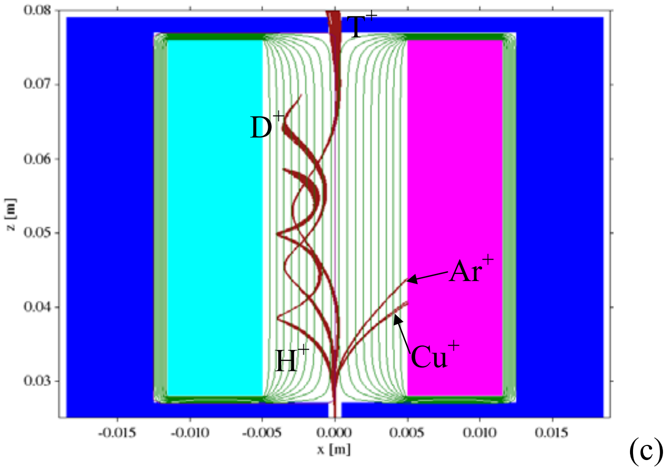

Figure 5.4: Computation results of the ion trajectories in the E x B field. The initial energy of the ions are 2.5keV and the bias voltage on the parallel plates is scanned from 0 to ± 1.5 kV.

5.2 Thin film deposition and applications

5.2.1 Thin film applications

Besides generating metallic ion beam, one of the most important applications for this source is sputtering deposition of metal thin film and some insulating material as well. Thin film deposition technology has been playing very important role in the industry and research area for decades such like:

Sputtering deposition method has been applied to many fields such as electronic components, electronic displays, optical coatings, optical data storage devices, antistatic coatings, and hard surface coatings etc. In addition, high rate sputtering methods for ferromagnetic materials, such as Fe and Ni, have been developed expending further the fields of sputtering application.[4-5]

Some prior research has also shown that if the sputtered atoms are highly ionized, it will be very useful to control the film properties with the aid of the ionic charge and/or the kinetic energy of the ionized sputtered atoms[6-8]. Energetic bombardment of background gas ions or ions of the depositing species can increase the mobility of deposited adatoms, which reduces the internal voids and defects and leads to a much denser film structure. For the ionized metal species, if the acceleration potential for the ions is significantly greater than their thermal energy, the ions will arrive at the wafer surface at almost exactly 90° with a controllable energy. If the percentage of the metal flux that is ionized is made high, it will help to fill the bottom part of the trench which has a high aspect ratio to achieve the conformal coating[9]. Being able to generate high density argon plasma, our sputter source thus can perform highly-ionized deposition in an efficient way.

5.2.2 Different coating mode

Metallic species of Cu, Fe, Ni, Mn and Pd have been tested. Thin films of different metal species were deposited on substrates of silicon and glass. Sturdy and uniform thin films have been achieved. A layer of copper thin film formed with high uniformity is shown in figure 5.5. The left part of the substrate was covered by a small copper block, and the curved surface on the left side of the thin film shows how the film grows at the edge. The profile was measured by a laser interference microscope and the average deposition rate is about 450nm/min with a cw RF power of 500W. The deposition rate varies for different metal materials due to different sputtering yields. The deposition is controlled mainly by the RF power, gas pressure, and duty factor (in pulse mode).

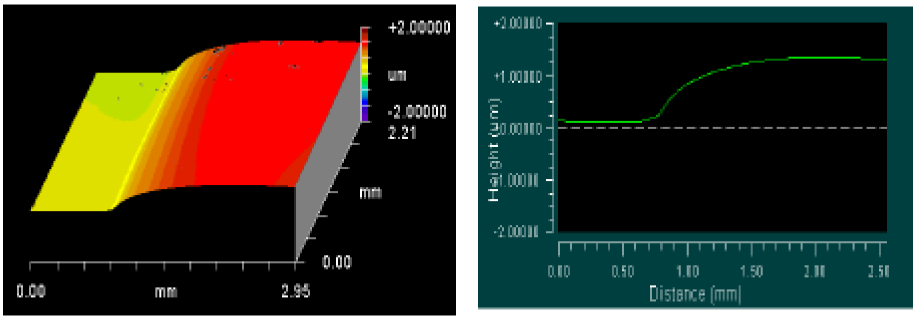

Figure 5.5: Image of copper thin film deposited on silicon substrate taken by laser interference microscope (left) and profile (right).

The microstructures of the thin film depend on the deposition parameters and local topography. An experimental study has been carried out to investigate the effect of the coating parameters on the film microstructure and profile. As illustrated in figure 5.6 a, at relatively low RF power and low gas pressure (coating condition 1), the metal ions approach the sidewalls at high oblique angles. Due to shadowing effects, film on the sidewalls is in the form of columnar, porous structures. In addition, due to atomic-attraction forces, the incident atoms are preferentially deposited on the top corners of the hole. This again gives rise to overhangs at the top corners.

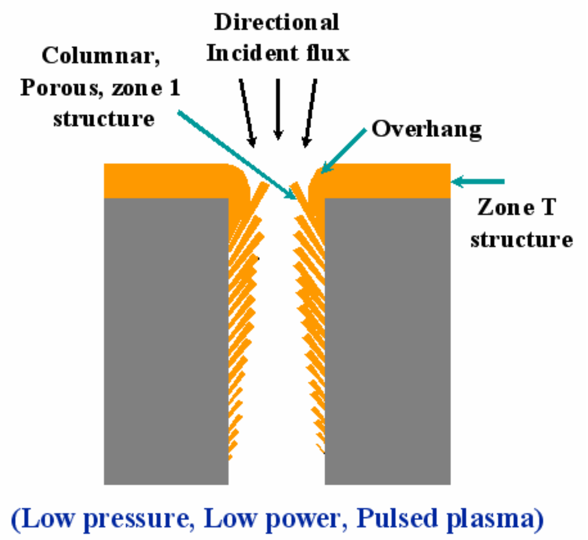

Figure 5.6a: Schematic diagram of the film microstructure under coating condition 1 : low pressure and low RF power.

Experiment is performed at 500W RF power and 100 mTorr gas pressure. The substrate is a 3μm thin film patterned with 3 x 3 arrays of 1.2 μm diameter hole. The result is shown in figure 5.6b. The SEM image shows that with the coating condition 1 discussed above, the film formed near the top corner of the hole has a porous and columnar microstructure.

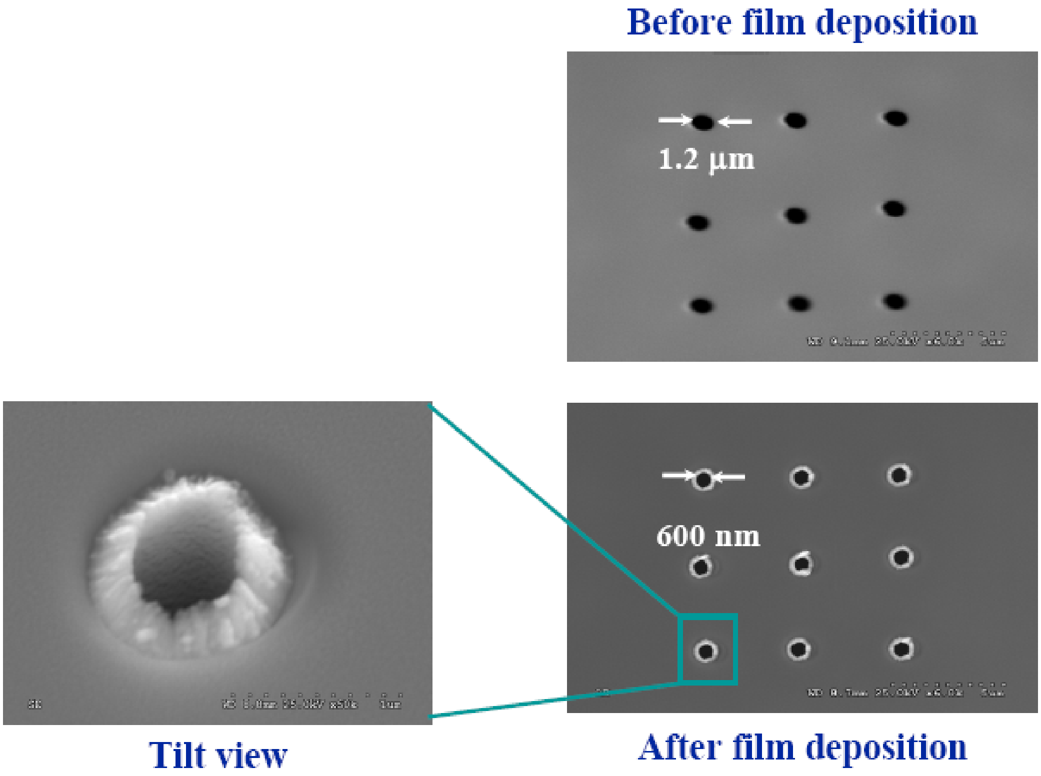

Figure 5.6b: SEM images of the copper thin film grown under coating condition 1 (low gas pressure:100 mTorr and low RF power:500W)

At higher pressure and lower RF power (coating condition 2), the metal neutrals and ions undergo a lot more scattering before reaching the substrate, which greatly enlarges the angular distribution of the flux. As a result, the chance for porous-like film to grow is reduced and the film becomes much denser but the flux directionality is sacrificed. The schematic diagram of such a concept is shown in figure 5.7. Under this coating condition, the top surface of the vias and trenches can be shrunk and closed up very quickly, however, leaving the bottom unfilled. This coating condition can be useful for forming nano-pores.

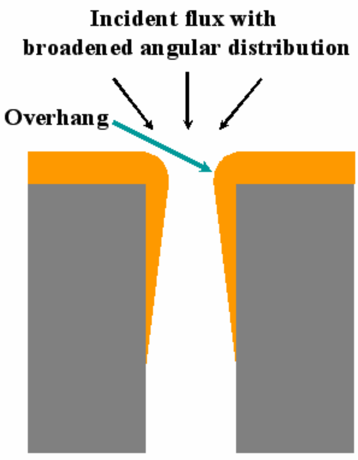

(High pressure, Low power, Pulsed plasma)

Figure 5.7: Schematic diagram of the film microstructure under coating condition 2: high pressure and low RF power.

Another coating scenario appears at high RF power and low gas pressure (coating condition 3). As illustrated in figure 5.8, at low gas pressure, the scattering of the Cu ions and neutrals is highly reduced; this helps to form a highly directional flux, which is very important for coating of trenches with high aspect ratio. In addition the Cu ions and neutrals can maintain relatively high kinetic energy because they undergo less scattering that would slow them down. The plasma density is higher at high RF power, which results in a bigger voltage across the plasma sheath both around the sputtering target and the coating sample. As a result, the energy of the metal ions and the neutrals is higher. When coating narrow trenches or vias with high aspect ratios, they can re-sputter the deposited film on the deposited film on the sidewall while traveling through the trench/via, improving the uniformity and conformality of the film. All these characteristics make this coating mode the most ideal for high aspect ratio conformal coatings.

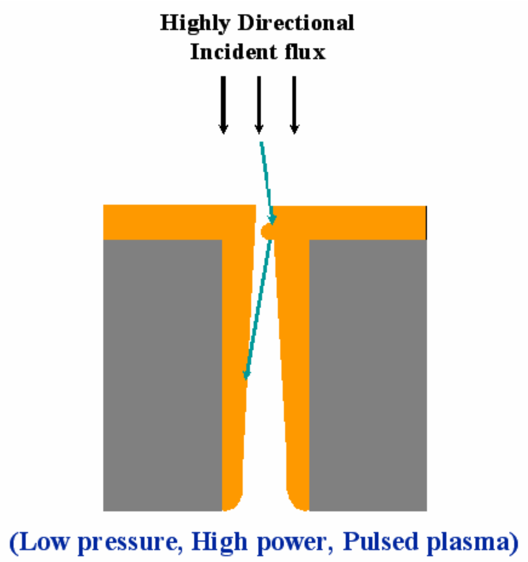

Figure 5.8: Schematic diagram of the film microstructure under coating condition 3: (low pressure and high RF power).

5.2.3 Application of thin film deposition I: Formation of nanopore and nanoslit

From the previous discuss, a conclusion can be drawn that by means of thin film deposition method, some patterns with nanoscale feature size can be fabricated, which usually is very hard to do using conventional fabrication process.

Recently there is a lot of demand arising in a wide range of research fields for nanofabrication on a variety of material with different geometries. Focus ion beam milling using conventional gallium ion beam generated by liquid metal ion sources is facing the great difficulty in improving the throughput. One way to overcome this is to employ the ion beam imprinting system to form multiple shaped ion beams simultaneously, which eliminates beam switching and scanning. In order to push ion beam imprinting technology to nanometer regime, masks with arrays of apertures or slits at nanometer scale are inevitable. The ability to fabricate membranes with arrays of apertures only a few nanometers in diameter is important to many fields of research, including ion beam lithography[10,11], DNA sequencing[12], single ion implantations[13], and single molecule studies. Currently, the methods of producing nanoscale pores in membranes have important limitations. One method of fabricating holes with dimension of tens of nanometers is to use electron beam lithography, followed by reactive ion etching. But achieving smaller feature sizes is difficult, and because the process includes resist exposure and etching, it is slow. Holes directly milled by focused ion beam (FIB) are limited in dimension to the beam diameter, which is about 10nm, and arrays of apertures must be drilled one at a time. Molecular-scale nanopores in silicon nitride films have been reported using the technique of ion-beam sculpting[12]: apertures with an initial diameter of 100nm were fabricated in a free-standing Si_3N_4 membrane supported on a silicon frame. Irradiating the holes with a 3 keV argon ion (Ar^+) beam caused them to close rather than open up, resulting in nanopores 2-3 nm in diameter, as controlled by a feedback monitoring circuit. However, this technique can only be applied to insulating membrane, such as Si_3N_4 and silicon dioxide (SiO_2), and multiple simultaneous nanopores have not been reported using ion-beam sculpting. Another method of fabricating nanopores is to use a dual beam system employing an FIB and a SEM[14]. Apertures ranging from 50 nm to 600 nm in diameter are pre-machined using an FIB, followed by gas-assisted deposition using an FIB/SEM dual beam. Depositing a film of metal like platinum around the edges of the aperture makes them smaller and smaller. Like the ion-beam sculpting technique, forming multiple nanopore arrays with FIB/SEM is very slow. The sputter source and the coating conditions discussed above provide a means of forming arrays of nanopores simultaneously on a thin, solid-state membrane using plasma-assisted thin film deposition. By depositing layers of metallic thin films, the aperture sizes of pores in a pre-fabricated membrane can be reduced from a couple of micrometers down to tens of nanometers and even smaller. The plasma-assisted thin-film deposition technique has two significant advantages. First, there is no restriction on the material that can be used for membranes. The presence of a plasma eliminates any charging problem, allowing uniform thin-film coating on either conducting or insulating samples. In the experiment, a membrane was prepared as a pattern generator for an ion-projection lithography system.[15] As shown in figure 5.9, starting with a bare 4” silicon wafer, low stress silicon nitride (LSN) films are deposited on both sides of the wafer. Then, 1mm^2 windows were patterned on the backside of the wafer using photolithography, and later silicon is etched away by potassium hydroxide (KOH) wet etch step, during which LSN was used as a mask. After the KOH etch, a silicon nitride membrane approximately 3μm thick remained. A focused gallium ion beam was then used to drill apertures of different dimensions in the membrane.

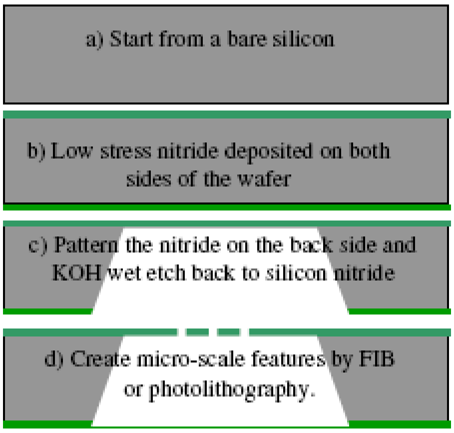

Figure 5.9: Process flow of fabricating a thin membrane.

A second advantage of this technique is that there is no restriction on the initial dimension of the pre-machined apertures. Starting with an aperture of a diameter of 650 nm, as shown in figure 5.10, the aperture becomes smaller after copper depositing on the substrate surface and sidewalls. The SEM micrographs in figure 5.10 show that the diameter of the hole was reduced to approximately 200 nm after 3 hour of deposition. There is no limit to how small the aperture will shrink before it is fully closed up. By depositing layer after layer of copper film the size of the aperture continues to shrink. Finally after another 1.5 hours deposition, the size of the aperture was reduced to approximately 13 nm. Presently the dimension of nanopore is gauged only by the deposition time. Accurate control of the final aperture size can be achieved by monitoring the ion current that passes through the aperture.

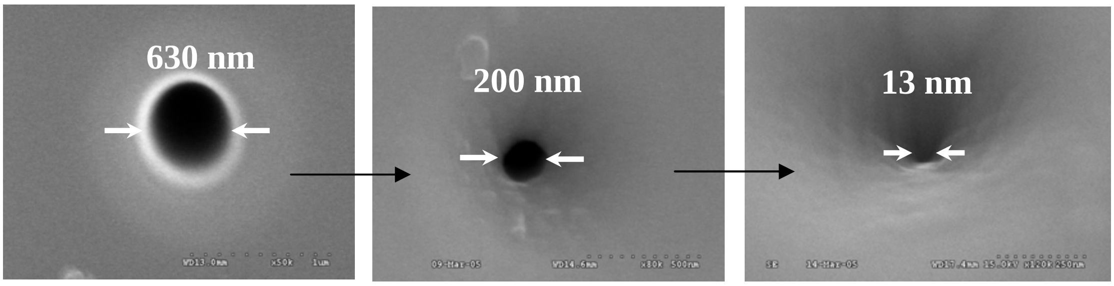

Figure 5.10: An aperture after copper deposition. Its size is reduced from 630 nm to 200nm after deposition for 2.5 hours, and 13nm after deposition for another 1.5 hours.

This method is useful for fabricating a variety of nano-structures. Similar shrinkage was observed for several different geometries besides round holes, including rectangular slits. The rectangular-shaped feature shown in figure 5.11 maintained the same shape after the shrinkage. After subsequent copper depositions, the width of a nanoscale slit was reduced from 830 nm to approximately 20 nm.[16]

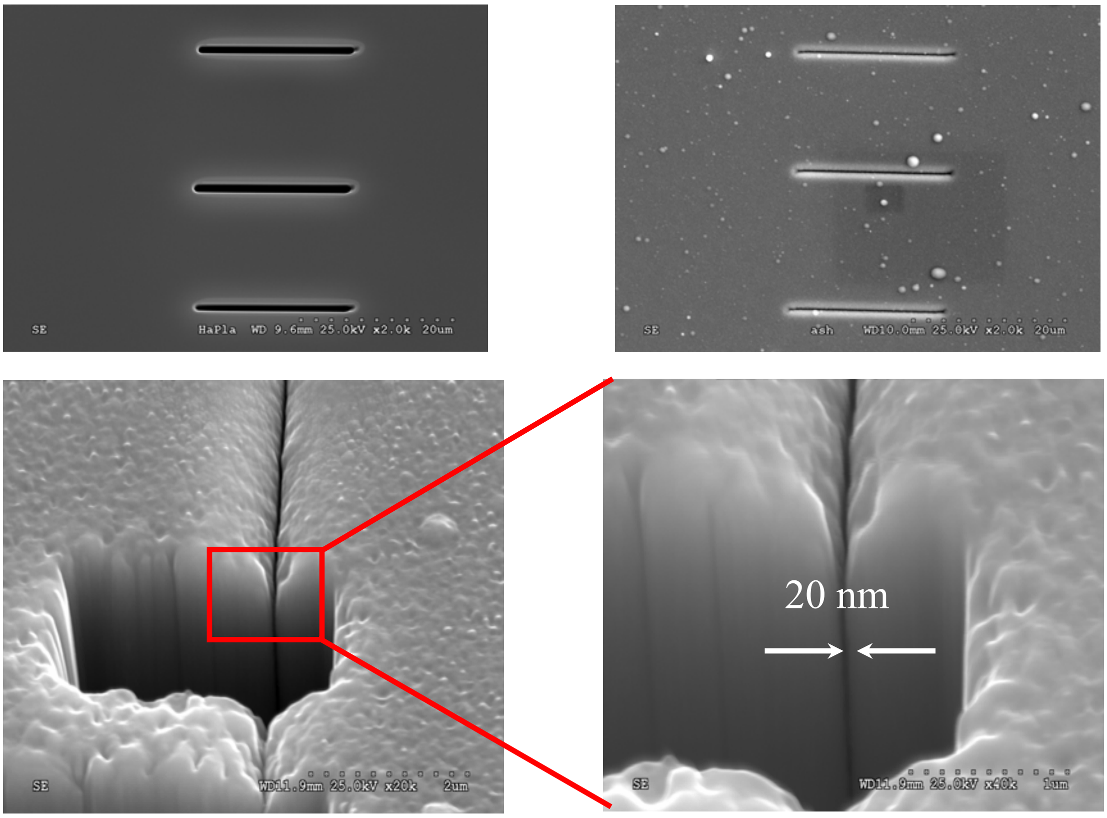

Figure 5.11: SEM micrographs of nano-slit arrays after subsequent copper depositions. The size of the slit continues to reduce from 830 nm before deposition, to 20 nm after deposition (top). And cross- section view of the slit (bottom).

This technique is very useful in bionanotechnology (e.g. nano-fluidic system fabrication). In the field of bionanotechnology, nanochannels are essential components in nano-fluidic system[17]. This coating technique thus implies a very efficient way for nanochannel fabrication especially for multi-nanochannel fabrication[16].

5.2.4 Application of thin film deposition II: Conformal trench coating

Conformal trench coating technique is of great interest in research area of microelectronics. In the area of microelectronics, a search is underway to find a reliable technique for filling trenches and vias using copper metallization technology.

Due to the need for further decrease of the line width and the via area in ULSI application, vias with aspect ratios of approximately four to one have to be filled completely[18]. Therefore, conformal coating continues to be a growing need in the microelectronics industry.

Physical vapor deposition (PVD) techniques, especially magnetron sputtering, have been widely used for thin-film deposition in microelectronics. However, the conformality of films from the conventional magnetron sputtering deposition process is poor due to a great deal of self-shadowing. Shadowing effects can cause, for example, poor step coverage on sidewalls and bottoms of trenches and vias, and can form overhanging structures on the top corners of the trenches and vias. These effects can lead to void formation when attempting to fill a surface feature[19]. Thus CVD-based techniques, which are able to fill trenches and vias with a high aspect ratio[20], are preferred. However void creation can still be observed, due to non-uniform layer growth. In addition, the deposition technique and the chemistry make their application much more difficult.

As mentioned before, conformal coating of trenches with high aspect ratios can be achieved using the coating condition 3 described above. In the experiment, a (1 0 0) oriented p-type Si wafer is used as the substrate. Two sets of patterns are prepared on the substrate. One set is patterned with high aspect ratio trenches using the Surface Technology Systems (STS) Advanced Silicon Etch (ASE) system. The widths of the trenches range from 1 μm to 4 μm, and the aspect ratios range from 20:1 to around 6:1. The other set of patterns are fabricated using the FIB system. The patterns have much smaller sizes, which range from 80 nm to 150 nm. The aspect ratio is about 18. SEM pictures of conformal coating patterns are shown in figure 5.12. A layer of copper film with a thickness of 600 nm is coated around a 4-µm-wide silicon trench, the aspect ratio of which is 6:1. The coating was highly conformal. The coated film follows the topology of the trench fairly well and exhibits a high degree of uniformity. This coating condition also works very well at a much smaller scale of trench size. Figure 5.13 shows the SEM images of the cross-section of a 110 nm-wide trench before and after copper film coating. The aspect ratio is as high as 18:1. After the deposition, the trench width is reduced to 60 nm with a 25 nm-thick copper film coated on each side.

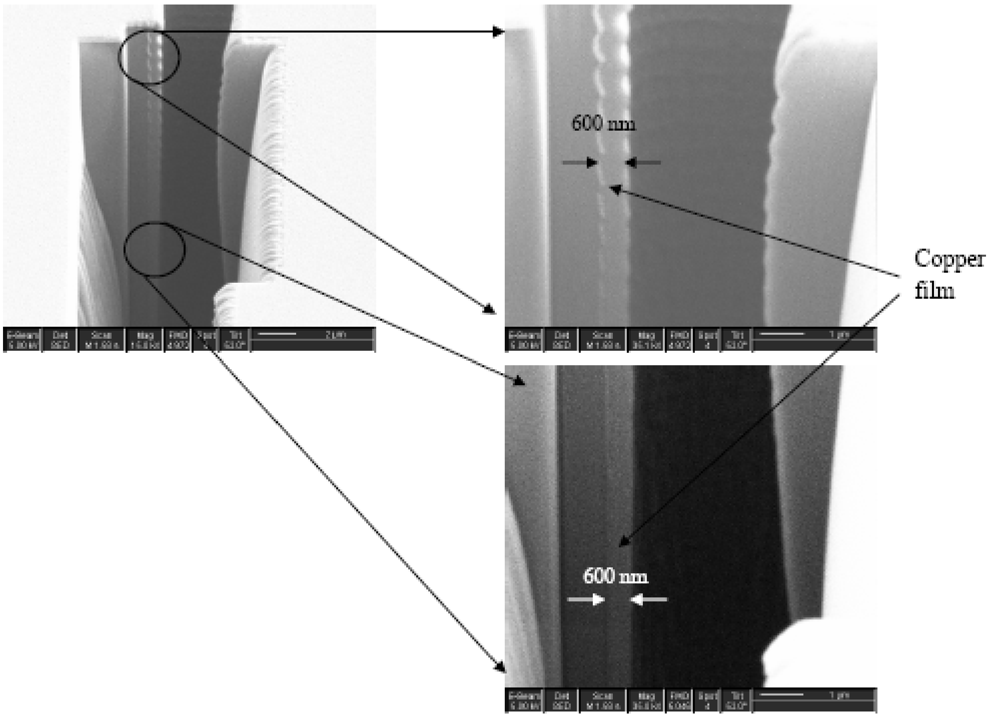

Figure 5.12: SEM pictures of the cross-section of a conformal coating on a 4 µm wide trench; the aspect ratio of the trench is around 6:1 (left). And zoom in of the cross-section. (right) The

wiggles on the sidewall of the trench are coming from the etch process, not related to the copper deposition process.

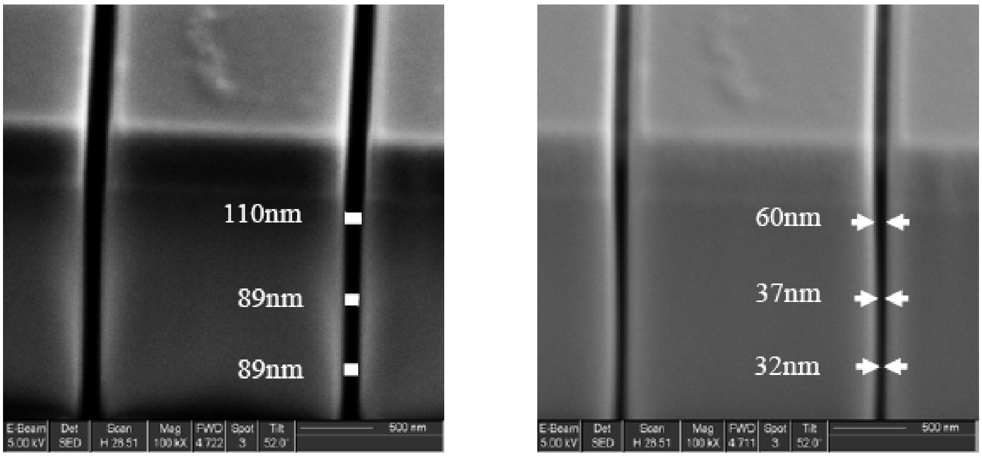

Figure 5.13: SEM pictures of the cross-section of a conformal coating on a 110 nm wide trench; the aspect ratio of the trench is 18:1. (left) cross-section of the trench without copper film coating; (right) cross-section of the trench with copper film coating.

5.2.5 Coating with insulating material

By changing the antenna covering material from copper to graphite and, at the same time, introducing both CH_4 and argon mixed gas to generate plasma, DLC thin film can be formed on the substrate. With 400 W of CW RF power, a 200 nm-thick DLC film is formed after a 30 min coating time.

Diamond-like carbon (DLC) films are of considerable research interest because of their widespread applications as protective coatings in areas such as optical windows, magnetic storage disks, automobile parts, biomedical coatings and MEMS devices.

5.3 Mixture deposition and direct patterning

5.3.1 Mixture deposition

Besides forming thin films of single metallic specie, mixture deposition of multiple metal species has found more and more important applications especially in the field of magnetic storage media formation. By allocating the depositing materials in a proper way the sputtering system can accomplish this task very well. Some preliminary experiments have been performed for mixture deposition of Ni and Fe alloy.

Mixture deposition of different metal species is accomplished by arranging the antenna alternately with small pieces of different metal materials as shown on figure 5.14. When each piece of material is small enough and arranged uniformly on the antenna, the deposited mixture is also fairly uniform. Mixture deposition of Ni and Fe patterned film is carried out, and the TOF-secondary ion mass spectrum (SIMS) analysis results are shown in figure 5.15. The distribution of both Fe and Ni are uniform, and the ratio of the two species in the alloy thin film is about 33.7: 66.3. Almost no argon is detected in the coated layer. By changing the proportion of exposure area of the metal species on the antenna and taking into account the difference of sputtering yields, the ratio of each deposition composition is adjustable. NiFe films are very important soft magnetic materials due to the high magnetic moment and low magnetostriction. The capability of depositing NiFe alloys with adjustable compositions will allow a large number of parameters available for material characteristic modification such as dielectric constant and magnetic coercivity of the nanoscale islands, which makes the technique very useful in magnetic recording media fabrication[21].

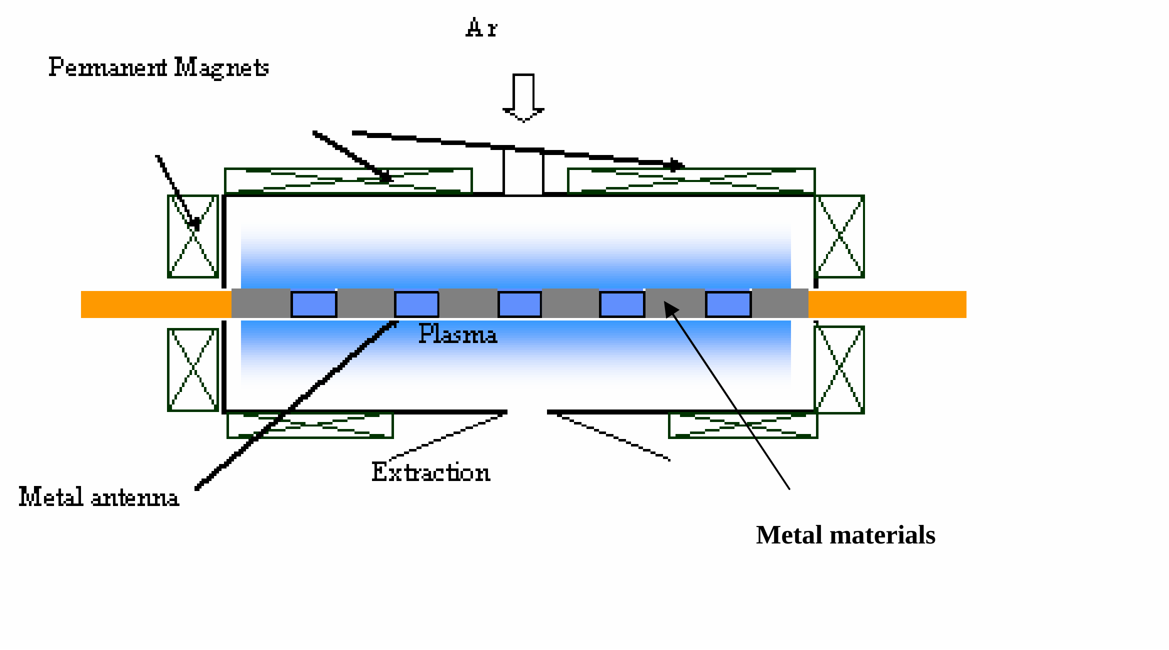

Figure 5.14: Schematic of the target materials arrangement on the antenna.

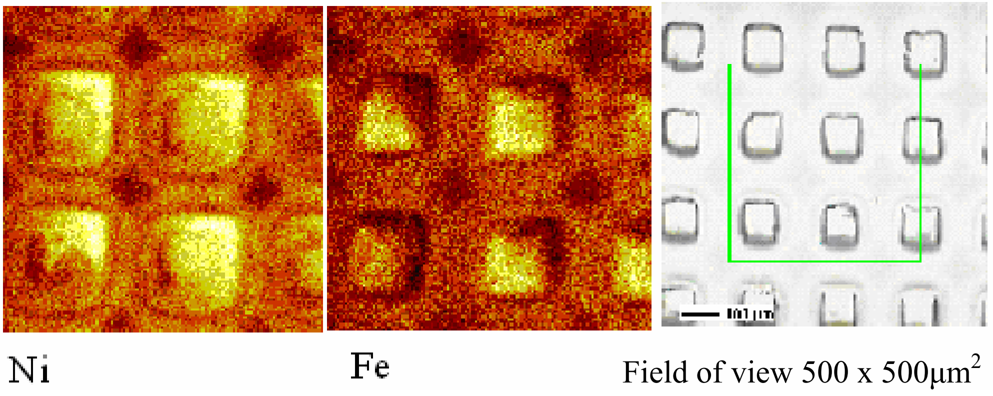
Ni Fe Field of view 500 x 500µm^2

Figure 5.15: TOF-SIMS analysis result of the patterned NiFe alloy thin film: Ni in the thin film (left), Fe in the thin film (middle), square shaped thin film patterns on silicon substrate (right).

5.3.2 Direct patterning

Conventionally a patterned thin film is fabricated after going through a series of processes: thin film deposition, photolithography patterning, and etching. The focused ion beam technology makes it possible to direct pattern the metal thin film.

Two kinds of patterning scheme are developed. Some preliminary results using these methods have been achieved. The experiment will be explained in details in the following discussions.

In semiconductor industry, metallic thin film is patterned using a light-sensitive photoresist and etched using reactive ion etching (RIE) to form circuit elements. The pattern generation process is usually an extremely slow process and the cost is high. Taking advantages of focused ion beam technology and combining with an ion beam imprinting scheme[22], two different metal thin film patterning schemes are developed. One is called directly depositing patterned metallic thin film and the other one is resistless ion beam sputtering. In the first scheme as shown in figure 5.16, a stencil mask containing apertures with different shapes like lines, squares or round holes is used as the plasma electrode. The metal ion beam comes out through the mask, reaching the substrate in similar shapes. By controlling the distance of the gap and the electric field between the mask and the substrate, the demagnifications of patterns can be adjusted. In this way, some special patterns can be formed at one exposure. It eliminates beam scanning and switching, and the patterning process thus can be simplified a lot.

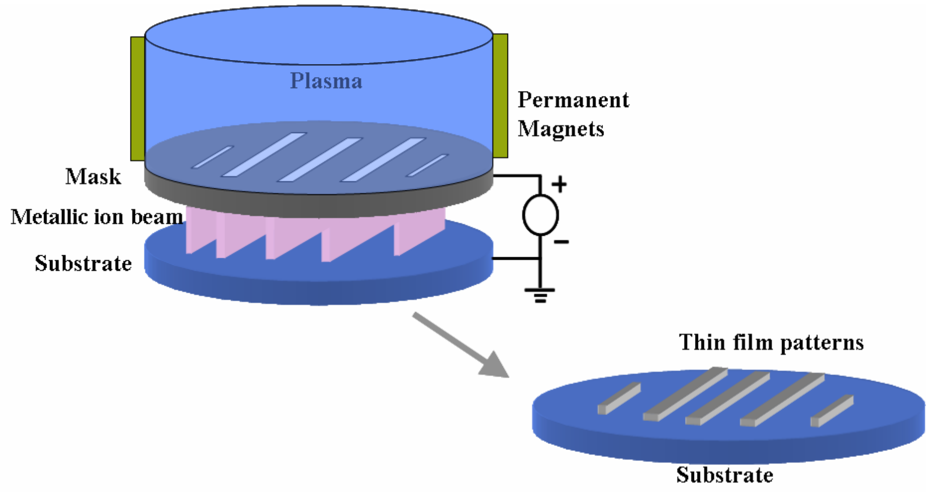

Figure 5.16: Ion beam direct patterning scheme-1: directly deposit patterned metallic thin film.

Contact deposition is tested first. In this case, the mask and the substrate surface contact firmly. Both the source body and the substrate are well grounded. Metallic ions reach the surface of the substrate with the energy equal to the plasma potential. 1:1 pattern transfer is achieved under this condition and some deposited patterns are shown in figure 5.17 and the step height analysis results by KLA-TENCOR ALPHA ASIQ profiler are shown on the right. At micro scale, contact pattern transfer can work reasonably well. However, it still has a strict requirement on a firm contact between the mask and the sample surface and also on the flatness of the mask. Moreover, it can only conduct 1:1 pattern transfer and cannot produce any reduction.

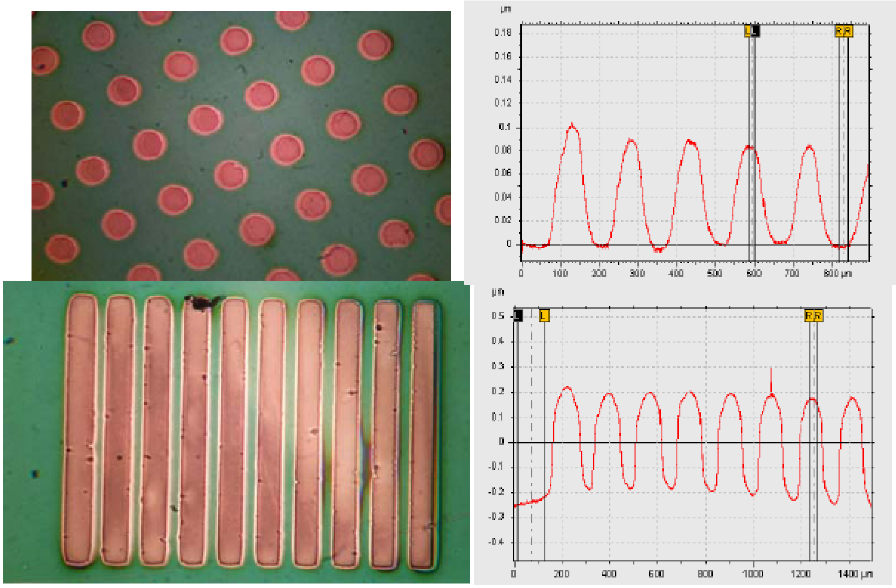

Figure 5.17: Directly patterned copper deposition: pictures taken under optical microscope (left), step height analysis results by KLA-TENCOR ALPHA ASIQ profiler (right).

Focused ion beam technology can help to overcome this difficulty. In a proof-of-principle experiment (shown in figure 5.18), the substrate is biased at a negative potential relative to the ground; an electric field is generated between the plasma electrode (the mask) and the substrate. The voltage applied is 100-200 eV to ensure deposition effect dominates instead of sputtering or doping. Metal ions are extracted and reach the substrate with a demagnification factor of about 1.7.

Copper particles depositing on the edge of the mask was found to be an issue. As shown in figure 5.18, the deposition on the mask magnified the roughness (which is initially induced by the mechanical drilling) around the mask edge. One way to overcome this issue is to bias the mask at a relatively negative voltage respect to the source body. In this way, the Ar^+ and Cu^+ can have a higher kinetic energy when they reach the extraction mask, where deposition and sputtering rate cancel each other.

After the beam extraction, the Cu^+ can be separated from the Ar^+ and further focus down using electro-static lens.

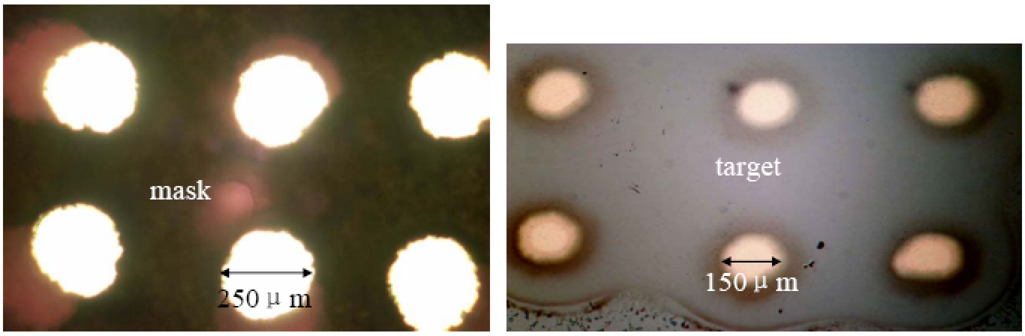

Figure 5.18: Copper patterns directly formed by extracted copper ion beam. The mask is shown on the left. Some demagnification can be achieved by using extracted ion beam.

In the second scheme of resistless ion beam sputtering shown in figure 5.19, a layer of thin film is deposited first, and then different shapes of features are formed by a shaped Ar^+ beam with certain energy and beam spot size. With a beam focusing electrostatic lens, the ion beam can be focused to hundreds or tens nanometer scale, which will make this direct pattern technique useful in the application of photomask fabrication and repair. Some preliminary experiments have been performed. In the experiment, a single-gap extraction configuration is employed. The argon beam extracting from 250 μm diameter holes which is focused by the electric field between the mask and the substrate, is used to sputter a Ni thin film coated on a piece of silicon wafer. As shown in figure 5.20, a circular area with a diameter of 20 μm on the thin film is totally sputtered off which indicates that a demagnification factor of 12 is achieved. The measured profile is shown on the right.

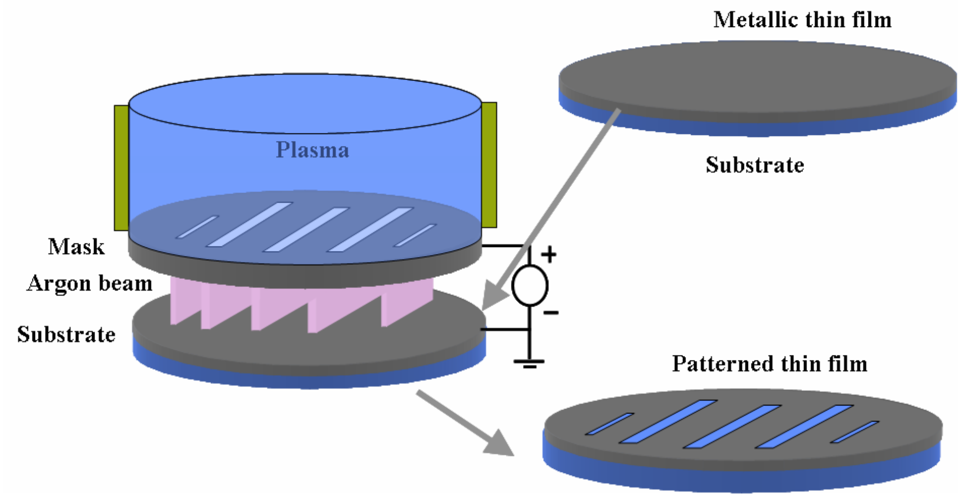

Figure 5.19: Ion beam direct patterning scheme-2: resistless ion beam sputtering.

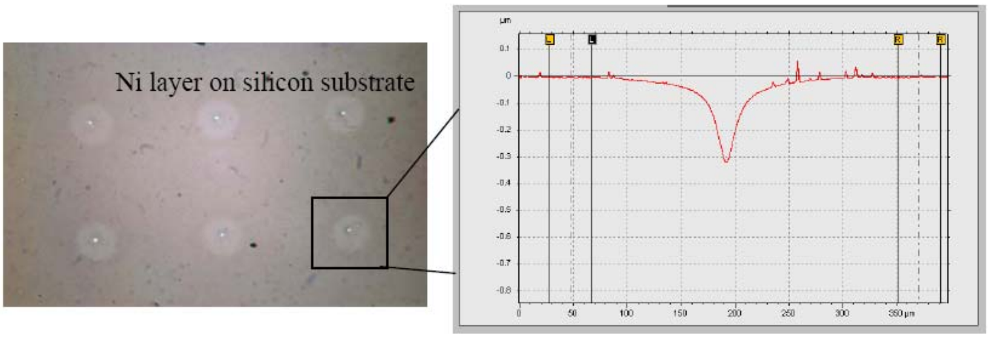

Figure 5.20: Resistless argon beam sputtering Ni from silicon substrate: pictures taken under optical microscope (left), step height analysis results by KLA-TENCOR ALPHA ASIQ profiler (right).

5.4 Summary and discussion

The RF-driven plasma source for metallic ion beam generation and sputter deposition of metal thin films has been presented in this chapter. Experiment has demonstrated various metallic ions generation and three different thin film coating conditions. Some applications have been discussed.

To measure the metallic ion current, an E x B ion mass separator has been fabricated. But the first device is made small to fit in the compact system; the dimension limits the separation resolution. So it is not able to measure the metal ion current precisely. A better design of the ion mass separator is needed to form a high purity metallic ion beam.

The source has been shown to have a high ionization ratio on sputtered metallic atoms theoretically and through the visual observations. But the ionization ratio needs to be measured quantitively as an important experimental support for the high ionization ratio argument.

Reference:

[1] Q. Ji, T. –J. King, K.-N. Leung, S. B. Wilde, *Rev. Sci. Instru.*, Vol 73, 822 (2002).

[2] H. Yamashita, M. Harada, J. Misaka, M. Takeuchi, Y. Ichihashi, F. Goto, M. Ishida, T. Sasaki and M. Anpo, *J. Synchrotron Rad, Vol 8*, 569 (2001).

[3] www.farfield-scientific.com/bio_pro.asp

[4] M. Yamashita, *J. Vac. Sci. Technol.* A 7, 151 (1989).

[5] S. Kadokura, T. Tomie, and M. Naoe, *IEEE Trans. Magn*. 17,3175 (1981).

[6] K F Chiu, Z H Barber and R E Somekh *Thin Solid Films* 343 – 344, 39–42, (1999).

[7] K F Chiu and Z H Barber Thin Solid Films 358, 264-269 (2000).

[8] K F Chiu, M G Blamire and Z H Barber *J. Vac. Sci. Technol.* A 17, 2891-2895 (1999).

[9] www.research.ibm.com/journal/rd/431/rossnagel.html

[10] X. Jiang, Q. Ji, L. Ji, A. Chang, K.-N. Leung, *J. Vac. Sci. Technol.* B21, 2724–2727 (2003).

[11] Q. Ji, L. Ji, Y. Chen, K.-N. Leung, *Appl. Phys. Lett.* 85, 4618–4620 (2004).

[12] J. Li, D. Stein, C. McMullan, D. Branton, M.J. Aziz, J.A. Golovchenko,*Nature* 412, 166–169 (2001).

[13] T. Schenkel, A. Persaud, S.J. Park, J. Meijer, J.R. Kinglsey, J.W. McDonald, J.P. Holder, J. Bokor, D.H. Schneider, *J. Vac. Sci. Technol.* B20, 2816–2823 (2002).

[14] T. Schenkel, V. Radmilovic, E.A. Stach, S.J. Park, A. Persaud, *J. Vac. Sci. Technol.* B 21, 2720–2723 (2003).

[15] X. Jiang, K.-N. Leung, Abstract Proceedings of the 49th International Conference on Electron, Ion, and Photon beam Technology and Nanofabrication, 311 (2005).

[16] Q. Ji, Y. Chen, LL. Ji, et al, *Microelectronic Engineering* 83 (4-9), (2006)

[17] Lee C, Yang EH, Myung NV, et al, *Nano Letters* 3 (10),1339-1340, (2003)

[18] C. Wenzel, N. Urbansky, W. Klimes, P. Siemroth, T. Schulke, *Microelectronics Engineering*, 33, 31 (1997)

[19] T. Karabacak and T-M. Lu, *J. Appl. Phys. 97*, 124504 (2005)

[20] K. Ueno, K. Ohto and K. Tsunenari, Advanced Metallization jbr ULSI Applications, R. Blumenthal and G. Janssen (MRS, Pittsburgh, PA) 95-101 (1994).

[21] I. Giouroudi, A. Ktena, E. Hristoforou, *J. Optoelectron. Adv. Mater*. 4, 281 (2002).

Chapter 6:

Summary

The work described in this thesis is mainly about developing three ion beam tools with simulation and experimental investigation.

6.1 Experimental work achievements

6.1.1 Development of the mini-rf plasma source and hardware preparation for the FIB/SEM dual beam system

A mini-rf plasma ion source is developed and ion source performance has been studied in detail. The experiment results have demonstrated a high ion current generation with less power consumption. An FEI two-lens electron (2LE) column for SEM imaging, and a five-axis manipulator system developed by Zyvex Corporation have been tested and integrated on a dual-beam chamber. A 35 kV ion beam optical lens has been fabricated and is waiting for final integration. The application for this system is also discussed in that chapter as well.

6.1.2 Development of a double-chamber plasma source and combined-beam study

Chapter 3 is focused on discussion of developing a combined electron and focused ion beam system. The formation of a single beam consisting both positive ions and electrons has been achieved by developing a new double-chamber ion-electron plasma source. Separate control of the ion source chamber and electron source chamber has been achieved. Experiment has been conducted on this double-chamber source with a single gap extraction. The experimental results have demonstrated the electron neutralization effect and electron post-ionization effect induced by the combined beam. Multiple beamlets have also been generated and used for ion milling applications, and the combined-beam has shown higher milling efficiency than a pure ion beam.

6.1.3 Development of a new plasma source for metallic ion beam generation and metal thin film deposition

Chapter 5 mainly discusses about developing a novel plasma source which is used for generating metallic ion beams and also used for physical vapor deposition (PVD) of various metal thin films. The prototype device has shown the capability of generating ions of Cu, Ni, Fe, Pd and depositing thin films of these metallic species. Two schemes for direct patterning of metal thin film have been developed and demonstrated by preliminary results. Three different deposition conditions have been observed, one of which (deposition at low RF power and high gas pressure) has provided a solution for nano-pore fabrication. Conformal deposition of trenches with high aspect ratios has also been achieved by one of the deposition conditions (deposition at high RF power and low gas pressure).

6.2 Simulation work achievements

6.2.1 Simulation design of an ion acceleration column for the dual FIB/SEM system

Simulation work has also been performed in order to design the ion beam accelerator column for the ion beam systems. For the dual FIB/SEM system, simulation is done with a commercial simulation software-Munro simulation code. The first order ion optics properties and aberration information of the ion optical column have been obtained. Beam transportation has been simulated by a 2D ray tracing program. According to the simulation results, sub-micron size ion beam down to 100 nm can be generated on this system.

6.2.2 Simulation for the combined electron and focused ion beam system

In order to simulate electrons and positive ions simultaneously, simulation code-IBSimu code has been developed and is being optimized by Taneli Kalvas. With the help of both Munro simulation and IBSimu simulation, preliminary design of the beam accelerator column for this combined-beam system has been achieved. The transportation of the combined-beam has been calculated and plotted by the IBSimu program. Due to the special configuration of this combined beam, beam deflection and beam pulse generation are also different from conventional ion beam system. These two situations are investigated by IBSimu and XOOPIC simulation as well.

6.3 Suggestions for future work

6.3.1 Dual FIB/SEM system final installation and test

The dual FIB/SEM system is right now in the final stage for installation. After finishing assembling the ion accelerator column, the ion gun will be installed on the dual beam chamber. Beam exposure test will be conducted to test the dual beam system performance at Harvard University. Finally the system will be used for ion beam direct doping or other surface modification applications.

6.3.2 Beam simulation and plasma physics modeling for the combined-beam system

More computational work is required for the combined electron and focused ion beam system. Due to the special configuration of the double-chamber source, a high energy (currently several keV) high current (from hundreds nA to tens μA depending on the application) electron beam will go through the ion source chamber, which will introduce a disturb to the plasma in the ion source chamber and will affect the beam extraction as well. A plasma physics model needs to be developed to analyze the plasma condition in the ion source chamber and around the plasma meniscus area. And more detailed simulation need to be carried out for a more precise beam accelerator column design. So far, the IBSimu code can only calculate the ion and electron trajectory but can not give out the aberration information. Also the simulation at beam extraction is not accurate. The simulation code needs to be further optimized for this simulation.

6.3.3 Experimental investigation of the effects introduced by the combined-beam

Since the combined electron and focused ion beam is a new topic, much more interesting effects and phenomena need to be thoroughly investigated.

As discussed in chapter 3, electron post-ionization effect has been demonstrated experimentally. But several approximations are applied when obtaining the data curves. The trend is real but more precisely designed experiment is needed in order to evaluate the absolute signal. With the current experiment setup and by replacing the secondary ion detector with a negative secondary ion detector, electron post-attachment effect can be investigated. In order to perform this test, a negative secondary ion detector needs to be carefully designed. No electrons should be collected on the detector. Ion current density increasing with the presence of electrons in the combined-beam has been indicated by simulation. This effect is also an important topic that needs to be demonstrated with experimental research. It may provide a promising solution for enhancing signals in nano-SIMS applications.